Thermo-mechanical Stability and Strengthening Mechanisms of Ti/Ni Multilayer Thin Films

Zhou Yang

A dissertation

submitted in partial fulfillment of the

requirements for the degree of

Doctor of Philosophy

University of Washington

2016

Reading Committee:

Junlan Wang, Chair

Jiangyu Li

Ramulu Mamidala

Fumio Ohuchi

Program Authorized to Offer Degree:

Mechanical Engineering

University of Washington

Abstract

Thermo-mechanical Stability and Strengthening Mechanisms of Ti/Ni Multilayer Thin Films

Zhou Yang

Chair of the Supervisory Committee:
Professor Junlan Wang
Mechanical Engineering Department

In this work, systematic studies on mechanical and microstructural properties of Ti/Ni multilayer thin films were carried out to understand the coupled size and thermal effects on strengthening mechanisms of metallic multilayer thin films. The size effect comes from the individual layer thickness and total film thickness, and the thermal effect comes from either post-deposition annealing, in-situ high temperature deposition, or localized surface annealing by pulse-laser irradiation.

For as-deposited metallic multilayer thin films, the deformation behavior was found to follow the traditional trend from dislocation mediated motions with dislocation pile up along interfaces with

layer thickness from microns down to a few tens of nanometers, and single dislocation bowing between interfaces with layer thickness from a few tens of nanometers to a few nanometers, to grain boundary mediated motions with further reduced layer thickness. In addition, strong orientation dependent hardness was observed in as-deposited multilayer thin films. The anisotropic hardness is attributed to dominant deformation mechanism switch from dislocation pile-up against the interfaces to confined layer slip within the layers as the loading direction changes from perpendicular to parallel to the interfaces.

A systematic study on Ti/Ni multilayers with layer thickness from 200 nm to 6 nm and annealing temperature up to 500 ℃ led to the establishment of a coupled layer-thickness and annealing-temperature dependent strengthening mechanism map. For annealed films, grain boundary relaxation is considered to be the initial strengthening mechanism with higher activation temperature required for thicker layers. Under further annealing, solid solution hardening, intermetallic precipitation hardening, and fully intermixed alloy structure continue to strengthen the thin layered films, while recrystallization and grain growth lead to the eventual softening of thick layered films. For films with intermediate layer thickness, a strong orientation dependent hardness behavior is exhibited under high temperature annealing due to mechanism switch from grain growth softening to intermetallic precipitation hardening when changing the loading orientation from perpendicular to parallel to the layer interfaces.

Furthermore, deposition temperature induced texture evolution and mechanical strengthening were studied for Ti/Ni multilayer thin films deposited with elevated substrate temperatures up to 500 ℃. An obvious substrate-temperature dependent texture strengthening was observed. After low

temperature deposition, preferred crystallographic texture were detected for both Ti and Ni layers, and columnar structure was observed to extend through layers, leading to initial strengthening. The columnar structure became more distinct and complete with the increase of substrate temperature, and meanwhile more atomic diffusion and intermixing occur along the Ti/Ni interfaces, promoting the formation of Ti-Ni intermetallic precipitates, and the subsequent mechanical strengthening. After high temperature deposition, columnar Ti-Ni alloys were observed with disintegration of layered structure. Ti-Ni intermetallic was detected with preferred crystallographic texture. Recrystallization was observed with even higher deposition temperature, leading to even higher material strength.

Finally, a picosecond pulse laser was utilized to treat Ti/Ni multilayer thin films to induce desired microstructure change and surface strengthening. It was observed that with the increase of pulse-laser energy, the surface morphology evolves from homogeneous grain surface, to a cross-hatched pattern surface, and then to a rough melted surface covered with bubbles, voids and cracks. And the cross-section morphology evolves from a multilayered structure to partially intermixed and eventually fully intermixed structure. Due to the precipitation of Ti-Ni intermetallic phase, laser treatment with high pulse-energy led to surface strengthening on Ti/Ni multilayer thin films. In addition, the film and layer thickness effects on microstructural and mechanical properties were investigated using layer thicknesses of 20 nm and 50 nm, and film thicknesses 500 nm and 1 μm. It was found that thinner film and larger layer thickness requires the least energy to produce the intermixing effect while thicker film and smaller layer thickness requires a lot more energy to produce the desired intermix and mechanical strengthening.

TABLE OF CONTENTS

LIST OF FIGURES

LIST OF TABLES

ACKNOWLEDGEMENTS

First of all, I would like to express my deepest and sincerest gratitude to my advisor, Prof. Junlan Wang. During the more than six years we have worked together, she provided me immeasurable amount of guidance and support to improve my technical and communication skills, while still leaving me enough freedom to explore my interests and curiosities. I appreciate all the discussions and suggestions she provided throughout my entire graduate school life.

I would like to thank Prof. Jiangyu Li, Prof. Ramulu Mamidala and Prof. Fumio Ohuchi for serving on my dissertation committee. I have benefited a lot from the discussions with these intelligent, knowledgeable and thoughtful professors. I would also like to thank all the faculty and staff in the Department of Mechanical Engineering as well as the Materials Science Department at the University of Washington for offering many interesting courses and generous help in my day-to-day graduate study.

I would like to thank many of the past and current members of my research group. In particular, during my early period in graduate school, Dr. Jie Lian (now at Flextronic, InC., CA) provided me crucial help and training on the molecular dynamics simulation projects. I enjoyed and benefited from the numerous discussions with several other past lab members including Dr. Wu-feng Yeh (now at InvenSense, Inc., CA), Dr. Philip Miller (now at Los Alomos National Lab, NM), Dr.

Gabriel Chow (now at Triple Ring Tech., CA), and current members including Mark Miller, Melicent Stossel, Qian Tong, and Yang Zhou.

I would like to thank the technical staff at the UW Molecular Analysis Facility, Scott Braswell, Dr. Micah Glaz, Gerry Hammer, and Washington Nanofabrication Facility, Dr. Darick Baker and Duane Irish, for their help and training in using the various advanced imaging and analysis tools. I would like to express my appreciation to Prof. Jiangyu Li and his students Dr. Feiyue Ma and Peiqi Wang for their help with furnace-annealing and some preliminary AFM imaging. I would also like to express my appreciation to Prof. Ohuchi and his student Bo Zhao for helping me with some exploratory XPS testing.

I would like to thank all of my friends here in Seattle, including Huimin Guo, Yuanzheng Gong, Peiqi Wang, Di Zhang, Ya Zhao, Feiyue Ma, Chihao Li, Yan Han, Lei Wang, Long Gui, Cory Moore and many others, for the great time and fun memories we held together.

Last but not least, I would like to express my forever gratitude to my family: my wife Liwen Shu, my parents, my sister and my grandparents. It is impossible for me to complete my PhD without their support and encouragement.

Thanks and love all of you!

DEDICATION

To my beloved family,
my wife, dad, mom, sister, grandmother, grandfather
for their endless love, support and encouragement

Chapter 1. INTRODUCTION

1.1 MOTIVATION: ULTRA-STRENGTH PHENOMENA

Recent experiments on nanostructured materials have revealed a very interesting ultra-strength phenomena in a variety of materials systems, with materials strength reaching over 10% of their ideal strength [1]. The ultra-strength phenomena have attracted increasing attention because they not only deal with the traditional concerns of mechanics of materials, such as shape stability and deformation kinetics of materials under stress and temperature, but also the functional properties of materials. A brief review of ultra-strength materials can be found by Zhu and Li [1, 2], and Fig. 1.1 shows a schematic of the development of ultra-strength materials based on this review and the representative examples, including bulk nanocrystalline and nanotwinned materials, thin films, multilayers, micro/nano pillars, nanowires, nanotubes, nanoparticles, and graphene. Early in 1950s, the ultra-strength was observed in the tensile testing of ceramic and metallic whiskers. The whiskers were fabricated with diameter in μm scale, however, the strongest whiskers were observed to have a strength up to 2 – 6% of their modulus [3, 4]. In the last two decades, a large number of nanostructured materials have been synthesized, including nanocrystalline materials, nanotwinned materials [5-7], thin films and multilayers [8-10]. The material strength is found to dramatically increase with decreasing feature size, such as the grain size in nanocrystalline and thin film materials, twin spacing in nanotwinned materials, and layer thickness in multilayers. In 2004, micro-pillar was for the first time sculpted out from a substrate by using focused ion beam (FIB) [11], and since then extensive studies have been performed based on mechanical testing of micro-pillar and nano-pillars [12, 13]. For example, Greer and Nix demonstrated that sub-micron-

gold pillars can be 50 times stronger than their bulk counterparts [13]. Going down in characteristic size scale, nanowires [14, 15], nanotubes [16, 17] and nanoparticles [18], all demonstrated super high strengths, approaching to their ideal strength, with their characteristic length scale approaching a few tens of nanometers. An extreme limit is a monolayer graphene. An AFM based nanoindentation was applied to measure the strength of the graphene, and the measured strength (130 GPa) almost approaches the ideal strength calculated by *ab initio* from quantum mechanics (~130 GPa) [19].

While the ultra-strength materials demonstrated the possibility to achieve both superior mechanical and functional properties, there are still challenges that have to be overcome in order to have a comprehensive understanding of this special class of materials, which are roughly summarized as following:

(a) How to reliably synthesize the ultra-strength material systems;

(b) How to experimentally control the loading and measure the stress/strain using advanced, miniaturized instrumentation;

(c) How to measure, understand and predict the dependencies of physi-chemical properties, including electronic, magnetic, optical, phononic, thermoelectric and catalytic, etc.;

(d) How to understand the different deformation and strengthening mechanisms.

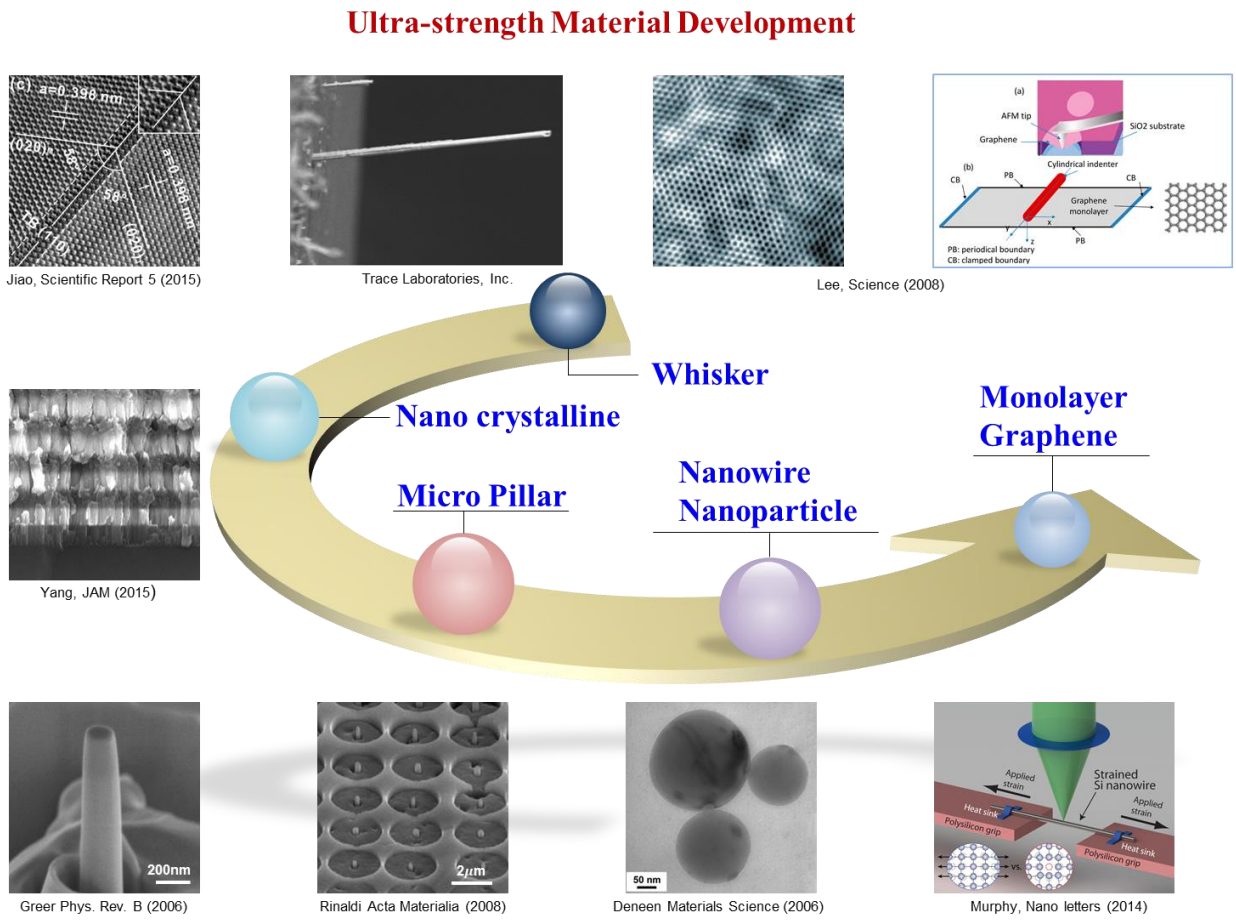

Figure 1.1: Schematic of the development of ultra-strength material systems: whiskers in 1950s, a large number of nanocrystalline materials in the last two decades including bulk nanocrystalline and nanotwinned materials, thin films, multilayers, micro/nano pillar, 1D nanowires and nanotubes, 0D nanoparticles and recent monolayer graphene.

1.2 BACKGROUND OF THIN FILMS AND MULTILAYERS

As a special type of ultra-strength material, thin films or multilayers have attracted a lot of attention in the research and technology fields, such as various functional coatings in optics, electronics, biotechnology and energy. [20, 21].

The thin film materials in the aforementioned applications can be developed with many different deposition methods, among which physical vapor deposition (PVD) and chemical vapor deposition (CVD) are the two most common ones. During the PVD process, material atoms are transferred to the growth film surface with the facilitation of physical processes, such as evaporation, sublimation or ionic impingement. Evaporation and sputtering are the two most widely used PVD methods for depositing thin films, while a chemical reaction between the source material and suitable gases facilitates the atomic deposition in CVD process. There are also variants of the CVD process applied to specific situations, such as low-pressure CVD (LPCVD) and plasma-enhanced CVD (PECVD) which are mostly used in semi-conductor fabrication [22].

A comparison of the typical thin film deposition methods is shown in Table 1. 1, and it can be seen that the specific deposition method can have a significant effect on film microstructure, such as average grain size, grain shape, grain size distribution and crystallographic texture. On the other hand, the fabrication process almost always results in internal or residual stress which can induce mechanical deformation, damage or even failure. Both the presence of an internal/residual stress and film microstructure can have significant influence on thin films material properties – electrical, magnetic, optical, mechanical, and thus affect device performance [22].

Multilayer thin film is a special class of composite material with alternating layers of two (or more in some cases) different materials. The individual layer thickness can range from a few nanometers to a few hundreds of nanometers. Multilayered films have attracted more and more attention due to their advanced material properties and wide technological applications [23]. For example, multilayered films can be used as magnetic recording media [24-26], X-ray mirrors [27-29] and wear resistant coatings [30] due to their specific magnetic, optical and mechanical properties. In addition to provide various applications in advanced engineering, multilayer thin film systems are considered as model systems for many fundamental studies such as strengthening mechanism dependence on length scale [31-33], thermal stability on interface structure [34-38], and solid state reaction induced solid state amorphization [39-41].

Table 1.1: Comparison of typical thin film deposition methods.

Process	Thermal Evaporation	E-beam Evaporation	Sputtering	PECVD	LPCVD
Material	Metal/ low melting -point material	Both metal and dielectrics	Both metal and dielectrics	Mainly dielectrics	Mainly dielectrics
Uniformity	Poor	Poor	Very good	Good	Very good
Impurity	High	Low	Low	Very low	Very low
Grain Size	10-100 nm	10-100 nm	10-100 nm	10-100 nm	1-10 nm
Film Density	Poor	Poor	Good	Good	Excellent
Deposition Rate (Å/S)	1~20	10 ~100	Metal: ~100 Dielectrics: 1-10	10 ~100	10 ~100
Directional	Yes	Yes	Some degree	Some degree	Isotropic
Cost	Very low	High	High	Very high	Very high

1.3 INTRODUCTION TO Ti/Ni MULTILAYER THIN FILMS

Metallic multilayer thin films display unusual chemical, structural, electrical, magnetic, optical and mechanical properties when the structure periodicity is on the order of a few nanometers. Among the various multilayer thin film systems, Ti/Ni multilayer thin film structure is of special interest due to its superior optical and mechanical properties. In addition, Ti/Ni multilayer thin films are widely used in many technological applications from various fields, such as in the design of MEMS and medical devices.

One of the major applications of Ti/Ni multilayer thin film is in the field of soft X-rays and neutron optics [42-45]. Ti/Ni multilayer thin film with periodicity several nanometers can be designed as highly reflecting mirrors, supermirrors and polarizers. For example, an X-ray mirror made of Ti/Ni multilayers with periodicity 1 ~ 2 nm was proven to display high reflectance and excellent polarization efficiency in the water window (energy E: 280 ~ 530 eV /wavelength λ : 2.3 ~ 4.4 nm) [45]. In addition to the optical applications, Ti/Ni multilayer thin film was found to be useful in a new fabrication process of Ti-Ni shape memory alloy [46-50], which has been broadly applied in MEMS such as cantilevers and actuators [51], and medical field such as self-expanding vascular stent made of superelastic nitinol (Ti-Ni alloys) [52, 53]. Previously, alloyed Ti-Ni targets were used by conventional sputtering deposition method. The new fabrication process is to achieve Ti-Ni alloys by post processing sputtering-deposited Ti/Ni multilayer thin films, such as thermal annealing and ion implantation. By this new fabrication process, the composition of Ti and Ni in the alloy film can be controlled precisely by adjusting sputtering power and sputtering time for Ti and Ni layers respectively, and thus the type of Ti-Ni alloy can be also controlled.

In addition to the aforementioned applications, Ti/Ni multilayer thin films have been studied extensively as a model system to understand the fundamental phenomenon of solid-state reaction leading to solid state amorphization [39-41]. The reaction leading to amorphization only works on material systems which can satisfy several main conditions such as a large difference in Gibbs free energy of intermixing and anomalous fast diffusion of one material atom into another material layer. Besides, interface structure is also important, since the nucleation of the amorphous phase is found to be dependent on the presence of incoherent or disordered interface structure. Ti/Ni multilayer thin films display a large negative heat of mixing, indicating that the Ti-Ni amorphous alloy has a lower free energy than the two-phase mixture of crystalline elements. Thus the large difference in free energy in Ti/Ni multilayer system is the thermodynamic driving force for this solid state reaction. In addition, Ni atoms are more mobile than Ti atoms in this system and would start diffusing into Ti layer during low temperature annealing [39-41, 54]. Combining these two advantages, Ti/Ni multilayer thin films were selected to investigate more details about the solid-state amorphization, such as interfacial microstructure dependence on amorphization process.

Although the majority of existing works on Ti/Ni multilayer thin films focus on either optical property, fabrication process of Ti-Ni alloys or fundamental solid-state reaction, there are still a few others working on other properties of Ti/Ni multilayer system, such as structural, chemical and magnetic properties [38, 55], as well as thermal stability on layered structure [36].

1.4 Overview of Strengthening Mechanisms of Metallic Material

Understanding the deformation behavior and strengthening mechanism has been one of the most challenge tasks for ultra-strength material systems. In general, nanocrystallized material and multilayer thin films can exhibit much higher strength than conventional material when the material feature size is in the range of nanometer [31, 33, 56]. The maximum strength can reach almost half of the theoretical value for metallic multilayer structure when the individual layer thickness is in the range of a few nanometers. Fundamentally, there are only two ways to approach the theoretical strength: by either eliminating all dislocations [13] or creating as many and as powerful barriers for dislocation motion as possible [56].

Work hardening or strain hardening is one of the most important strengthening mechanisms for metallic material. Fig.1.2 shows a schematic of stress-strain curve for an elastic-ideally plastic solid and a work-hardening solid. For a real crystalline solid, hardening can be achieved after plastic loading. During plastic deformation, dislocations move and interact directly with each other and other imperfections, or indirectly with internal stress field of various imperfections and obstacles. All of these interactions can significantly reduce the mobility of dislocations and as a result larger stress is required to achieve further dislocation movement. However, the work hardening behavior is difficult to predict since the density and distribution of dislocations with respect to the plastic strain is unpredictable. Experimental observation shows a linear relationship between the flow stress τ and the square root of the dislocation density ρ as following [57]:

$$\tau = \tau_0 + \alpha G b \sqrt{\rho} \tag{1.1}$$

where τ_0 is the stress necessary to move a dislocation in the crystalline solid, α is a constant (0.3 ~ 0.6), G is shear modulus and b is Burgers vector.

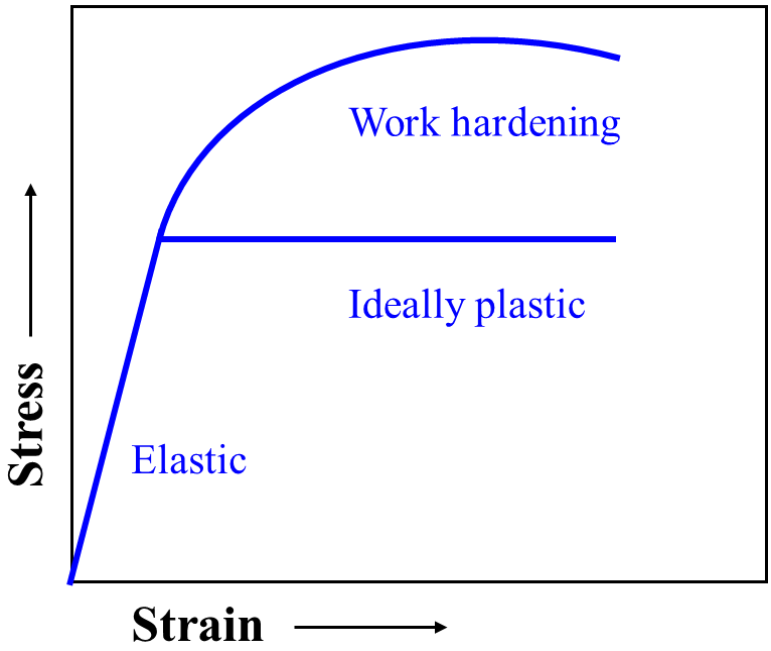

Figure 1.2: Schematic of stress-strain curve of an elastic-ideally plastic solid and a work hardening solid for the demonstration of strain hardening or work hardening.

Another common approach of creating barriers to reduce dislocation mobility is to introduce heterogeneity into crystalline solids, such as solid solutions, precipitates or hard particles, and the corresponding strengthening is named as solid solution hardening or precipitation hardening. In this scenario, the impurity atoms can distort the lattice and generate local shear stress field. Much

higher stress is thus required to move a dislocation in the presence of local shear stress fields. A typical example is continuously strengthened steels with increased carbon solute content.

For polycrystalline material, grain boundary can impede dislocation propagation due to the orientation discontinuity between two adjacent grains. In general, material with small grain size can display higher strength because more grain boundaries provide more barriers to dislocation motion. This trend can be represented by the well-known Hall-Petch equation:

$$\sigma_y = \sigma_0 + k / \sqrt{d} \tag{1.2}$$

where σ_y is the yield stress, σ_0 is a frictional stress required to move a dislocation into material, and d is the grain size. This equation was originally introduced by Hall and Petch to describe the lower yield point of low-carbon steels as a function of grain size, and now has been successfully applied to many systems, such as nanotwinned material and multilayer thin films. For example, in multilayer system, individual layer thickness is generally applied in Hall-Petch relation instead of grain size to describe the dislocation strengthening due to dislocation pile up against the interfaces of layered structure.

In addition to dislocation pile up strengthening mechanism, another common dislocation strengthening mechanism is dislocation bowing. In nanotwinned materials and multilayer thin films, single dislocation bowing within layers is found as applicable mechanism when the feature size is ranged from a few nanometers to a few tens of nanometers. In addition, these two different dislocation strengthening mechanisms can be switched by changing the loading orientation. Dislocation pile up dominates with the activated slip system in which both slip plane and slip direction are inclined to interfaces, while dislocation bowing dominates with the activated slip

system in which slip plane inclined to interfaces, and slip direction parallel to interfaces. A schematic of these two dislocation strengthening mechanisms with different loading orientation in multilayer system is shown in Fig. 1.3 based on our current work [31].

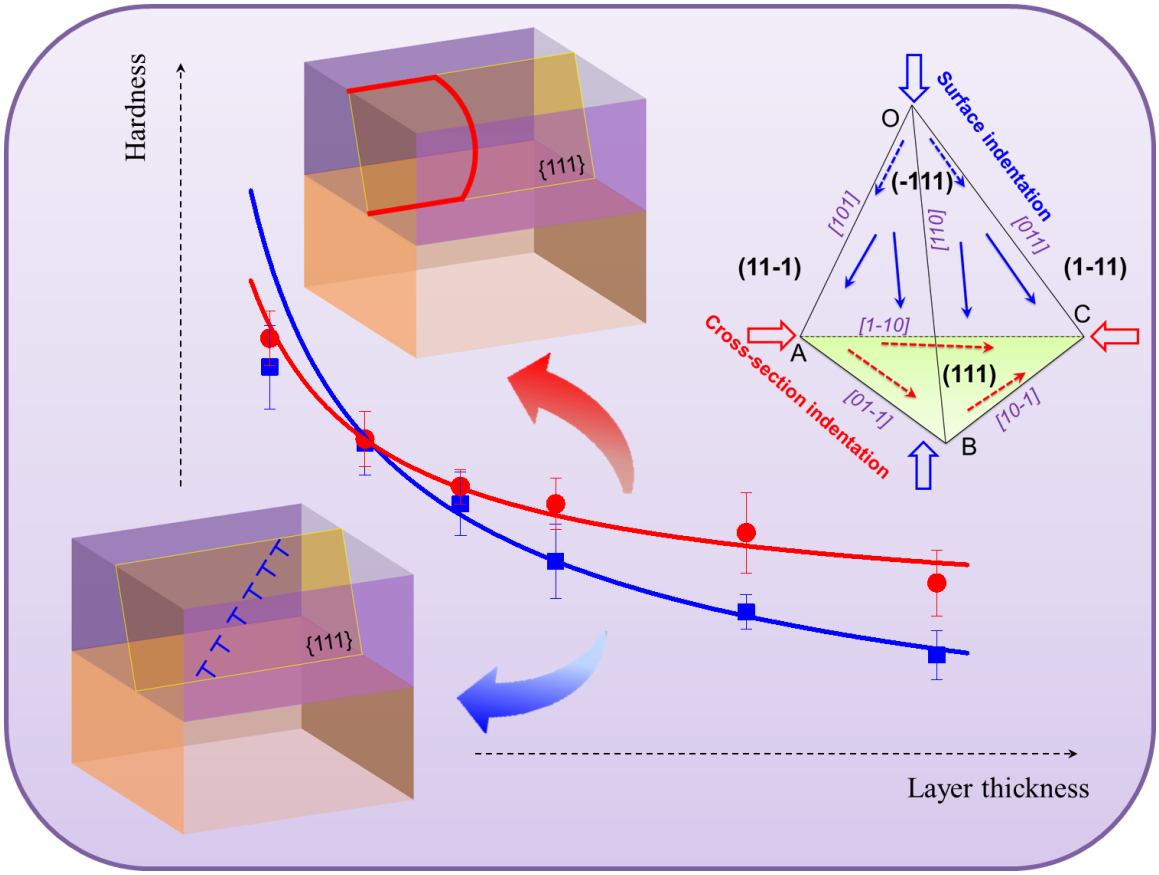

Figure 1.3: Schematic of two common dislocation strengthening mechanisms with different loading orientation in multilayer thin film systems. Dislocation pile-up (blue case) dominates in slip system with both slip plane and slip direction inclined to interface, while dislocation bowing (red case) dominates in slip system with slip plane inclined to interface and slip direction parallel to interface.

Dislocation starvation and defect-free are two common mechanisms for nanostructured materials by eliminating defects [13]. For example, in pillars, very few dislocations present, and they cannot multiply sufficiently before they are annihilated at free surfaces, leading to a dislocation-starved state. High stresses are thus required to nucleate new mobile dislocations.

There are still many other mechanisms to strengthen materials such as fiber reinforcement for composite material, martensitic strengthening, ordering strengthening (to achieve more ordered crystal), and texturing strengthening. Besides, there are some strengthening processes, which may combine more strengthening mechanisms at the same time. For example: thermomechanical processing (TMP) or treatment (TMT) introduces plastic deformation into thermal treatment cycle to improve mechanical strength by using the synergistic effect of the mechanical treatments (interstitial atoms, line defects, stacking faults, etc.) and thermal treatments (precipitates, martensite); Radiation damage can harden metallic material by creating a large number of interstitials and vacancies; and pulsed laser treatment has been extensively used to hardening the metal surface. [57]

1.5 OBJECTIVES AND ORGANIZATION OF THE DISSERTATION

For multilayer thin films, one of the biggest challenge today is to fully understand the deformation behaviors and strengthening mechanisms. Furthermore, materials could be likely exposed to thermal environment during manufacturing or service. Therefore, the coupled size and temperature effect can have significant consequence on the shape stability and deformation kinetics of the materials.

The overall objective of this dissertation is to understand the coupled size and temperature effect on thermo-mechanical stability and strengthening mechanisms of metallic multilayer thin films. Size effect comes from different individual layer thickness in different samples. Thermal sources come from either post-deposition annealing, in-situ high temperature deposition, or localized surface annealing by ps pulse-laser irradiation. For all the studies, Ti/Ni was chosen as the model system due to a) the wide-spread application of these materials as discussed in section 1.3 and b) the fact that Ti/Ni serves as a nice combination of an hcp/fcc structures to reveal the different strengthening mechanisms on an incoherent bimaterial interface.

In this dissertation, the investigation of deformation behaviors and strengthening mechanisms of metallic multilayer thin films will be introduced from room temperature deposited samples, to post deposition annealed samples, high temperature deposited samples, and then to pulse-laser treated samples.

Chapter 1 briefly describes the motivation of the study and the necessary background information of thin film and multilayer materials, Ti/Ni multilayer thin films and strengthening mechanisms of metallic materials, as well as the objectives and organization of the dissertation.

Chapter 2 provides an overview of the experimental techniques utilized in this research. A magnetron sputtering system was used to deposit the Ti/Ni multilayer samples used in all studies. For mechanical characterization, a Ubi1 nanomechanical test system was used to carry out all the nanoindentation experiments. For microstructure characterization, scanning electron microscopy (SEM) was widely used to obtain the surface and cross-section morphologies of the Ti/Ni multilayer samples and transmission electron microscopy (TEM) was used to capture detailed cross-section morphology and crystal structure for selected samples with ultra-thin individual layers. Atomic force microscopy (AFM) was occasionally used to obtain the topography for laser treated samples. X-ray diffraction (XRD) was also widely applied to obtain crystallinity information for samples. X-ray photoelectron spectroscopy (XPS) was used to characterize the elemental composition, and mostly to obtain the depth profile for multilayers with an Ar ion sputtering gun.

In chapter 3, the length scale effect (individual layer thickness) on the Ti/Ni multilayer strength was first experimentally investigated, and two dislocation models adapted from literature were applied to quantitatively analyze the dislocation motions with different layer thickness. Then orientation effect was studied by indenting on both surface and cross-section of samples. For cross-section indentation, mechanical polishing was applied to achieve smooth area, and the corresponding polishing induced hardening effect was also discussed. Furthermore, dislocation

models were also applied to understand the deformation and strengthening mechanisms associated with different loading orientations, as well as polishing process.

In Chapter 4, coupled layer thickness and annealing temperature effect was discussed on the Ti/Ni multilayers. Samples with a wide range of layer thickness from 200 nm to 6 nm were annealed at different temperature from 100 ℃ to 500 ℃, and then indented on both surface and cross-sections. With detailed microstructure characterization and mechanical testing, a schematic strengthening mechanism map was proposed with respect to the coupled size and thermal effect. In addition, a strong orientation effect on the mechanism boundary was observed.

In Chapter 5, another type of thermal effect from substrate temperature was studied. The detailed influence on texture evolution and material strength of Ti/Ni multilayers was discussed. First, substrate temperature effect was studied on samples with layer thickness 20 nm with a wide range of temperature from 100 ℃ to 500 ℃. Then, a coupled size and thermal effect was investigated with individual layer thickness from 250 nm to 10 nm, and deposition temperature under 300 ℃.

In Chapter 6, localized surface annealing was applied on Ti/Ni multilayers by using picosecond pulse-laser irradiation. The detailed effect from pulse-laser energy and thickness – both layer thickness and film thickness – were studied on the microstructure evolution and surface mechanical property modification. A wide range of laser energy from 25 mJ to 150 mJ was performed on four types of samples with different film thickness/layer thickness combination – 500 nm/20 nm, 500 nm/ 50nm, 1 μm/20 nm and 1 μm/50 nm.

Chapter 7 summaries the current results and proposes some future directions.

In Appendix, the detailed nanoindentation procedure was shown and the elastic modulus results for Ti/Ni multilayer thin films were discussed.

1.6 PUBLICATION LIST

Zhou Yang, Jie Lian, Junlan Wang, "Molecular dynamics simulation of thin film interfacial strength dependency on lattice mismatch", Thin Solid Films, 537 (2013) 190-197.

Zhou Yang, Junlan Wang, "Orientation-dependent hardness in as-deposited and low-temperature annealed Ti/Ni multilayer films", Journal of Applied Mechanics, 82(1) (2015) 011008.

Zhou Yang, Junlan Wang, "Coupled annealing temperature and layer thickness effect on strengthening mechanism of Ti/Ni Multilayer thin films", Journal of the Mechanics and Physics of Solids, 88 (2016) 72-82.

Zhou Yang, Melicent Stossel, Junlan Wang, "Microstructural evolution and surface strengthening of pulse-laser treated Ti/Ni multilayer films", Extreme Mechanics Letter, 4 (2015) 45-51.

Zhou Yang, Melicent Stossel, Junlan Wang, "Thickness effect on microstructural and mechanical properties of pulse-laser treated Ti/Ni multilayer thin films", Journal of Applied Physics, 2016, to be submitted.

Zhou Yang, Qian Tong, Junlan Wang, "Deposition temperature-induced texture and strengthening of Ti/Ni multilayer thin films", Journal of Applied Mechanics, 2016, to be submitted.

Zhou Yang, Qian Tong, Junlan Wang, "Size-dependent texturing of low-temperature deposited Ti/Ni multilayer thin films", 2016, to be submitted.

Chapter 2. EXPERIMENTAL TECHNIQUES

Microstructure and mechanical property characterizations are important for strengthening mechanisms investigation for metallic multilayer thin films. This chapter provides a brief overview of the sample preparation and characterization techniques utilized in this dissertation.

2.1 MAGNETRON SPUTTERING THIN FILM DEPOSITION

As introduced in Chapter 1, sputtering is one of the most popular PVD processes to deposit material atoms onto a substrate. A basic sputtering process is shown in Fig. 2.1. Argon atoms are introduced into a vacuum chamber. A direct current (DC) voltage is placed between the target and substrate which ionizes the electrically neutral Ar atoms and thus creates plasma, hot gas-like phase consisting of ions and electrons. The charged Ar ions are accelerated to the cathode target. Their collision with the target ejects target atoms, which travel to the substrate and eventually settle in the substrate. Electrons released during Argon ionization are accelerated to the anode substrate, subsequently colliding with additional Ar atoms, creating more ions and free electrons in the process, continuing the cycle.

Magnetron sputtering is a more enhanced version of the above sputtering process. The main difference between this and a basic DC sputtering system is the addition of a strong magnetic field near the target area. This magnetic field causes electrons to spiral along magnetic flux lines near the target instead of being attracted toward the substrate as shown in Fig. 2.2. The advantage of this is that the plasma is confined to an area near the target, without causing damages to the thin

film being formed. Also, electrons travel for a longer distance, increasing the probability of further ionizing Argon atoms. This tends to generate a stable plasma with high density of ions. More ions mean more ejected atoms from the target, therefore, increasing the efficiency of the sputtering process. The faster ejection rate, and hence deposition rate, minimizes impurities to form in the thin-film, and the increased distance between the plasma and substrate minimizes damage caused by stray electrons and Argon ions.

Table 2.1: As-deposited Ti/Ni multilayer thin films in different projects with different layer thickness and film thickness

Projects	Film Thickness (μm)	Layer Thickness (nm)
As-deposition	4 for thick layer 2 for thin layer	200 - 6
Annealing		
Deposition Temperature	1	167 - 10
Laser Treatment	1 & 0.5	50 & 20

In this dissertation, Ti/Ni multilayer thin films were fabricated by using a dual d.c. magnetron sputtering system (Orion-5-UHV from AJA International, Inc, MA). Ti (99.995%) and Ni (99.999%) targets were used as the two sputtering sources, and single crystal Si (100) wafers were used as substrates. Alternating Ti and Ni layers were deposited on the Si substrate with Ti being the first layer and Ni being the last layer. The background pressure of the main sputtering chamber was around 1×10^{-7} mbar, and the depositions were carried out with the argon gas pressure around 1×10^{-3} mbar. The Ti and Ni targets were sputtered at d.c. powers of 100 W, and the sputtering time of each layer was controlled to maintain the desired individual layer thickness. The sputtering rates

for Ti and Ni were calibrated to be 2.44 and 3.37 nm/min respectively. The Ti layer has the same thickness as the Ni layer in each sample. Table 2.1 lists all the samples deposited for different projects with different layer thickness and film thickness.

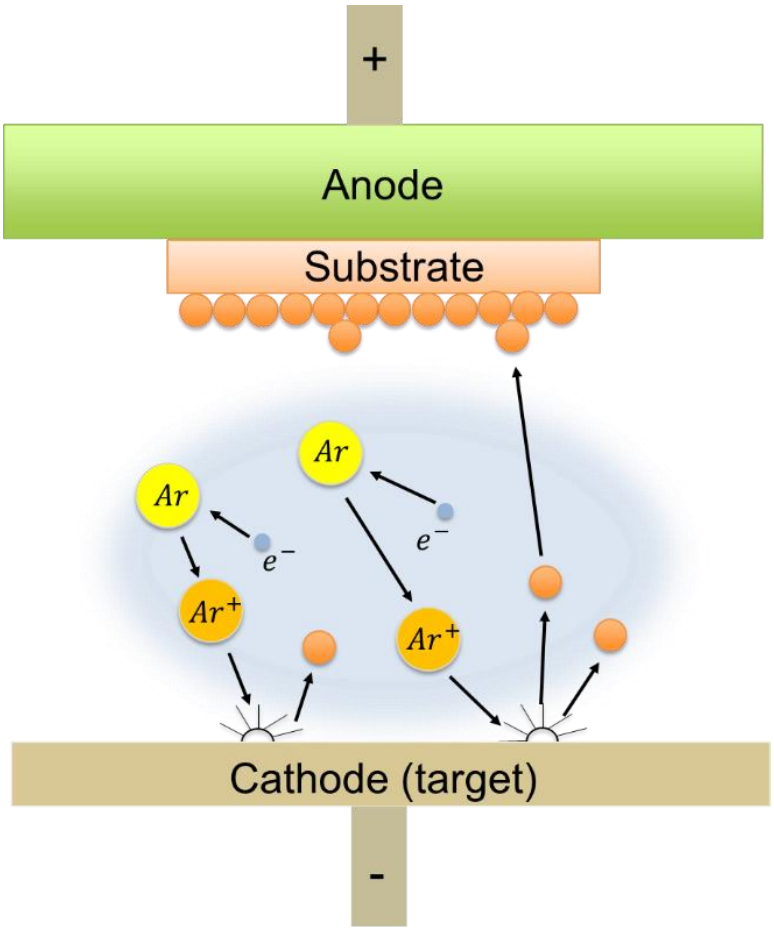

Figure 2.1: A schematic of basic sputtering process: electrical field is formed between target and substrate, and the plasma is created in the vacuum chamber. Ar ion strikes the target, and target atoms move to substrate, forming the film.

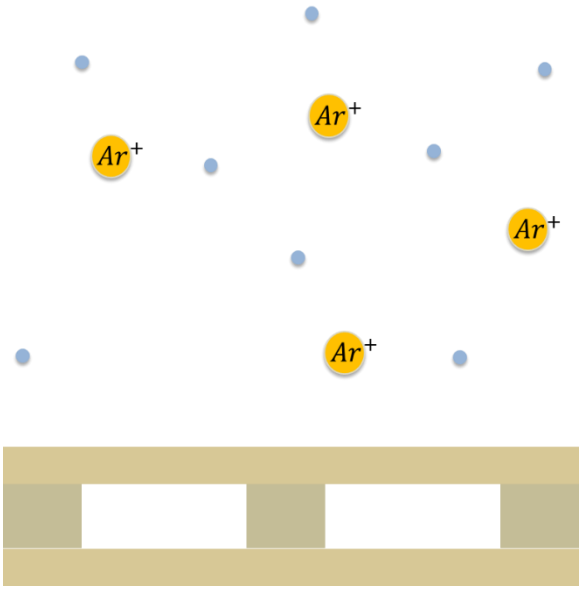

(a)

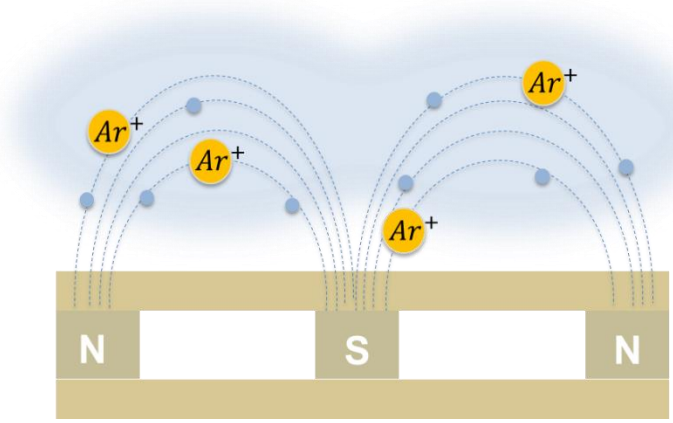

(b)

Figure 2.2: Schematic of the difference between (a) basic sputtering process and (b) magnetron sputtering process. The plasma is confined within an area near the target in the magnetron sputtering process, increasing the efficient of the whole sputtering process.

2.2 MICROSTRUCTURE CHARACTERIZATION TOOLS

2.2.1 Scanning Electron Microscopy

Scanning Electron Microscopy (SEM) is one of the most popular tools to image a sample by scanning surface with a focused electron beam, and has been widely applied to observe microstructure for thin film materials, such as grain size and shape, grain distribution, and film thickness. The electron beam interacts with atoms of sample surface, producing secondary electrons and backscattered electrons from the sample. These secondary electrons or backscattered electrons are collected by a secondary detector or a backscattered detector, and then converted to voltage signals, and amplified by electronic amplifiers. The resulting image is therefore a distribution map of the reflected signal intensity from the scanned area of the sample surface. SEM has a large depth of field to allow large amount of sample surface focused at one time. SEM can also achieve very high resolution on the order of 1 nanometer. In addition, sample preparation for SEM experiments is simple. For non-conductive sample, a thin layer of electrically conductive material such as gold or palladium is coated before SEM.

In this work, SEM (FEI Sirion XL30) located in UW Molecular Analysis Facility (MAF) was used extensively to capture both surface and cross-section morphologies for Ti/Ni multilayer thin films. The average grain size with respect to individual layer thickness can be obtained by analyzing the information from SEM images. Both surface and cross section morphological evolution can be revealed by these SEM images with the increasing of annealing temperature or substrate temperature. For laser treated samples, SEM images also show the modification of surface and cross section morphology after laser treatment.

2.2.2 Transmission Electron Microscopy

Transmission Electron Microscopy (TEM) is another powerful microscopy technique which uses a high energy electron beam transmitted through an ultra-thin specimen to image and analyzes the microstructure of sample material. The transmitted beam contains information about electron density, phase and periodicity, which is used to form an image. The image is then magnified and focused onto a fluorescent screen or detected by a CCD camera. TEM has a wide-range of applications and can be utilized in a variety of different scientific, educational and industrial fields. TEM provides both high resolution images with resolution about 1 ~ 2 Å by image mode and crystal information by diffraction mode for sample material.

In this work, TEM (FEI Tecnai) located in UW Molecular Analysis Facility (MAF) is used to confirm layered structure and crystallinity for Ti/Ni multilayer with ultra-thin individual layers (12 nm and 16 nm cases). However, the preparation of cross section samples for TEM is time-consuming. A brief summary of cross section TEM sample preparation is descripted as following:

Step 1 - Cutting several sample slices of 2 mm width and 4 - 6 mm length

Step 2 - Forming a stack with the above slices by using epoxy glue and then annealing

Step 3 - Embedding the stack in a Cu tube (3mm diameter) and filling it with epoxy

Step 4 - Cutting the Cu tube into disks of about 300 - 400 microns thickness

Step 5 - Mechanically polishing the disk down to a thickness of 80 -120 microns

Step 6 - Dimple-grinding with a dimpling wheel to leave 15 - 20 microns in the middle

Step 7 - Ion milling the center of dimple-grinded sample until a hole appears

2.2.3 Atomic Force Microscopy

Atomic Force Microscopy (AFM) has been widely applied to image surface topography with a very high resolution on the order of fractions of a nanometer. AFM utilizes an ultra-sharp tip (radius of curvature on the order of nanometers) mounted on a cantilever to scan the sample surface. Once the tip is brought closely to the sample surface, the interaction forces between the tip and material atoms can cause deflections of the cantilever, which can be measured by using a laser spot and then used to image the surface topography. Depending on the applications, there are three different AFM imaging modes: contact mode with tip-sample in soft contact, tapping mode in which the cantilever oscillates at resonant frequency and the tip contacts the sample surface at the bottom of vibration, and non-contact mode in which tip is separated from the sample and vibrates above the sample surface during scanning. Unlike the electron microscope, AFM can provide a 3D surface profile. There is almost no specific sample preparation by using AFM, and AFM can work perfectly well in ambient air environment, although with a small scan area usually below 100×100 μm.

In this work, AFM (Veeco Dimension 3100) was occasionally used to obtain surface morphology for high-temperature annealed Ti/Ni multilayers, especially for samples with thin layer.

2.2.4 X-ray Diffraction

XRD is the most commonly used tool to determine the crystal structure of sample material. For x-ray diffraction method, the normal spacing d between adjacent crystallographic planes is determined by means of Bragg's law as following:

$$d = \frac{n\lambda}{2\sin\theta} \tag{2.1}$$

where n is an integer, λ is the wavelength of the x-ray beam incident on the film and θ is the angle of incidence and reflection. In XRD, x-rays with wavelength λ are incident to the sample material with certain angles, and the diffracted x-rays are collected by a detector placed at 2θ from the transmitted x-ray beam. That is why the intensity of the scattered x-ray beam is usually monitored as a function of 2θ. From the Bragg's equation, it can be seen that only when the incident angles meet Eq. (2.1), there are peaks in the intensity plot, which provides precise spacing information of crystal planes in sample material. With XRD data, the crystalline phases can be identified by the peak positions and the average crystalline size and strain can be estimated by both peak positions and peak widths.

In this dissertation proposal, all the XRD experiments were done by utilizing a Bruker D8 Discover with GADDS XRD system. The source was Cu Kα radiation, running at 40 kV and 120 mA.

2.2.5 X-ray Photoelectron Spectroscopy

XPS is one of the most widely used surface analysis techniques to characterize the elemental composition. In XPS, Al Kα radiation or Mg Kα radiation are commonly employed as the x-ray source. The x-ray beam is directed at the sample material resulting in core-level electron emission (photoemission) in an atom near the surface (0 ~ 10 nm). The emitted electrons can be detected

and the corresponding kinetic energies are measured. The energy of an x-ray with known wavelength is also known, for example, for Al Kα x-ray, E=1486.6 eV, and for Mg Kα x-ray, E=1253.6 eV. Due to the conservation of energy equation in Eq. (2.2), the electron binding energy of the emitted electrons can be determined:

$$E_{binding} = E_{photon} - E_{kinetic} \tag{2.2}$$

where $E_{binding}$ is the binding energy, E_{photon} is the energy of x-ray photons, and $E_{kinetic}$ is the kinetic energy of the emitted electrons. The binding energy is determined primarily by the attractive force by the electron for the nucleus of the atom, and thus the binding energy is specific for each electron shell in an element, and these binding energies vary from element to element. So the elements can be determined by using binding energies, and the relative composition of the constituents can be further determined by analyzing the binding energy peaks.

In this dissertation, all the XPS works were carried out by a Phi Versaprobe 5000 XPS system to obtain the elemental depth profile of Ti/Ni multilayer sample. The XPS system utilizes an Al Kα x-ray and collects emitted electrons with an SSL-300 Hemispherical Analyzer. The depth profile of sample material was achieved by combining a sequence of Ar ion sputtering cycles with XPS survey scans from the current surface. After each survey scan, the Ar ion gun was used for sputtering the surface material to expose a new surface for next survey scan. The set of XPS spectra was analyzed to different element composition with respect to depth.

2.3 NANOINDENTATION

Nanoindentation has been widely applied on small volume of materials to measure various mechanical properties such as elastic modulus, hardness and wear resistance. So far it is one of the most popular tools for thin film materials due to its easy operation, few requirements on sample preparation, accurate software analysis as well as wide applications on many types of materials. The earliest indentation tests – microhardness test - were developed to measure hardness, and then expanded for other mechanical properties such as modulus and fracture toughness. It was not until the mid-1970s that the nanoindentation techniques were developed in which the indentation depth is continuously monitored and the analysis of the load-displacement curve yield both the modulus and hardness information for the indented samples.

During nanoindentation testing, an indenter tip with known geometry (e.g. Berkovich tip with three-sided pyramid geometry) is employed to penetrate into the material and then withdrawn from the material to leave an imprint on the surface following a prescribed loading, holding and unloading function. Fig. 2.3 (a) shows a schematic of deformation behavior during and after nanoindentation. Both elastic and plastic deformation occurs during the loading process, and the elastic portion is recovered after unloading. A typical load-displacement curve can be achieved after nanoindentation as shown in Fig. 2.3 (b), and the unloading part can be analyzed for the mechanical properties, such as elastic modulus and hardness [58, 59].

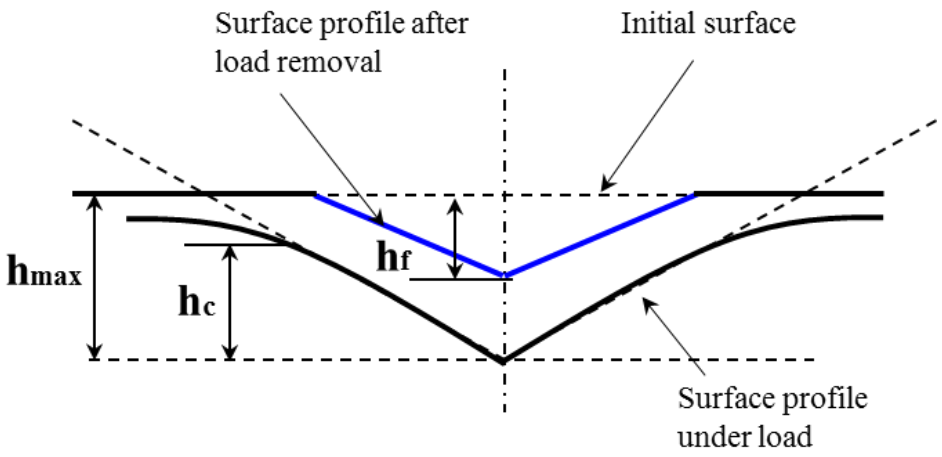

(a)

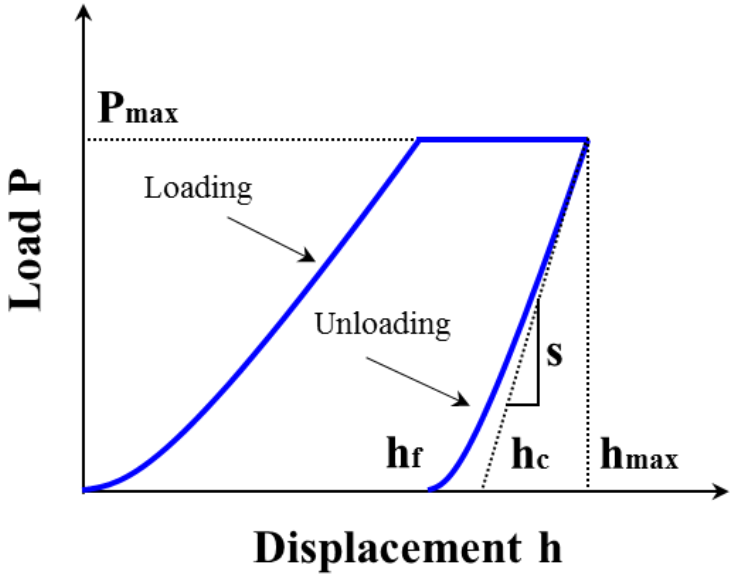

(b)

Figure 2.3: (a) Schematic of deformation behavior during and after indentation; (b) typical indentation load-displacement curve.

The nanoindentation hardness is defined as the maximum indentation load over the contact area:

$$H = \frac{P_{\max}}{A_c} \tag{2.3}$$

where H is the hardness of sample material, $P_{\max}$ is the maximum load and A_c is the contact area, which is a function of contact depth h_c. For a specific tip, the contact area can be obtained geometrically. For example, in the case of Berkovich tip, $A_c = 24.5h_c^2$. However, there are always defects and the tip is not perfectly sharp, and as a result, a modified area function with additional coefficients is calibrated to approximate the real tip by using a standard fused quartz. The calibrated area function is represented as following:

$$A_c(h_c) = C_0(h_c^2) + C_1(h_c) + C_2(h_c^{1/2}) + C_3(h_c^{1/4}) + ... + C_n(h_c^{2/2^n}) \tag{2.4}$$

where C_n are fitting coefficients. The contact depth can be estimated from the load-displacement data using Sneddon's equation as following:

$$h_c = h_{\max} - \varepsilon \frac{P_{\max}}{S} \tag{2.5}$$

where $h_{\max}$ is maximum contact depth, ε is a constant depending on the tip geometry (e.g., 0.75 for a Berkovich tip and 0.72 for a conical tip), and S is the indentation stiffness. The stiffness is defined the slope of the initial portion of the unloading curve. Oliver and Pharr described the unloading curve by a power law of the following form:

$$P = a(h - h_f)^m \tag{2.6}$$

where h_f is the final depth, and a and m are empirically determined fitting coefficients. Then the stiffness can be calculated by differentiating P at the maximum depth of penetration shown in Eq. (2.6). With the known of stiffness, the contact depth can be determined, and so does projected contact area. Thus the hardness in Eq. (2.3) can be determined.

In addition, the reduced modulus can be obtained with the known of stiffness and projected contact area in Eq. (2.7). On the other hand, the reduced modulus can be expressed by Eq. (2.8).

$$E_r = \frac{\sqrt{\pi}}{2\sqrt{A_c}} S \tag{2.7}$$

$$\frac{1}{E_r} = \frac{(1-\nu_m{}^2)}{E_m} + \frac{(1-\nu_i{}^2)}{E_i} \tag{2.8}$$

where E_m and ν_m, E_i and ν_i are the elastic modulus and Poisson's ratio of the sample material and the tip respectively. For a diamond tip in nanoindentation experiments, Young's modulus is 1140 GPa, and Poisson's ratio is 0.07. Thus the elastic modulus of sample material can be determined.

In this dissertation proposal, all the nanoindentation experiments were carried out on an Ubi1 nanomechanical test instrument (Hysitron, Inc., MN) for all the Ti/Ni multilayer films, as-deposited, annealed and laser treated. In each single indent, the sample underwent a trapezoidal loading described by a 10 s loading, 5 s hold at maximum load, and 10 s unloading. A minimum of 20 indents were performed on each sample to obtain the average hardness value. In addition, scanning probe microscopy (SPM) images of the sample topography were obtained using the in-situ scanning capability of the nanoindenter and were used to ascertain the quality of indents.

Chapter 3. AS-DEPOSITED TI/NI MULTILAYER THIN FILMS - EFFECT FROM LAYER THICKNESS AND LOADING ORIENTATION

3.1 INTRODUCTION

Metallic multilayers can exhibit high strength close to theoretical values with individual layer thickness on the order of a few to a few tens nanometers [8-10]. An obvious layer thickness/size dependent hardness behavior is reported in extensive studies and three types of dislocation-based models have been proposed as the mechanisms of size strengthening for metallic multilayers [33]. A Hall-Petch model ($\sigma \propto h^{-1/2}$) based on dislocation pile-up along the interface is found applicable at length scales where dislocation pile-ups can be treated as a continuum ($h > 100$ nm) [60-62]. In the limit of a continuum of dislocations in the pile-up, the stresses at the tip of the pile-up are amplified by the number of dislocations in the pile-up and can attain theoretical shear and tensile strength levels to nucleate slip in the adjacent layer or nucleate a crack in the interface or adjacent layer. Consequently, the pile-up possesses a mechanical advantage to enable large-scale deformation at low applied stress levels. At sub-micrometer length scales, there are too few dislocations inside to be treated as a continuum and a modified Hall-Petch model ($\sigma \propto h^{-\alpha}$ where $\alpha \neq 0.5$) is used. In addition, the corresponding Hall-Petch slope indicating the resistance of interface can be utilized to estimate the peak strength of the multilayers. At smaller layer thickness with the few to a few tens of nanometers length scales, dislocation pile-up becomes difficult and a confined layer slip (CLS) model based on Orowan bowing is treated as the operative mechanism [63-65]. Several modifications to the CLS model such as dislocation core spreading along the

interface, interface stress and resistance from interface dislocation arrays are needed to achieve the correct functional dependence of CLS stress on layer thickness. The multilayer strength reaches a peak with layer thickness several nanometers, and the peak strength is set by the interface resistance to single dislocation transmission [66-68]. Other factors can be important to determine the barrier strength in different material systems such as coherent stress [67-69], misfit dislocation [67, 70], Koehler stress [56] and intermixing at the interface [71, 72]. Softening is usually observed with further reduced layer thickness due to the interface crossing by dislocations. In addition, for polycrystalline metallic multilayers, the diffusion-based mechanisms such as the grain boundary/interface sliding or Coble creep can also lead to material softening in this layer thickness range [73, 74].

For metallic multilayers, the loading orientation can be an essential factor governing the deformation behavior. With a change of loading orientation with respect to interface, the dominant effect of interface on dislocation motion can vary [32, 75], leading to loading/interface orientation-dependent plastic deformation, that is, anisotropic plasticity. Previous studies on metals and alloys attribute the anisotropic mechanical behaviors to crystallographic texture [76] and precipitates [77]. In addition, systematical works on anisotropic plastic deformations have been done in nanotwinned metals and alloys [78-80]. Three major deformation modes for dislocation interactions with twin boundaries (TBs) were proposed including dislocation glide in between the twins [81] in a hard mode I with both slip plane and slip direction of the active slip systems as well as the Burgers vector inclined to TBs, dislocation transfer across twin boundaries [82] in hard mode II with the slip plane inclined to TBs but the slip direction parallel to TBs, and dislocation-

mediated boundary migration in soft mode with both the slip plane and slip direction parallel to TBs [83].

In this work, the layer thickness dependency of multilayer strength was studied with a wide layer thickness range from hundreds nanometers to a few nanometers, and both surface indentation and cross-section indentation were carried out to investigate the loading/interface orientation effect. The dislocation based models were applied to fit experimental data for strengthening mechanism study.

3.2 EXPERIMENTAL DETAILS

Ti/Ni multilayer system with individual layer thickness ranging from 200 nm to 6 nm is utilized to investigate layer thickness and orientation dependent strengthening mechanism. The magnetron sputtering system is used for Ti/Ni multilayer thin films deposition and the detailed deposition method was introduced in previous Section 2.1. Based on the range of layer thickness, the deposited multilayers are divided into three categories: thick-layer cases with layer thickness 200 and 100 nm, intermediate-layer cases with layer thickness 50 and 25 nm, and thin-layer cases with layer thickness 16, 12, 8 and 6 nm. The nominal total film thickness is 4 μm in thick- and intermediate-layer cases and 2 μm in thin-layer cases.

For microstructure characterization, XRD was used to determine the crystallinity and SEM for both surface and cross-sectional morphology. For sample in thin-layer cases, TEM was performed to achieve the cross-section morphology and the corresponding diffraction pattern. For mechanical properties characterization, nanoindentation experiments were carried out with a cube corner indenter tip for all the Ti/Ni multilayer thin films. Cross section indentations were applied on polished cross section samples. For cross section sample preparation, two pieces of Si substrate with as-deposited Ti/Ni multilayer thin films were mounted face to face on the film side using an epoxy mounting compound. Then the cross-sectional sample was mechanically polished by using diamond discs of 75 μm and 20 μm grit, and diamond paste in successive grades of 9 μm, 3 μm, 1 μm and finally 0.25 μm on a Buehler polisher. For consistency, the corresponding surface samples were also polished to investigate the polishing effect.

3.3 MICROSTRUCTURE CHARACTERIZATION

3.3.1 XRD Spectra and Analysis

Fig. 3.1 shows the XRD spectra of as-deposited Ti/Ni multilayer thin films with individual layer thickness from 200 nm to 6 nm. In the thick-layer cases (200 nm and 100 nm cases), the XRD pattern shows a FCC structure for Ni with strong peaks at 44.3 ° corresponding to the reflection from Ni (111), 51.7 ° from Ni (200), and 76.2 ° from Ni (220), while a HCP structure for Ti with a strong peak at 38.6 ° corresponding to the reflection from Ti (002) and a weak peak at 35.6 ° from Ti (100). In the intermediate-layer cases (50 nm and 25 nm cases), the intensities of Ti (002) peak and Ni (200) become smaller and smaller, and Ni (220) peak disappears, while Ti (100) peak becomes stronger. In the thin-layer cases, Ti peaks become weaker with decreased layer thickness, and no longer distinguished with layer thickness less than 12 nm. Only Ni (111) peak maintains significant and the other two Ni peaks Ni (200) and Ni (220) are not visuable. In each case, there is a big intensity difference between Ni and Ti peaks, indicating that the Ni layer is more crystalline and textured than the Ti layer. By comparing the XRD patterns in Fig. 3.1, peak broadening can be obviously observed with decreasing layer thickness for both Ni and Ti peaks indicating finer grains with thinner layers. For multilayer film with thin individual layer, grain growth would be suppressed and small grains would dominate, which results in the broadening of the diffraction peaks.

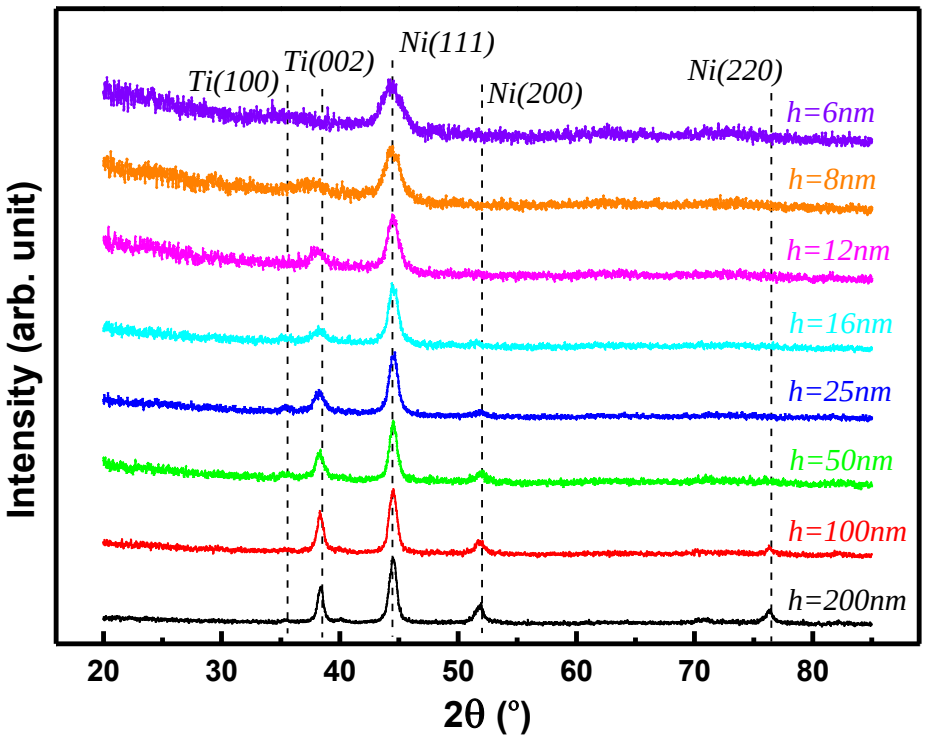

Figure 3.1: XRD spectra of as-deposited Ti/Ni multilayer thin films with layer thickness from 200 nm to 6 nm. Several different peaks are detected for both Ni and Ti materials, such as Ni (111), Ni (200), Ni (220), Ti (002), and Ti (100). Polycrystalline structures are indicated for both Ti and Ni layers.

For Ti/Ni multilayers, XRD spectra can be used to quantitatively estimate microstructure information. For Ti grains, the only significant peak Ti (002) is used to estimate the grain size by the following equation:

$$D = \frac{k\lambda}{\beta \cos(\theta)} \tag{3.1}$$

where D is the grain size, k is the Scherrer constant and here $k = 0.89$, λ is the x-ray wavelength and here $\lambda = 1.54$ Å, β is the peak width at half of the maximum intensity and θ is

the Bragg angle. Table 3.1 establishes the estimated Ti grain size for Ti/Ni multilayer thin films with layer thickness from 200 nm to 25 nm, decreased grain sizes from about 25 nm to 10 nm as the individual layer thickness decreases from 200 nm to 25 nm. For Ni grains, there are several Ni peaks and therefore the corresponding XRD peaks can be used to analyze both average grain size and microstrain by applying Williamson-Hall relationship [84] as following:

$$\beta\cos(\theta) = \frac{k\lambda}{D} + 4\varepsilon\sin(\theta) \tag{3.2}$$

where ε is the mean microstrain and other parameters are defined the same as in Equation (3.1). Take 50 nm case as an example, Table 3.2 shows the analysis results of both average grain size and mean microstrain. It should be pointed out that XRD measurement of microstrain and average grain size in Table 3.2 should be regarded as approximate estimation since only three Ni peaks can be used to fit these two parameters and not all three peaks are significant in the XRD spectra.

Table 3.1: Comparison of Ti grain size in as-deposited Ti/Ni multilayer thin films estimated by XRD spectra analysis and measured directly from cross-sectional SEM images

CASE	XRD analysis (nm)	SEM measurement (nm)
$h = 200$ nm	25.5	30.9 ± 12.3
$h = 100$ nm	21.3	21.9 ± 7.3
$h = 50$ nm	15.8	–
$h = 25$ nm	10.0	–

Table 3.2: XRD analysis of Ni peaks for as-deposited and 200 ℃ annealed Ti/Ni multilayer thin films with layer thickness 50 nm

CASE: $h = 50$ nm	Peak Width β (°)		Mean Microstrain ε (%)	Average Grain Size (nm)
	<111>	<220>		
RT	0.645	0.929	0.324 ± 0.064	25 ± 7
200 °C	0.626	0.887	0.278 ± 0.049	23 ± 4

3.3.2 Cross-section and Surface Morphologies

Fig. 3.2 shows the SEM images of the cross-section morphology for Ti/Ni multilayers with layer thickness from 200 nm to 25 nm. In all cases, layered structure can be clearly observed with bright one Ni layer and dark one Ti layer. Fractured cross-section morphologies display the columnar structure for Ni layers with a single grain along the thickness direction and the equiaxed structure for Ti layers, and more pronounced crystalline for Ni, which is consistent with the XRD results that the Ni peaks have much higher intensity than the Ti peaks. In addition, the SEM images of cross-section morphology can be used to directly measure the grain size. As shown in Table 3.1, the measured Ti grain size is in reasonable agreement with the estimation from XRD analysis.

For Ti/Ni multilayer with thin layer, SEM is not capable to capture the detailed cross-section morphology, and as a result TEM was performed to obtain microstructure information including cross-sectional TEM image and the corresponding diffraction pattern as shown in Fig. 3.3. Layered structure can be clearly observed with bright layer Ti and dark one Ni. More crystalline structure is displayed in Ni layers, consist with samples in thick- and intermediate-layer cases. Diffraction pattern indicates polycrystalline structure with a couple diffracted rings corresponding to the reflection from Ti (100), Ti (002), Ni (111) and Ni (200), which confirms the XRD spectra as shown in Fig. 3.1.

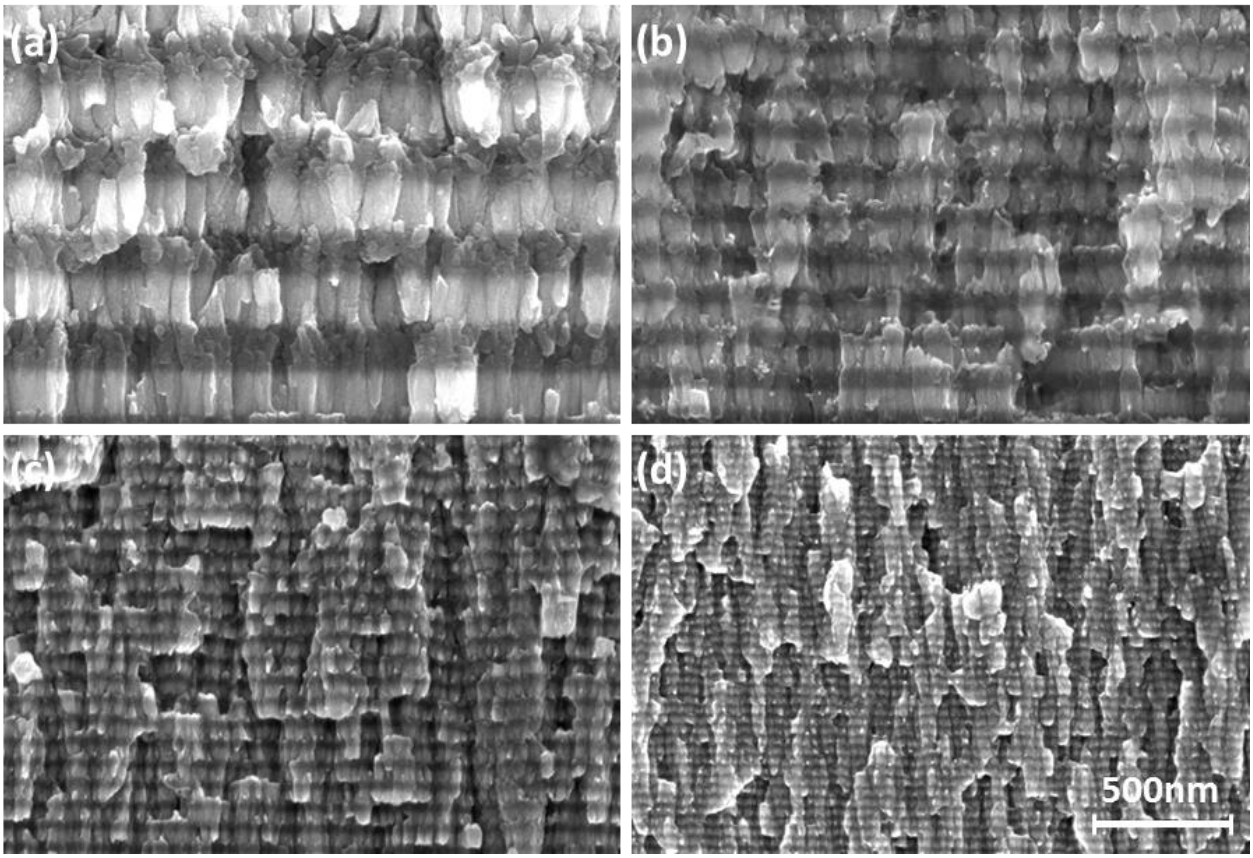

Figure 3.2: SEM images of cross-section morphology for as-deposited Ti/Ni multilayer films with individual layer thickness: (a) 200 nm; (b) 100 nm; (c) 50 nm; (d) 25 nm. Layered structure can be clearly observed in all cases, with dark layer Ti and bright one Ni. Ni grains show more crystallinity than Ti.

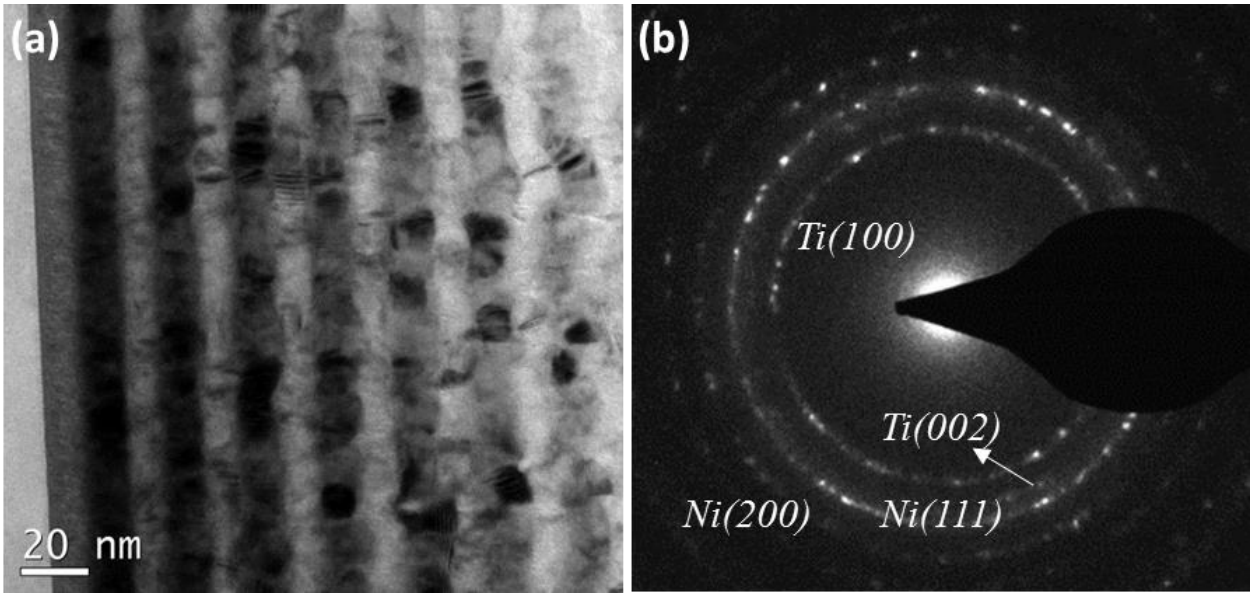

Figure 3.3: TEM results for as-deposited Ti/Ni multilayer with layer thickness 12 nm. (a) Bright field TEM image of cross-section: layered structure is clearly displayed with dark one Ni and bright one Ti. (b) The corresponding diffraction pattern: polycrystalline structures are confirmed for both Ti and Ni layers.

Fig. 3.4 shows the surface morphological SEM images for the Ti/Ni multilayer films with layer thickness from 200 nm to 6 nm. In the thick-layer case, the in-plane Ni particles are composed of a couple of grains while only one grain in the thin-layer case. The plan-view of the multilayers shows that the top Ni layers have in-plane particles about several tens of nanometers in diameter. Fig. 3.5 shows the relationship between the in-plane Ni particle size and layer thickness and it is obvious that the particle size decreases with decreasing individual layer thickness down to 50 nm, then reaches a plateau with grain size about 25 nm.

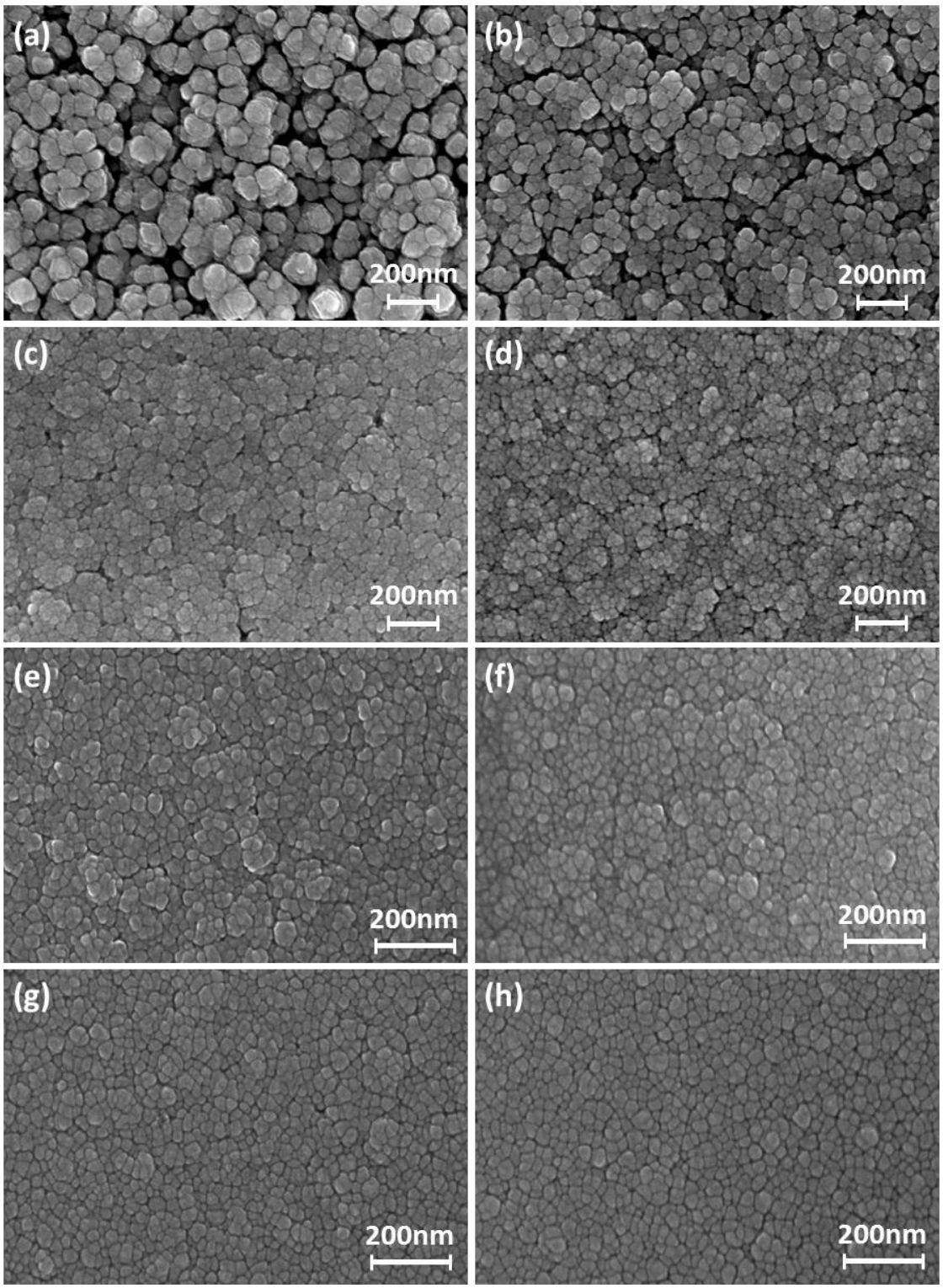

Figure 3.4: SEM images of surface morphology for as-deposited Ti/Ni multilayer thin films with different layer thickness (a) 200 nm; (b) 100 nm; (c) 50 nm; (d) 25 nm; (e) 16 nm; (f) 12 nm; (g) 8 nm; (h) 6 nm. Homogeneous grain structure is observed in all cases, and the surface grain/particle sizes could be directly measured.

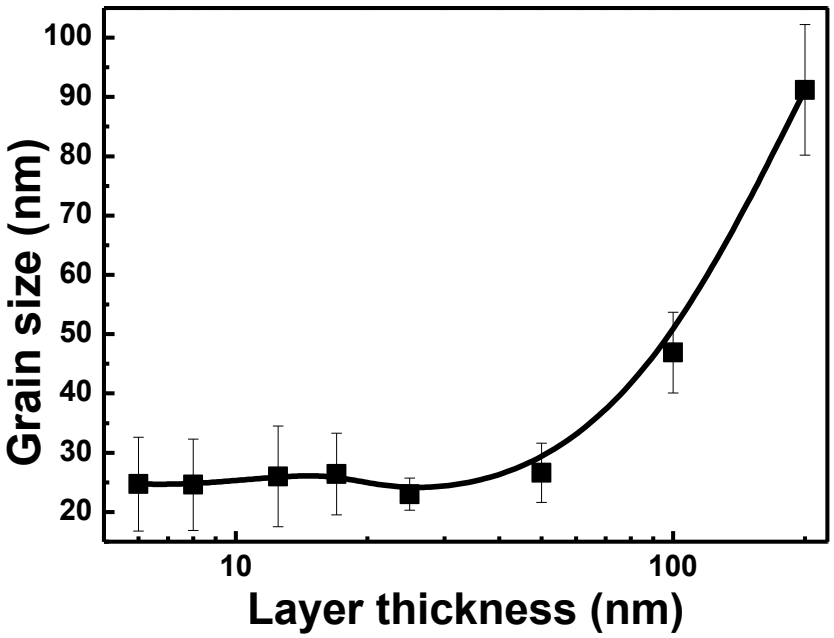

Figure 3.5: The relationship between in-plane Ni particle size and layer thickness of as-deposited Ti/Ni multilayer thin films. The grain/particle size decreases dramatically with the decrease of layer thickness down to 50 nm, and then a similar particle size level is maintained with further reduced layer thickness.

3.4 HARDNESS AND STRENGTHENING MECHANISM

3.4.1 Layer Thickness-dependent Strengthening Mechanism

Fig. 3.6 shows the hardness as a function of individual layer thickness for surface indentation of as-deposited Ti/Ni multilayers with layer thickness ranging from 200 nm to 6 nm. The hardness increases with decreasing individual layer thickness. For nanocrystalline multilayer thin films, both small gran size and small individual layer thickness can contribute to material strengthening due to dislocation-mediated deformation mechanisms. This is exactly what is observed here – the films with smaller layer thickness were shown to have finer grains and correspondingly higher hardness. To understand the exact mechanisms with respect to layer thickness, the hardness data is fitted with two different dislocation-mediated models as shown in Fig. 3.6. A Hall-Petch model based on dislocation pile-up along interface is used in the range with layer thickness (h) larger than 50 nm and a confined layer slip (CLS) model based on single dislocation bowing between interfaces is used in the range with layer thickness further down to 12 nm. The good fitting of dislocation associated models not only confirms the dislocation motion-dominated strengthening mechanism, but also validates our experiments. The detailed analysis is presented as following.

I. $h > 50$ **nm**

The hardness of as-deposited multilayers with $h > 50$ nm can be quantitatively analyzed by Hall-Petch model. The fitting is shown as in Fig. 3.7 by the following equation:

$$H = H_0 + Kh^{-1/2} \tag{3.3}$$

where H_0 is a constant, caused by lattice friction, here $H_0 = 1.67$ GPa, h the individual layer thickness, K the strengthening factor from layer thickness and $K = 20.8\ \text{GPa} \cdot \sqrt{\text{nm}}$ which can be used to estimate the maximum hardness via:

$$K_\tau = \sqrt{\frac{\tau^* \mu b}{\pi(1-\nu)}} \tag{3.4}$$

where τ^* is the interface barrier strength for slip transmission, μ is the shear modulus, b is the Burgers vector, and ν is the Poisson ratio. Substituting $K_\tau = \frac{K}{2.7 \times 3.1} = 2.49\ \text{GPa} \cdot \sqrt{\text{nm}}$ for a Hall-Petch fit to the shear strength data (2.7 is the Tabor hardness factor, and 3.1 is the Taylor factor), and $\mu = 76$ GPa, $b = 0.25$ nm, $\nu = 0.31$ for Ni, which is the softer material comparing to Ti, and plastic deformation tends to initiate from the softer phase, we obtain $\tau^* = 0.71$ GPa. Multiplied by the Tabor factor of 2.7 and Taylor factor of 3.1, this yields a maximum hardness of 5.9 GPa which is close to the experimental maximum hardness 6 GPa. Both good fitting of Hall-Petch model and precise prediction of maximum hardness indicate the dislocation pile-up along interface as dominated strengthening mechanism.

II. $h > 12$ **nm**

It is accepted that the modified CLS model based on single dislocation bowing between interfaces can be used to fit the hardness of multilayers with layer thickness down to a few tens of nanometer. The fitting of CLS model is shown in Fig. 3.6 (blue solid line), and the modified CLS stress $\sigma_{CLS} = H / 2.7$ is given as:

$$\sigma_{CLS} = \frac{M\mu b \sin\theta}{8\pi h}\left(\frac{4-\nu}{1-\nu}\right)\ln\left(\frac{\alpha h}{b\sin\theta}\right) - \frac{f}{h} + \frac{\mu b}{(1-\nu)L} \quad (3.5)$$

where M is the Taylor factor of 3.1, θ the angle between the slip plane and the interface, α the core cut-off parameter varying from 0 to 1, f the interface stress with a typical value 2-3 J/m^2, and L the spacing of the interface dislocation array. Other symbols have the same meaning as defined above. By taking $\alpha = 0.12$, $f = 3$, $\theta = 60^\circ$ and $L = 25$, the CLS model can fit the experimental data well with layer thickness ranged from 75 to 12 nm (blue solid line in Fig. 3.6). In the modified CLS model, $L = b/\varepsilon$, where ε is in-plane plastic strain with a typical value 1-2% for nanoscale metallic multilayers. Here $L = 25$ corresponds to a plastic strain around 1%. The good fitting of the modified CLS model with current experimental data indicates the single dislocation bowing between interfaces is the dominating strengthening mechanism in this layer thickness range.

III. $h < 12$ **nm**

While the peak strength of 6 GPa was reached at layer thickness 12 nm, a decreased hardness was observed with further decreasing layer thickness. Previous studies reported the maximum strength with layer thickness of a few nanometers and attributed interface crossing by dislocations is as operative softening mechanism with decreasing layer thickness since the interface resistance of single dislocation transmission decreases as the dislocation core approaches layer thickness. However, the layer thickness range of softening in the current study is beyond that for interface crossing mechanism. Both cross-section (Fig. 3.3) and surface (Fig. 3.4) morphology display

polycrystalline structure in the thin-layer cases, and thus grain boundary shear is considered as the probable dominating softening mechanism in this layer thickness range.

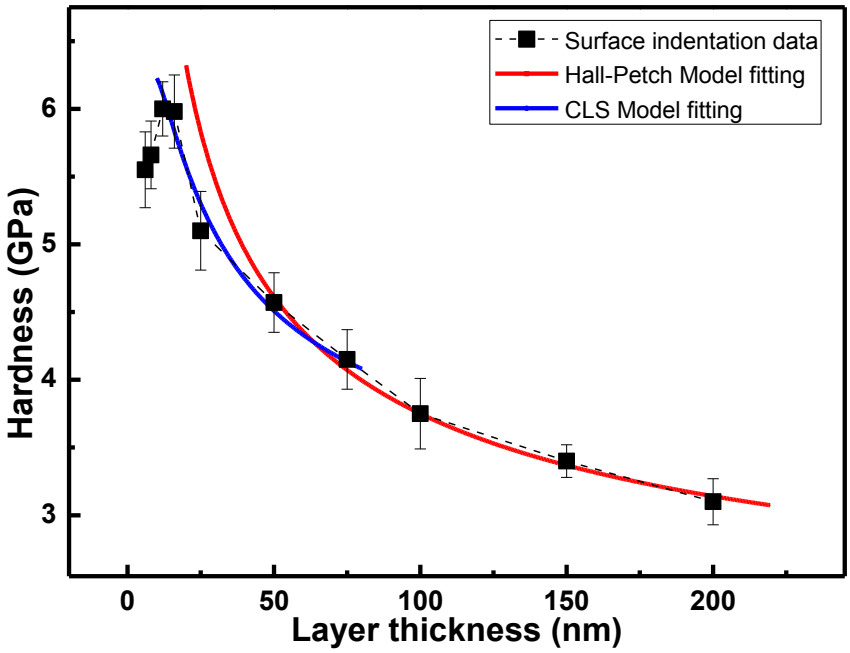

Figure 3.6: Hardness results of as-deposited Ti/Ni multilayers from surface indentation and the dislocation-based model fitting: Hall-Petch model for layer thickness ranging from 200 nm ~ 50 nm and CLS model for layer thickness ranging from 75 nm ~ 12 nm. The good fitting of both Hall-Petch model and CLS model not only indicate the dominant deformation behavior but only validate our experiments.

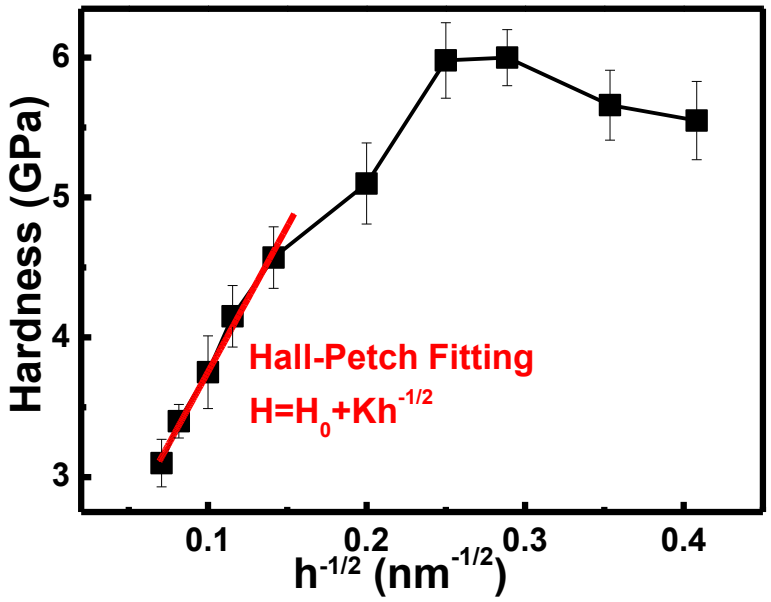

Figure 3.7: Hall-Petch fitting for as-deposited Ti/Ni multilayer thin films with layer thickness over 50 nm. The linear relationship between the hardness and the square root of layer thickness is shown.

3.4.2 Orientation-dependent Strengthening Mechanism

Fig. 3.8 shows the hardness as a function of individual layer thickness for both surface (unpolished) and cross-section (polished) indentations of as-deposited Ti/Ni multilayers with layer thickness from 200 nm to 25 nm. In both cases, the hardness increases with the decreasing individual layer thickness. For surface indentation, the detailed analysis was introduced in above section 3.4.1. For cross-section indentation, Fig. 3.9 shows the representative SEM and SPM images after indentation. Both images clearly show that most of the indents were controlled in the middle of the film. Compared to the surface indentation results, generally higher hardness was measured on the cross sections. The discrepancy between the surface and cross section indentation may be attributed to both plastic anisotropy and polishing process induced initial dislocation hardening.

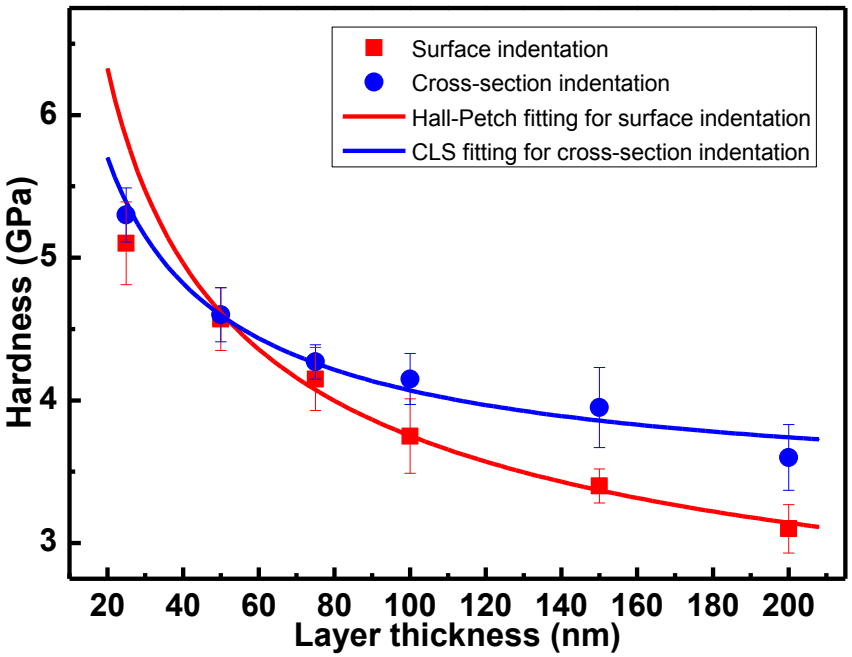

Figure 3.8: Hardness results from both surface indentation and cross-section indentation of as-deposited Ti/Ni multilayer thin films with layer thickness from 200 nm to 25 nm. The dislocation-based models are applied to fit the experimental results with Hall-Petch model for surface indentation and CLS model for cross-section indentation. Good fittings are shown in both models.

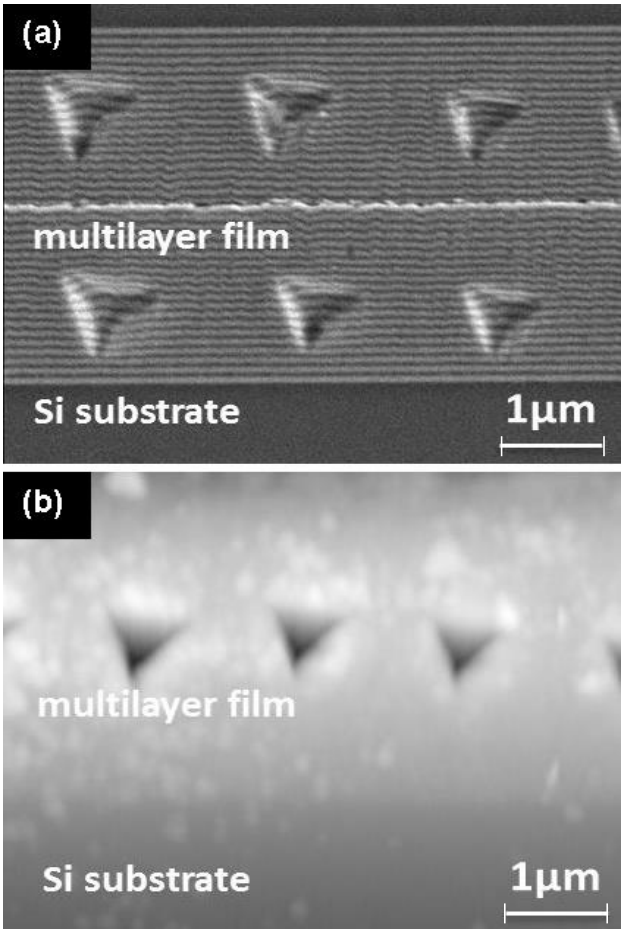

Figure 3.9: Representative (a) SEM and (b) SPM images of polished cross-sections of the multilayer thin films after indentation. In cross-section indentation, all the indents were performed in the middle of the film in order to avoid the Si substrate effect and boundary effect.

Three major plastic deformation modes in the tensile testing of nanotwinned metal along different orientations were introduced in Section 3.1, including a hard mode I, where both slip plane and slip direction are inclined to the twin interfaces, a hard mode II, where the slip plane is inclined to the twin interfaces but the slip direction is parallel to the interfaces, and a soft mode where both the slip plane and slip direction are parallel to the twin interfaces. In contrast to the coherent twin boundary planes, the Ti/Ni interfaces in this work are incoherent and only serve as barriers to

dislocation slip transmission. As a result, it does not render the soft deformation mode as seen in the nanotwinned Cu. In the as-deposited Ti/Ni multilayers, the XRD spectra (Fig. 3.1) indicate a preferred Ni (111) plane parallel to the interface. According to the Schmid's factor analysis for loading direction perpendicular and parallel to this plane, slip systems with both slip planes and slip directions inclined to the interface such as $(\bar{1}11)[101][011]$, $(11\bar{1})[101][110]$, and $(1\bar{1}1)[110][011]$ are more likely to be activated for surface indentation while slip systems with slip planes inclined and slip directions parallel to the interface such as $(11\bar{1})[01\bar{1}]$, $(\bar{1}11)[1\bar{1}0]$, and $(1\bar{1}1)[10\bar{1}]$ are more likely to be activated for cross section indentation. Therefore, the surface indentation is more likely to activate hard mode I, while cross section indentation is more likely to activate hard mode II, although the multilayer structure is much more complex due to the incoherent interfaces and grain boundaries, and nanoindentation process can generate much more complicated stress state than simple tensile loading. A schematic of activated slip systems by different loading orientations was shown in Fig. 3.10.

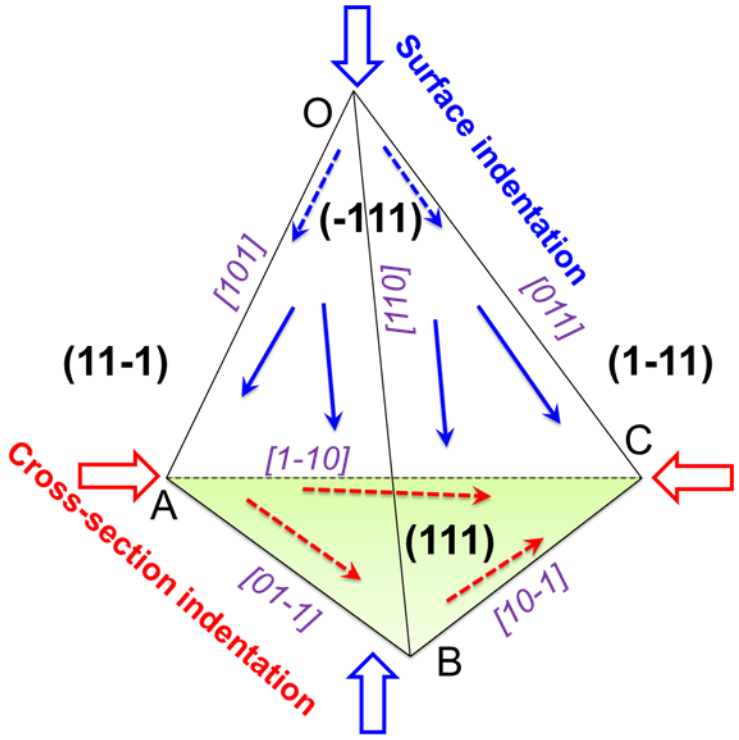

Figure 3.10: Schematic of activated slip systems by surface indentation and cross-section indentation. In surface indentation, slip systems with both slip planes and slip directions inclined to the interface are activated, while in cross-section indentation, slip systems with slip planes inclined to the interface, and slip direction parallel to the interface are activated.

In the above section 3.4.1, the Hall-Petch model was applied to fit the surface indentation results, and the good fitting indicates the dislocation pile-up as the dominant deformation mechanism involved in surface indentation, which is the aforementioned hard mode I, further confirming the Schmid's factor analysis. The Hall-Petch model can be also utilized to analyze the hardness results of cross-section indentation, and the slope K is obtained 12.96 GPa$\cdot\sqrt{\text{nm}}$. The consequent maximum hardness is estimated as 2.3 GPa, much lower than the experimental value, indicating other dominant deformation mechanism involved in cross-section indentation.

In the cross-section indentation, since the load is parallel to the multilayer interface, the deformation is more likely dominated by hard mode II. In this mode, dislocation can bow within layers and a recent CLS model has been adopted to analyze the hardness obtained as loading orientation parallel to interfaces. Together with the polishing effect, the hardness measured on the polished cross-section is fitted by the following equation:

$$H = H_0^{'} + \Delta H_P + 2.7 \times \eta \mu b \frac{\ln(\alpha h / b)}{h} \tag{3.6}$$

where $H_0^{'}$ is a material constant without interface confinement, caused by the lattice friction; ΔH_P is the initial dislocation hardening from the polishing process; and α is a material constant representing the dislocation core cutoff parameter, typically ranging from 0 to 1, and η is also a material constant. As shown in Fig. 3.8 (blue solid line), the CLS model can fit the experimental cross-section data very well by taking $\alpha = 0.16$, $\eta = 0.37$. And this fitting resulted in $H_0^{'} + \Delta H_P = 3.28\,\text{GPa}$. The close fitting of the CLS model to the cross-section indentation hardness data indicates that dislocation bowing within layers is the dominant deformation mechanism when the loading direction is parallel to the interfaces. Note that a similar equation was used for the CLS model in the nanotwinned Cu. In the Ti/Ni multilayer system with the incoherent interfaces, however, several factors such as interface stress and misfit dislocations can affect the dislocation motion during deformation. Further work such as atomistic simulation may be used to obtain more detailed information to refine the current CLS model. In addition, the polishing induced hardening may also be further estimated. By assuming $H_0^{'} = 1.67\,\text{GPa}$ (same values as H_0 in the surface indent), we obtain $\Delta H_P = 1.61$ GPa which yields a post-polishing dislocation density of $\rho_{0cs} \approx 4.1 \times 10^{14}\,\text{m}^{-2}$ based on the following relationship:

$$\Delta H_P / 2.7 = \gamma M \mu b \sqrt{\rho_0} \tag{3.7}$$

where ρ_0 is the initial dislocation density in the material; $\gamma = 0.5$ is the strengthening factor from ρ_0; M is the Taylor factor (~3.1). For comparison, polished surface samples were also indented and systematically higher hardness was obtained than the unpolished surface for all the layer thickness. Taking the difference between the polished and unpolished surface indentation hardness, the average polishing induced hardening $\overline{\Delta H_P}$ was calculated as 0.83 ± 0.07 GPa, which yields a dislocation density of $\rho_{0s} \approx 1.1 \times 10^{14}\,\mathrm{m}^{-2}$, about 75% lower than that of the cross-sectional case. Thus, polishing led to more hardening in the cross-section than the surface, probably due to the more direct cold working of the interface regions in the cross-section polishing.

3.5 CONCLUSION

In this work, layer thickness effect and loading orientation effect on the deformation behaviors and strengthening mechanisms of as-deposited Ti/Ni multilayer thin films were carried out with a wide range of layer thickness from 200 nm to 6 nm, and from both surface indentation and cross section indentation.

A strong size dependent material strength was observed in the as-deposited Ti/Ni multilayers. An increased hardness was obtained with the decreasing layer thickness until 12 nm, and the dominating strengthening mechanisms are dislocation mediated motions, such as dislocation pile-up along interfaces with layer thickness down to tens of nanometers and single dislocation bowing within layers with layer thickness from a few tens of nanometers to a few nanometers. The Hall-Petch model and modified CLS model can fit the experimental data very well, not only indicating the dislocation mediated motions as dominated deformation mechanisms but also validating our experiments. A decreased hardness was obtained with further decreasing layer thickness, and the dominating softening mechanism is probably grain boundary mediated motions.

In addition to the length scale effect, loading orientation plays an important role in deformation behaviors and strengthening mechanisms. Cross section indentation yielded higher hardness values for Ti/Ni multilayer thin films than surface indentation, and this discrepancy is attributed to different plastic deformation mechanisms along different loading orientations (dislocation pile up for surface indentation vs. confined layer slip for cross-section indentation) and polishing induced initial dislocation hardening.

Chapter 4. ANNEALED TI/NI MULTILAYER THIN FILMS – INTEGRATED ANNEALING TEMPERATURE – LAYER THICKNESS – LOADING ORIENTATION EFFECT

4.1 INTRODUCTION

Thermal annealing can have an important influence on microstructure evolution and deformation behaviors in metallic multilayer. Depending on the annealing temperature, various thermal activities could take place such as atomic diffusion, intermixing, recrystallization, grain growth, phase transformation and even intermetallic phase formation. The thermal stability of microstructure and multilayer strength at elevated temperatures could be significant if materials were exposure in thermal environment. However, few works have been done to understand the annealing temperature dependence of multilayer strength and the related mechanisms. A general decreased strength is achieved in different multilayer systems after a relatively high temperature annealing [85-87], and this softening phenomena have been attributed to the microstructure modification such as spheroidization of electrodeposited Cu/Ag multilayers annealed at 150 ℃ [85] and in-plane grain coarsening of Ni/Ru multilayers annealed at 450 ℃ [86]. In addition, significant morphological instabilities including complete disintegration of layered structure were observed in different multilayer systems [37, 88, 89], and such breakdown of periodicity can cause a dramatic strength drop [87].

In this work, a systematic study was carried out on the mechanical strength of Ti/Ni multilayer thin films of varying layer thickness and annealing temperatures. The layer thickness in this work is the same as in as-deposited section with the range of 200 nm to 6 nm, and the temperature range up to 500 ℃. The current work reveals the detailed dependency on annealing temperature - layer thickness - loading orientation of various deformation behaviors and strengthening mechanisms, such as dislocation mediated motions, grain boundary relaxation, solid solution hardening, precipitation hardening and alloying. The results not only shed light on the understanding of the deformation behavior and strengthening mechanisms in metallic multilayers, but also provide guidance to control and optimize this engineered material.

4.2 EXPERIMENTAL DETAILS

Ti/Ni multilayer thin films were used to study the integrated annealing temperature – layer thickness – loading orientation dependent material strength and strengthening mechanisms. The as-deposited films were fabricated by magnetron sputtering system as introduced in Chapter 3. A subset of the as-deposited Ti/Ni multilayer thin films were annealed under an Ar atmosphere for 2 hours with a variety of temperature from 100 ℃ to 500 ℃. The annealed samples in the thick- and intermediate-layer cases were then prepared for cross-section indentation, as introduced in Chapter 3. Comparison between cross-section and surface indentations help to demonstrate the mechanical anisotropy of the multilayers.

For mechanical strength, the aforementioned Ubi1 nanomechanical test instrument was still utilized to carry out both surface indentation and cross-section indentation on annealed samples with a cube corner indenter tip. A minimum of 20 indents was used to obtain the average hardness. For microstructure characterization, XRD was used to detect the crystal phases of Ti/Ni multilayers before and after annealing, and SEM was used to capture the microstructural evolution on the surface and cross-section after annealing. For the thin layer cases, TEM was performed to obtain the cross-section morphology for selected samples as SEM is resolution-limited at this length scale.

4.3 HARDNESS RESULT

Fig. 4.1 shows the hardness as a function of annealing temperature (T) for Ti/Ni multilayer thin films with layer thickness from 200 nm to 6 nm for both surface (S) and cross-section (CS) indentations. A coupled effect between annealing temperature and layer thickness was clearly observed. For the brevity of presentation, the results are divided into four temperature regions: room temperature (RT) for as-deposited films, low temperature (low-T) annealing for T<300 ℃, transitional temperature annealing for T=300 ℃ and high temperature (high-T) annealing for T>300 ℃. This division of temperature will be used throughout the manuscript. As shown in Fig. 4.1, for the thin layer cases, a monotonically increased hardness is observed with increasing annealing temperature. For the intermediate layer cases, an increased hardness is observed with increasing temperature up to 300 ℃, and then a decreased hardness under further high-T annealing. For the thick layer cases, there is no obvious hardness change under low-T annealing, but an increased hardness is observed for 300 ℃ and 400 ℃, and then a dramatic hardness decrease after 500 ℃ annealing. Overall, the hardness behavior under high-temperature annealing exhibits a very strong dependency on individual layer thickness. A complicated situation of hardness value is displayed here instead of a general decreasing trend mentioned by the aforementioned literatures [85-87].

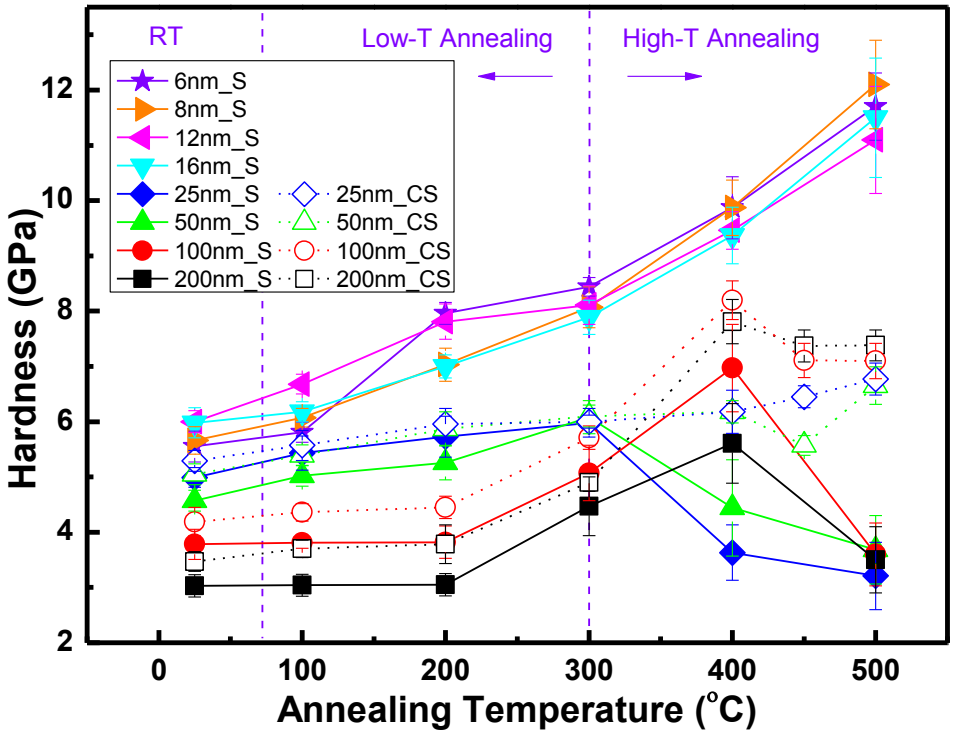

Figure 4.1: Surface (s) and cross-section (CS) indentation hardness of Ti/Ni multilayer thin films as a function of annealing temperature for different layer thickness.

In addition, an obvious orientation dependent hardness behavior is observed in the thick- and intermediate-layer cases after high-T annealing. In the thick-layer cases, although the same increasing-then-decreasing trend was observed in both cross-section indentation and surface indentation, the hardness drop at 500 ℃ is much less in the cross-section indentations. A large discrepancy of hardness behavior can be observed in intermediate-layer cases. Instead of the decreasing trend as in the surface indentation after high-T annealing, the hardness from the cross-section indentation continued the previous increasing trend from the low-T annealing.

In order to understand the various hardness behaviors associated with different layer thickness, annealing temperature and loading orientation, it is important to investigate the microstructure evolution of Ti/Ni multilayer thin films after thermal annealing.

4.4 MICROSTRUCTURE CHARACTERIZATION

4.4.1 XRD Spectra and Analysis

Thermal annealing induced microstructure modification of Ti/Ni multilayers can be revealed by XRD patterns. Fig. 4.2 and Fig. 4.3 shows the representative XRD spectrum for the thick-layer and thin-layer cases. During annealing, Ni and Ti atoms can start to diffuse along interface and grain boundary, and then phase transformation, recrystallization and grain growth, and even intermetallic formation occur under higher annealing temperature. All these thermal activities can be reflected by XRD spectra of Ti/Ni multilayers annealed at various temperatures.

For samples with layer thickness 100 nm, as shown in Fig.4.2, similar XRD spectra were obtained after low-T annealing. For low-T annealing case, the XRD spectra can be used to quantitatively estimate microstructure information as discussed in Chapter 3. Table 4.1 shows the comparison of estimated Ti grain size from as-deposited and 200 ℃ annealed Ti/Ni multilayers by using XRD spectra, and the difference is not detectable after low-T annealing. Table 3.2 shows the analysis results on as-deposited and annealed Ni grains in samples with layer thickness 50 nm. Slightly lower microstrain is obtained after 200 ℃ annealing associated with narrowed peaks detected. It should be pointed out again that XRD measurement of microstrain and average grain size in Table 3.2 should be regarded as approximate estimation due to the limitation of significant Ni peaks in the XRD spectra.

The intensity of Ti peak dramatically decreases after 300 ℃ annealing and no more Ti peak detected after high-T annealing. In addition, a couple new peaks corresponding to Ti-Ni

intermetallic phase were detected at 500 ℃. In spite of disappearance of the Ti peak and formation of the Ti-Ni intermetallic peak, Ni (111) stays as the strongest peak at all temperatures.

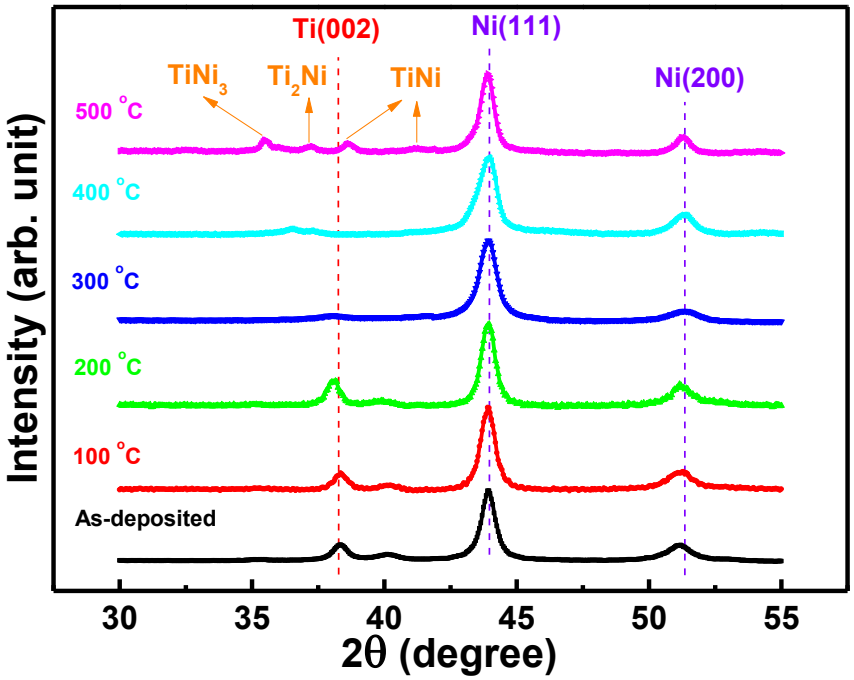

Figure 4.2: XRD spectra of as-deposited and annealed Ti/Ni multilayers with individual layer thicknesses 100 nm. No obvious change is observed after low-T annealing, while Ti-Ni intermetallic is detected after high-T annealing.

However, a totally different phenomenon is displayed in the samples with layer thickness 8 nm as shown in Fig. 4.3. Ni (111) is the only significant peak shown by the as-deposited sample and an obvious left shifting of this peak is observed after low-T annealing which may be caused by the diffusion of Ti atoms into Ni layer enlarging the Ni lattice. After high-T annealing, only Ti-Ni intermetallic peaks were detected. The disappearance of the Ni peak indicates possible

disintegration of layers and the formation of fully intermixed and completely alloyed structure. Both TEM images and quantitate XRD analysis in literature [38, 49, 50] provide evidences of complete mixed Ti-Ni structure instead of layered structure after high-temperature annealing. The broad peak located between Ni (111) and Ti-Ni intermetallic peak at 300 ℃ annealing is likely a combination of the intermetallic peak and shifted Ni (111) peak.

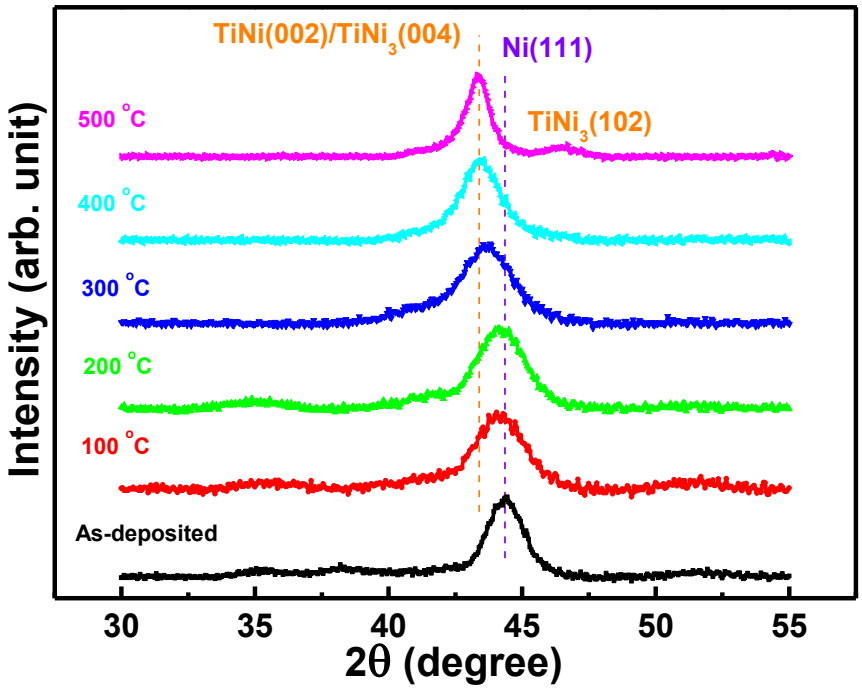

Figure 4.3: XRD spectra of as-deposited and annealed Ti/Ni multilayers with individual layer thicknesses 8 nm. No significant change is observed after low-T annealing, while only Ti-Ni intermetallic phase is detected after high-T annealing.

The different XRD spectra between the thick layer cases and thin layer cases indicate a strong layer thickness dependent microstructure evolution after thermal annealing. In the thin layer cases,

atomic diffusion may be activated upon low-T annealing which led to a large extent of diffusion and intermixing between the Ti and Ni layers, and the films evolve into complete Ti-Ni intermetallic phase with high-T annealing. In the thick layer cases, Ti-Ni alloys may only have been formed along the interfaces while the layered structure still being maintained.

All these thermal activities including initial diffusion and intermixing, phase transformation, intermetallic formation, multilayer disintegration can significantly influence the material strength. In order to validate the microstructure modification indicated from XRD patterns, SEM and TEM were performed and the corresponding images of surface and cross-section are presented below.

Table 4.1: The comparison of Ti grain size estimated by using XRD spectra and cross-section SEM images.

CASE	XRD		SEM	
	RT (nm)	200 °C (nm)	RT (nm)	200 °C (nm)
$h = 200$ nm	25.5	24.8	30.9 ± 12.3	28.4 ± 6.0
$h = 100$ nm	21.3	20.5	21.9 ± 7.3	24.4 ± 5.5
$h = 50$ nm	15.8	18.2	–	–
$h = 25$ nm	10.0	10.3	–	–

4.4.2 Cross-section and Surface Morphology

Cross-sectional SEM and TEM images provide direct evidence and confirmation of the aforementioned postulation of the layer thickness dependent microstructural evolution after thermal annealing. As shown in Fig. 3.2 and Fig. 3.3, the layered structure can be clearly observed for as-deposited Ti/Ni multilayers with different layer thicknesses. The as-deposited film shows the columnar structure in the Ni layers with a single grain along the thickness direction and the equiaxed structure in the Ti layers. Fig. 4.4 shows the evolution of cross-sectional morphology after thermal annealing for Ti/Ni multilayer with layer thickness 200 nm. There is almost no microstructure modification after low-T annealing (Fig. 4.4(b)), and slightly in-plane grain growth after 300 ℃ (Fig. 4.4(c)) and 400 ℃ annealing (Fig. 4.4(d)), and obvious diffusion observed along interfaces and grain boundaries after 500 ℃ annealing (Fig. 4.4(e)). After such high temperature annealing, the interface and grain boundary become less distinct, recrystallized Ni grains and voids can be observed. However, the layered structure is still maintained even after 550 ℃ annealing (Fig. 4.4(f)). In contrast, for layer thickness 25 nm case, the layered structure was already disintegrated after 400 ℃ annealing as shown in Fig. 4.5, indicating an inferior thermal stability in the thin layer cases.

In literature, quite a few studies dealt with the thermal stability of Ti/Ni multilayer thin films with thin individual layer, and reported: (1) after high-T annealing, a fully intermixed and completely alloyed structure to replace the layered structure, and (2) at 300 ℃ annealing, solid state reaction leading to amorphization due to a large extent of atomic diffusion. The XRD results in Fig. 4.3 only confirmed the complete alloying process after high-T annealing. However, after 300 ℃

annealing, instead of an amorphous structure, our study showed that a mixed structure including Ti, Ni, Ti-Ni amorphous and Ti-Ni intermetallic is more possible.

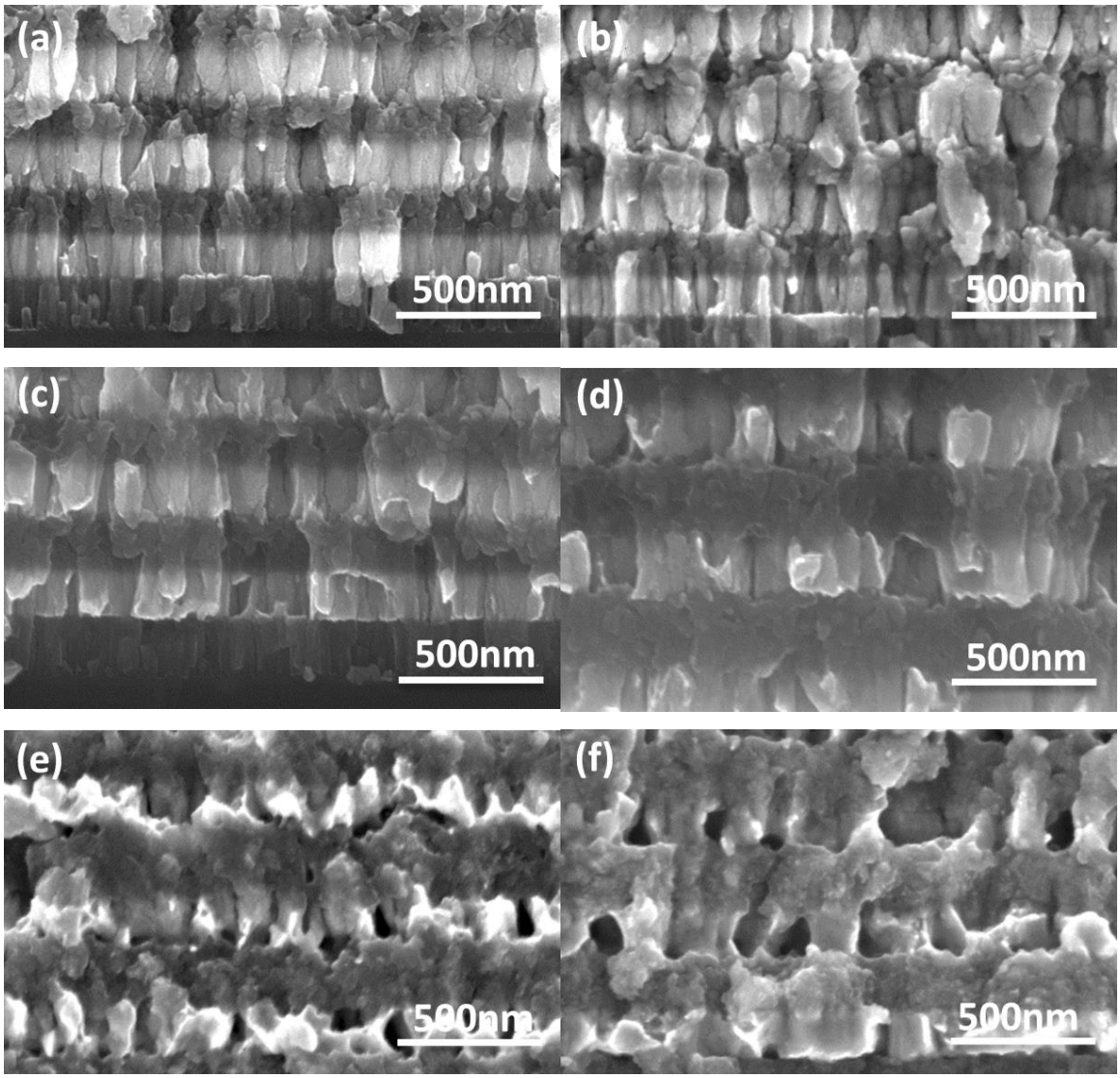

Figure 4.4: SEM images of cross-section morphology of Ti/Ni multilayers with layer thickness 200 nm in different cases: (a) as-deposited (b) 200 ℃ annealed (c) 300 ℃ annealed (d) 400 ℃ (e) 500 ℃ annealed (f) 550 ℃ annealed. No obvious different is observed after annealing up to 300 ℃, slight grain growth after annealing at 400 ℃, and obvious diffusion after annealing at higher temperature. Layered structure is still maintained in all cases.

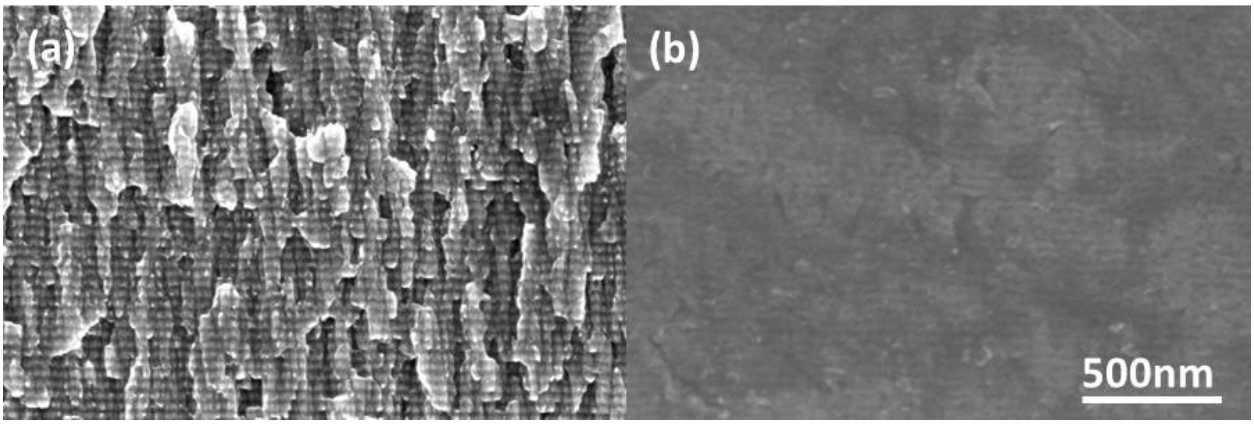

Figure 4.5: SEM images of cross-section morphology of Ti/Ni multilayers with layer thickness 25 nm in (a) as-deposited and (b) 400 ℃ annealed cases. Partially layered structure is observed after high-T annealing.

Now one aspect still not clear is that whether there is also a large extent of atomic diffusion during the low-T annealed thin film cases. To answer this question, TEM was performed to obtain important microstructure information. Fig. 4.6 shows the cross-section morphology and diffraction patterns for an as-deposited sample with layer thickness 12 nm and a 200 ℃ annealed sample with layer thickness 16 nm. Distinct interface can be observed in the bright field high resolution TEM images. In addition, the diffraction patterns confirm the polycrystalline nature and the phases of the Ti and Ni layers shown by the XRD, but do not show any amorphous structure induced broadening of the diffraction rings. The fact that the crystal lattices in each layer are clearly observed to extend all the way to the interface in the high resolution TEM image shown in Fig. 4.6(c) indicates only moderate diffusion occurred during the low-T annealing.

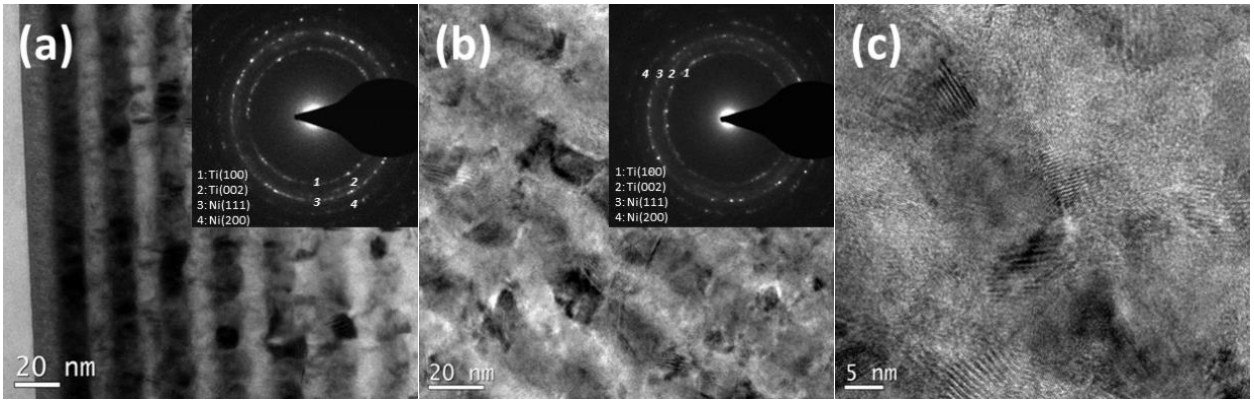

Figure 4.6: TEM images of Ti/Ni multilayer thin films in thin-layer cases. (a) As-deposited sample with layer thickness 12 nm. (b) 200 ℃ annealed sample with layer thickness 16 nm. (c) High-resolution TEM image for (b). The insert figures in (a) and (b) are corresponding diffraction patterns.

In addition, surface morphology can provide complementary information about layer thickness and annealing temperature dependent microstructure evolution. The representative surface SEM images are shown in Fig. 4.7 with one example from each of the thin, intermediate and thick layer cases. Information from the complete set of SEM images showed that for the as-deposited films, surface grain size decreases with decreasing layer thickness till layer thickness 25 nm, below which the surface grain size remains relatively constant around 25 nm. After thermal annealing, the surface morphology (e.g., grain size and shape) changes differently with different layer thickness. In layer thickness 200 nm case, no significant change is observed for annealing up to 300 ℃, only slight grain growth after 400 ℃ and recrystallized grains after 500 ℃, and all of these changes are consist with those indicated from the cross-section SEM (Fig. 4.4). In layer thickness 50 nm case, the surface shows no measurable microstructure change up to 300 ℃, but recrystallization upon 400 ℃ annealing and fully recrystallized grain structure after 500 ℃ annealing. In layer thickness

8 nm case, the morphology was almost identical after 200 ℃ to that of the as-deposited, consistent with the TEM observation, confirming insignificant atomic diffusion during low-T annealing. At 300 ℃ annealing, much sharper grain structure covers the whole surface (indicated by the bright dots), probably due to diffusion-induced grain sharpening and Ti-Ni intermetallic phase. After high-T annealing, a very different surface morphology corresponding to the Ti-Ni alloys is formed.

Combining the information from XRD, SEM and TEM, the microstructure evolution associated with different layer thickness and annealing temperature may be summarized as following. After low-T annealing, no significant microstructure change is observed in the thick and intermediate layer cases, and slight atomic diffusion occurs in the thin layer cases. After 300 ℃ annealing, increased thermal diffusion and even intermetallic formation happened in the thin layer cases, while still no obvious change in other cases. After high-T annealing, the phenomena is quite different for different cases. In the thick layer cases, only slight grain growth happened after 400 ℃ and recrystallization happened after 500 ℃ with significant voiding due to diffusion. In the intermediate layer case, however, significant recrystallization started after 400 ℃ which continued to 500 ℃, and only partially layered structure is maintained. In addition to grain growth and recrystallization in the thick and intermediate layer cases, there is also Ti-Ni intermetallic formation along the interfaces. In the thin layer case, the initially multilayered structure evolved into a completely alloyed structure. These detailed microstructure evolution and analysis will be utilized to explain the observed layer thickness, annealing temperature and loading orientation dependent hardness and strengthening mechanisms in next section.

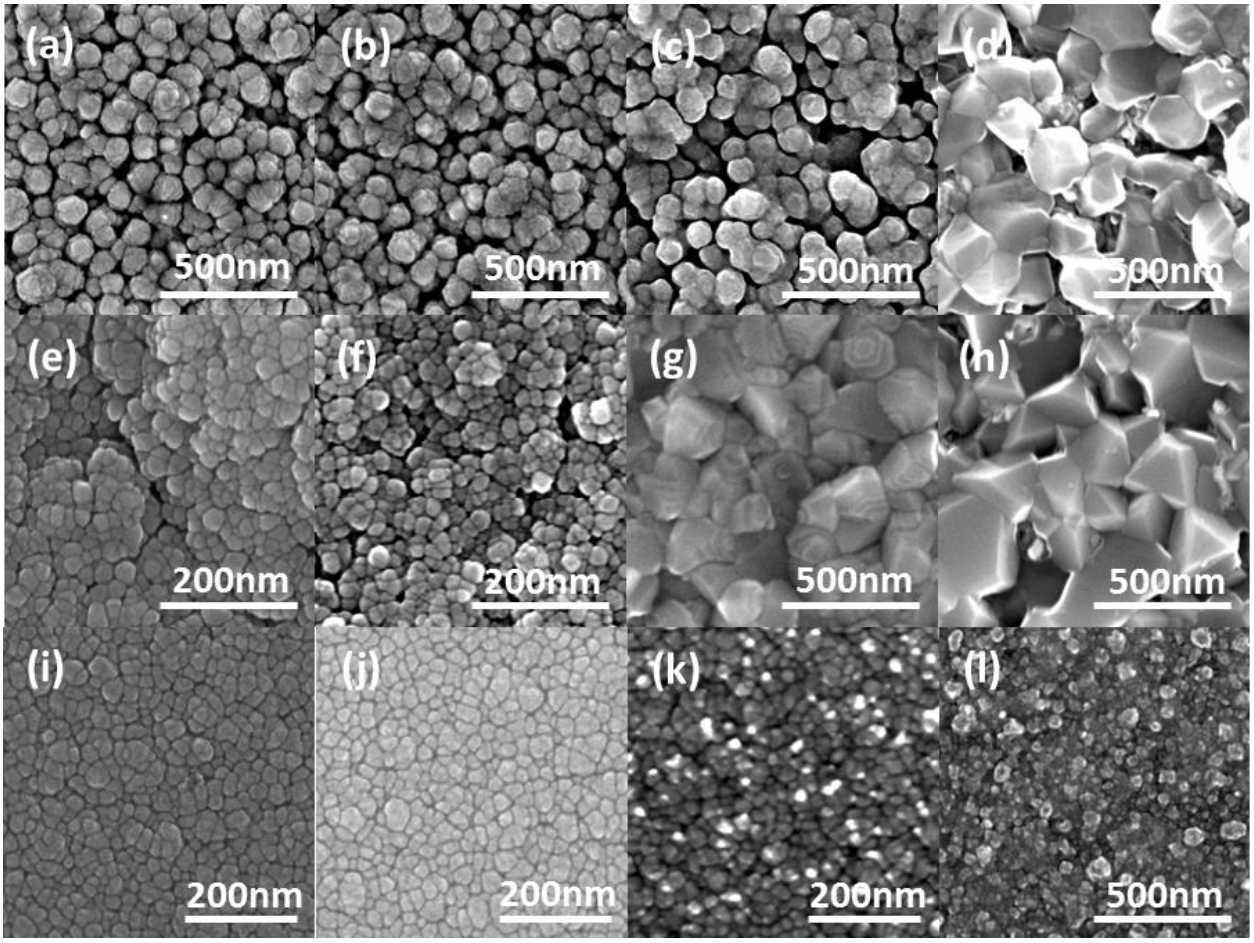

Figure 4.7: SEM images of surface morphology for Ti/Ni multilayer thin films in thick-layer case 200 nm (a) as-deposited (b) 300 ℃ annealed (c) 400 ℃ annealed (d) 500 ℃ annealed, in intermediate-layer case 50nm (e) as-deposited (f) 300 ℃ annealed (g) 400 ℃ annealed (h) 500 ℃ annealed, and in thin-layer case 8 nm (i) as-deposited (j) 200 ℃ annealed (k) 300 ℃ annealed (l) 400 ℃ annealed.

4.5 STRENGTHENING MECHANISM

4.5.1 Strengthening Mechanisms in Low-T Annealed Multilayer Thin Films

To demonstrate the effect of annealing on the hardness of the Ti/Ni multilayer thin films, Fig. 4.8 shows the hardness as a function of individual layer thickness for as-deposited and low-T annealed Ti/Ni multilayer thin films by surface indentation. Clearly, the low-T annealing led to a significant strengthening effect on the multilayer thin films and more pronounced strengthening is shown on the films with smaller individual layer thickness. In addition, higher annealing temperature is shown to lead to a more significant hardness. Since the annealing temperature here is much lower than the recrystallization temperature (around 400 ℃), there is little microstructure change after low-T annealing. This is confirmed by the previous SEM: no noticeable grain size change. On the other hand, the low-T annealing induced peak narrowing shown in the XRD spectra could be due to either microstrain reduction or grain size increase. However, it is well known that grain growth can soften material strength. Furthermore, there is neither any new Ti/Ni nor Ti-Ni intermetallic peak from the XRD spectra. Literature also showed that Ti-Ni intermetallic would only start to form after annealing at 400 ℃ for Ti/Ni multilayer thin films. Therefore, neither small grain induced Hall-Petch strengthening nor new Ti-Ni phase involved precipitation hardening are responsible for the increased hardness with increasing temperature. As a result, the reduced microstrain as indicated in Table 3.2 should be the main reason for the observed peak narrowing and the hardness strengthening.

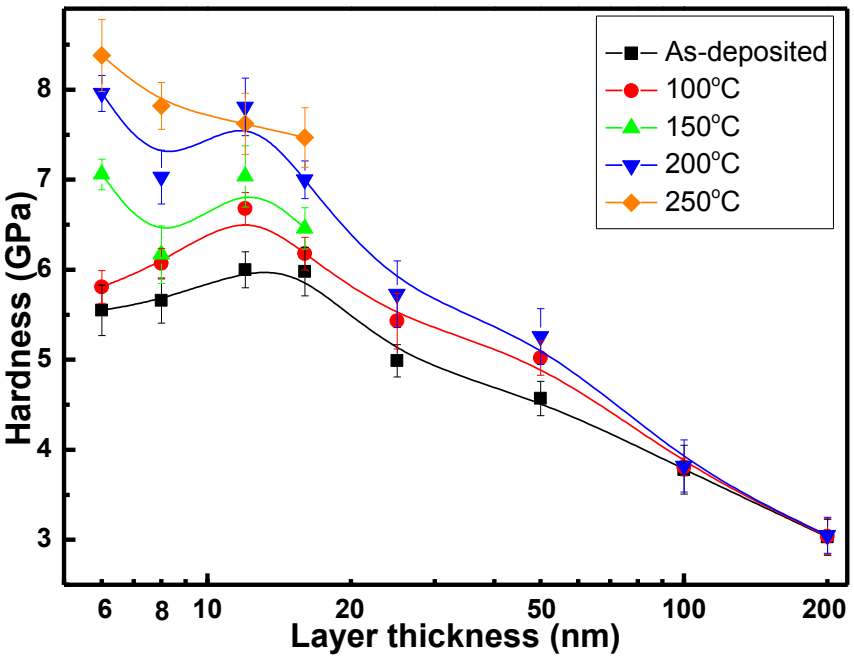

Figure 4.8: Hardness evolution as a function of layer thickness for both as-deposited and low-T annealed Ti/Ni multilayer thin films. More strengthening is observed in thin layer cases annealed at higher temperature.

The strength increase after low-T annealing has been previously reported by others on bulk nanocrystalline material and grain boundary relaxation is considered as the hardening mechanism. When the grain size is below 100 nm, grain boundaries occupy a significant volume fraction of the material, and the corresponding grain boundary mediated processes evolve into plastic deformation, such as grain boundary sliding. These deformation mechanisms tend to soften the material. However, these softening effects may be significantly suppressed by low-T annealing. During the annealing process, the number of grain boundary atoms decreases and the grain boundaries relax into a more equilibrated and ordered state, which provide a higher barrier for dislocation emission or grain boundary sliding, and thus force the material to deform by dislocation

glide. The annealing induced grain boundary relaxation has been studied experimentally and computationally on bulk nanocrystalline materials, and all of these studies suggest that not only size scale but also grain boundary state can dramatically affect the material strength and deformation.

The same mechanisms seem to be activated here in the Ti/Ni multilayer thin film systems – annealing led to the grain boundary relaxation and higher resistance of the multilayers to yielding, and thus increased hardness. In previous section, a Williamson-Hall fitting of the XRD peak profiles revealed the reduction of the microstrain in low-T annealing Ti/Ni multilayer thin films, further indicating that the grain boundary relaxation is the strengthening mechanism in this temperature range. The layer thickness dependent thermal strengthening shown here also further indicates that systems with large layer thickness may require higher annealing temperature to activate the grain boundary relaxation process due to the associated large grain size. In contrary, for films with smaller layer thickness, smaller grains dominate and the grain boundaries can be easily relaxed after annealing at low-T. Moreover, the kinetic analysis in Rupert's work showed that higher annealing temperature may activate more relaxation processes and hence results in more strengthening. This is confirmed by the indentation hardness results shown in Fig. 4.8, which shows higher hardness after annealing at higher temperature, especially when the layer thickness is small, e.g., the 25 nm case displays about 16% higher hardness after annealing at 200 ℃.

When layer thickness is below 16 nm, as shown in Fig. 4.8, a softening trend with decreasing layer thickness is observed for as-deposited samples due to possible grain boundary mediated motions, as discussed in Chapter 3. After low-T annealing, however, the grain boundary mediated motions

may be suppressed due to the more ordered grain boundary structure and the materials deform by dislocation glide, and as a result, a strengthening trend with decreasing layer thickness is observed for low-T annealing samples. In addition, slight diffusion was indicated from the microstructure characterization and the hardness enhancement in thin layer cases could be partially due to solid solution strengthening from diffused Ti and Ni atoms.

Fig. 4.9 shows the side-by-side bar graph comparison between surface indentation and cross-section indentation for the Ti/Ni multilayer thin films in thick and intermediate layer cases with the annealing induced hardening shown as increments from the previous temperature. Clearly more annealing induced strengthening is observed for the cross-sections. Since cross-section indentation covers two times more interfaces than that in surface indentation, this indicates that in addition to the grain boundary relaxation, low-temperature annealing might have also induced more stable interfaces. For the thick layer case, little thermal strengthening is observed in the surface indentation, while obvious strengthening for the cross-section indentation. This may be attributed to the small cross-section grain width as shown in Fig.4.2 since grain boundary relaxation can be more easily activated with the smaller grains.

(a)

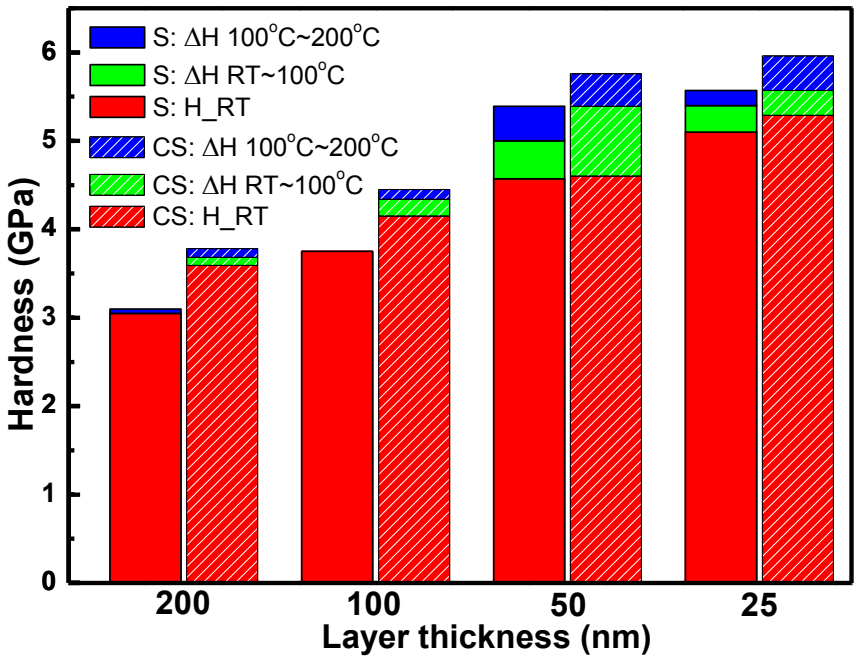

Figure 4.9: The comparison of hardening from surface and cross-section indentations after low-T annealing. More hardening is observed in cross-section indentation.

4.5.2 Strengthening Mechanisms in 300 ℃ Annealed Multilayer Thin Films

Fig. 4.10 shows the hardness evolution with different layer thickness for 200 ℃ and 300 ℃ annealed samples. All layers showed an increased hardness from 200 ℃ to 300 ℃, but a much larger amount of strengthening in the thicker layer. Grain boundary relaxation may continue to be the operative mechanism in the thick- and intermediate-layer cases since almost no obvious microstructure modification is detected for these cases after 300 ℃ annealing. The slightly higher temperature appears to have provided sufficient energy to activate the grain boundary relaxation process in thick layer cases, leading to an initial strengthening. However, the grain boundary

relaxation strengthening in the intermediate layer cases may have approached the saturation limit after low-T annealing, thus only moderate strengthening is observed after 300 ℃ annealing. In the thin layer cases, however, since a large extent of diffusion and Ti-Ni intermetallic formation were detected, solid solution strengthening and precipitation strengthening of intermetallic should be the dominating mechanisms together with continued grain boundary relaxation.

In addition, for thick and intermediate layer cases, the similar strengthening behavior is also observed in cross-section indentation, with more strengthening in thick layer cases.

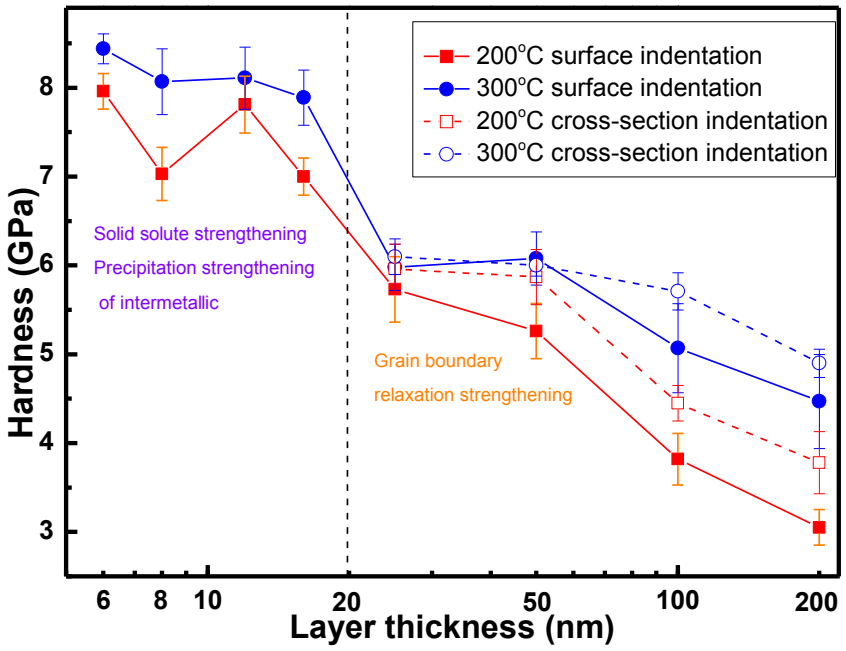

Figure 4.10: Hardness evolution with varying layer thickness for 200 ℃ and 300 ℃ annealed Ti/Ni multilayer thin films. More strengthening is observed in thick layer cases.

4.5.3 Strengthening/softening Mechanisms in High-T Annealed Multilayer Thin Films

Based on the microstructure analysis in previous sections, the strong layer thickness dependent hardness behavior observed after high-T annealing (400 ℃ ~ 500 ℃) may be attributed to combined results from grain boundary relaxation, solid solution strengthening, precipitation strengthening, intermetallic strengthening, and grain growth softening.

The results from surface indentation are first analyzed here. In the thick layer cases, grain boundary relaxation could be the dominating mechanism for the continued strengthening after 400 ℃ annealing while grain growth is responsible for the dramatic softening after 500 ℃. Note that slight grain growth was observed after 400 ℃ annealing. In the intermediate layer cases, continuously decreased hardness with increasing annealing temperature is also due to the grain growth, while the opposite trend in the thin layer cases is a result of the fully intermixed and completely alloyed structure.

In addition, the strong orientation dependent hardness behavior observed in the thick and intermediate layer cases can be attributed to high-T annealing induced crystallographic texture and precipitations. After high-T annealing, the recrystallized and grown surface grains have a size up to hundreds of nanometers, while the grain width is only a few tens of nanometers from the cross section. In addition, the Ti-Ni intermetallics formed along the interfaces and the fact that cross-section indentation covers two times more interfaces compared to the surface indentation also contributes to the observed mechanical anisotropy after high-T annealing.

4.5.4 Integrated Annealing Temperature – Layer Thickness – Loading Orientation Dependent Strengthening Mechanism

The systematic study on integrated annealing temperature - layer thickness - loading orientation effect on the hardness of Ti/Ni multilayer thin films provides new insights on the strengthening/softening mechanisms of nanometric metallic multilayer thin films. A qualitative strengthening mechanism map is proposed in Fig. 4.11 based on the discussions in sections 4.5.1-4.5.2, integrating the effect from annealing temperature, layer thickness, and the loading orientation. Detailed discussions are presented as following.

For as-deposited multilayer thin films, dislocation-mediated motions are the dominating strengthening mechanisms with decreasing layer thickness, e.g. dislocation pile-up along interface with layer thickness down to tens of nanometers and single dislocation bowing between interfaces with layer thickness from a few tens of nanometers to a few nanometers. However, the latter motion could be the dominating strengthening mechanism with layer thickness up to hundreds of nanometers when the loading orientation switches from perpendicular to parallel to the interfaces. With layer thickness of a few nanometers, the softening with further reduced layer thickness can be attributed to grain boundary mediated motions such as grain boundary sliding and rotation.

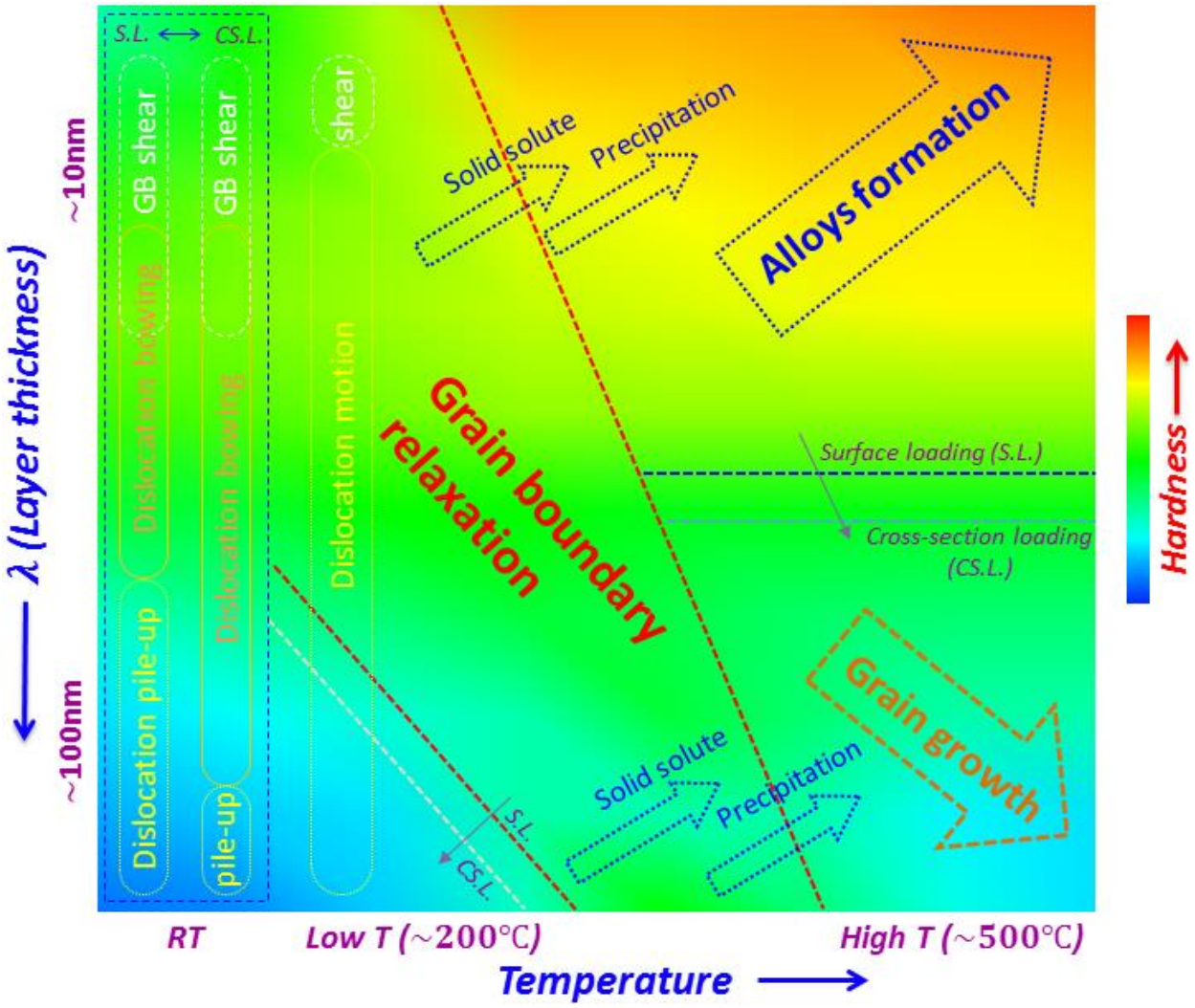

Figure 4.11: Schematic of strengthening/softening mechanism map of integrated annealing temperature, layer thickness, and loading orientation for Ti/Ni multilayer thin films.

However, the abovementioned grain boundary mediated processes can be suppressed by annealing activated grain boundary relaxation. Low-T annealing can trigger this grain boundary relaxation mechanism more easily in thin layer cases due to the small grain size and large volume of grain boundary atoms. More strengthening is achieved in cross-section loading due to smaller grain width compared to the much larger particle size on the surface.

Continued annealing (e.g. 300 ℃) could provide sufficient energy to activate grain boundary relaxation in the thick layer cases, leading to an initial strengthening. In the intermediate layer cases, further strengthening is achieved, but moderate since the low-T annealing induced strengthening may have approached the saturation limit. In the thin layer cases, however, in addition to grain boundary relaxation, strengthening is also resulted from solid solution of diffused atoms and precipitation of intermetallics.

Under high-T annealing, grain boundary relaxation induced strengthening in the thick layer cases will eventually be overtaken by recrystallization and grain growth induced softening. In the intermediate layer thickness, high-T induced grain growth softening appears at a lower temperature (e.g. 400 ℃ vs. 500 ℃) compared to the thick layer cases. However, slight strengthening may continue in the cross section loading due to high-T induced anisotropic texture and intermetallic precipitates. In the thin layer cases, a fully intermixed and completely alloyed structure results in a continuously increased hardness with increasing annealing temperature.

Therefore, from as-deposited to annealed multilayer thin films, grain boundary relaxation is the initial strengthening mechanism with higher activation temperature required for thicker layers. The strengthening mechanism transitions from grain boundary relaxation to solid solution and precipitation strengthening with the increase of annealing temperature, due to high thermal energy induced atomic diffusion and intermetallic formation. After high-T annealing, the hardness evolution is determined by two competing mechanisms – strengthening due to alloy formation and softening due to recrystallization and grain growth. For thin layers, the fully intermixed and

completely alloyed structure lead to continuously increased hardness. For thick layers, the layered structure is till maintained due to the large layer thickness despite of the extensive diffusion along the layer interfaces. Recrystallization and full grain growth leads to softening. Therefore, the layer thickness controls the mechanism switch between alloying strengthening and grain growth softening in the high temperature regime.

4.6 CONCLUSION

In the current work, a systematical study on integrated annealing temperature – layer thickness – loading orientation effect on the strengthening mechanisms of Ti/Ni multilayer thin films was carried out with a wide range of layer thickness, 200 nm – 6 nm, and annealing temperature from RT to 500 ℃. A monotonically increased hardness is observed with the whole range of annealing temperatures for the thin layer cases. For the intermediate layer cases, an increasing trend was observed from low-T to a transition temperature of 300 ℃, and then a decreased hardness was observed with high-T annealing. For the thick layer cases, the hardness started to show an increase after 300 ℃ annealing which continues into the high-T (400 ℃) annealing, and then a dramatic drop after further increased temperature (500 ℃).

These hardness behaviors can be explained through microstructure characterization and analysis. Under low-T annealing, no significant microstructure change in the thick and intermediate layer cases, and slight atomic diffusion occurred in the thin layer cases. After 300 ℃ annealing, increased thermal diffusion and even intermetallic formation happened in the thin layer cases, while still no obvious change in other cases. After high-T annealing, the phenomena is quite different for different cases. In the thick layer cases, only slight grain growth happened after 400 ℃ and recrystallization happened after 500 ℃ with significant voiding due to diffusion. In the intermediate layer cases, however, significant recrystallization started after 400 ℃ which continued to 500 ℃, and only partially layered structure is maintained. In addition to grain growth and recrystallization in the thick and intermediate layer cases, there is also Ti-Ni intermetallic formation along the interfaces. In the thin layer cases, the initially multilayered structure evolved into a completely alloyed structure.

Based on the detailed mechanical and microstructural analysis, a qualitative strengthening mechanism map integrating effects from annealing temperature, layer thickness, and loading orientation is proposed. Under room temperature, dislocation mediated activities, including dislocation pile-up along layer interfaces for layer thickness over 50 nm and single dislocation bowing between interfaces for layer thickness over 12 nm, are responsible for the observed layer thickness strengthening. Based on the literature report, the observed softening behavior for multilayer thin films with even smaller layer thickness may be attributed to grain boundary mediated motions. After low-T annealing, grain boundary relaxation is considered to be the dominating strengthening mechanism with increasing activation temperature required for thicker layers. With increasing annealing temperature, the strengthening mechanism transitions from grain boundary relaxation to two competing mechanisms – solid solution and intermetallic precipitation hardening, and recrystallization and grain growth induced softening. The exact trend for the hardness evolution is determined by the layer thickness – strengthening trend dominates the thin layer behavior due to the small layer thickness and large number of interfaces which facilitate more solid solution formation and intermetallic precipitation as well as complete alloying, while softening trend dominates the thick layer behavior due to the large extent of recrystallization and grain growth within the layers. For intermediate layer thickness, the trend of the hardness evolution switches from grain growth softening to intermetallic precipitation strengthening by changing the loading orientation from perpendicular to parallel to the interfaces.

The results in this study highlight the integrated effects of annealing temperature, layer thickness, and loading orientation on the mechanical strength and thermal stability of metallic multilayer

systems. The improved understanding of the deformation and strengthening mechanisms may provide meaningful guidelines on the control and optimization of this important class of future engineered materials.

Chapter 5. DEPOSITION TEMPERATURE INDUCED TEXTURE AND STRENGTHENING OF TI/NI MULTILAYER THIN FILMS

5.1 INTRODUCTION

Deposition temperature/substrate temperature plays an important role during thin film deposition in order to achieve desired microstructure for optimum functional properties [90]. For example, with close control of the deposition conditions, a homogeneous ordered Nb_3Sn thin film exhibits superconducting property in the design of a superconducting power transmission line (SPTL) [91], and a highly textured Al-doped ZnO thin film deposited with substrate temperature 150 ℃ displays low resistivity and high visible optical transmittance [92], which can be applied as transparent electrodes for solar cells, flat panel displays, and thermal coatings. From the viewpoint of thermodynamics, polycrystalline thin film prefers a certain crystallographic texture with orientation perpendicular to the planes of lowest surface energy [93, 94], such as (111) plane in FCC structures, (110) plane in BCC structures and (002) plane in HCP structures [95]. On the other hand, the crystallographic texture also depends on the orientation, shape, and size of the initial nucleus [96, 97]. Substrate temperature has significant effect in the mobility of the adatoms and surface diffusion, and hence affects the initial nucleus formation. The consequent crystallographic texture changes during film growth, accompanying with functional properties of thin film materials, including thin film yield strength/hardness [98-100]. Zhang *et al*. reported hardness enhancement of alumina thin film due to low substrate temperature deposition induced crystallization of Al_2O_3 [101]. Wu et al. performed microstructural and mechanical properties

characterization for Sc thin films as a function of substrate temperature, and found out that with the increase of substrate temperature, an initial softening was achieved due to grain growth, and then an strengthening was due to a combination of larger fraction of textured film, smaller grain size and higher densification [102].

Substrate temperature induced texturing could be observed in multilayer thin films as well [91]. Multilayer thin films have attracted more attention [33, 35, 103, 104] due to their advanced functional properties (electrical, magnetic, optical and mechanical) [24, 25, 27, 30, 31] compared to monolithic films of the constituent materials. With precise control of deposition temperature, the functional properties of multilayers can be further enhanced due to textured microstructure. In general, low deposition temperature could generate highly textured multilayers, which probably accompanies with better electrical and mechanical properties. Higher deposition temperature can generate solid solutes and intermetallic precipitates along interfaces and the precipitates were proved to enhance both mechanical [35] and magnetic properties [105]. High deposition temperature could probably lead to fully intermixing to form alloys, which provides an alternative method for alloy thin film fabrication. Although temperature deposited multilayers provide large potential for advanced properties and wide applications, detailed investigation of deposition temperature dependent microstructural and functional properties of multilayer thin films are still limited in literature.

In this work, the Ti/Ni multilayer system is selected as a model system to study substrate temperature induced microstructural and mechanical properties modifications. The first part of this work is to study the substrate temperature effect with a wide range temperature up to 500 ℃ by using one type of Ti/Ni multilayer system with individual layer thickness 20 nm. The second part is to further investigate coupled substrate temperature and layer thickness effect, with a wide range layer thickness from 200 nm to 10 nm and substrate temperature less than 300 ℃.

5.2 EXPERIMENTAL DETAILS

The Ti/Ni multilayer thin films were deposited using Ti (99.995%) and Ni (99.999%) targets in a magnetron sputtering system equipped with DC power supplies. The detailed deposition method is the same as introduced in Chapter 3. For substrate temperature effect study, Ti/Ni multilayer thin films with layer thickness 20 nm were deposited with the substrate temperature ranging from RT to 500 ℃. Heating was applied from the irradiation of two quartz lamps. For layer thickness effect study, Ti/Ni multilayer thin films were deposited with layer thickness varying from 250 nm to 10 nm and substrate temperature ranging from RT to 200 ℃.

The hardness of Ti/Ni multilayers was measured by Nanoindentation with a Berkvoic indenter tip. A minimum of 40 indents were performed on at least two specimens of each multilayer to obtain the average film hardness. XRD testing was carried out to determine the crystallographic texture, and SEM was conducted to obtain both surface and cross section morphologies of Ti/Ni multilayers.

5.3 SUBSTRATE TEMPERATURE EFFECT ON TEXTURE AND STRENGTHENING OF TI/NI MULTILAYER THIN FILMS

5.3.1 Hardness Results

Fig. 5.1 shows the hardness as a function of substrate temperature for Ti/Ni multilayers with individual layer thickness 20 nm. The hardness of as-deposited multilayer film under room temperature (RT) is around 5.99 GPa. A monotonically increased hardness was observed with the increase of substrate temperature. For example, 100 ℃ deposited multilayer shows an approximate hardness 6.81 GPa, about 13% increase, and 500 ℃ deposited film displays an ultrahigh hardness around 8.00 GPa, about 1/3 higher than RT case. For the convenience of the following presentation, the results are divided into four temperature regions: RT, low substrate temperature (low-ST) with T < 300 ℃, transitional substrate temperature with T = 300 ℃, and high substrate temperature (high-ST) with T > 300 ℃. This division of temperature will be used throughout the manuscript. In order to understand the hardness behavior with respect to the substrate temperature and the corresponding strengthening mechanisms, it is important to investigate the detailed microstructure evolution first.

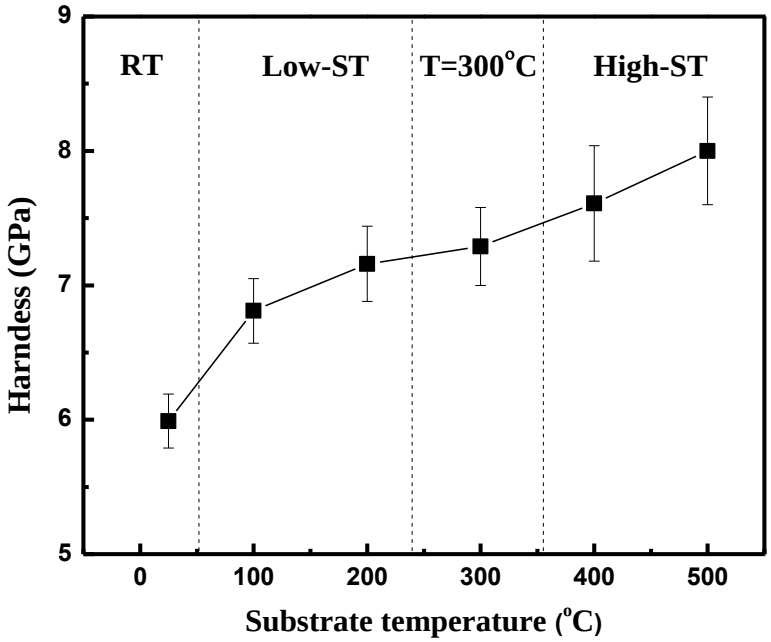

Figure 5.1: Hardness of as-deposited Ti/Ni multilayer thin films as a function of substrate temperature from RT to 500 ℃. The hardness increases monotonically with the substrate temperature. The temperature range is divided into four regions: RT, low-ST, 300 ℃ and high-ST.

5.3.2 Microstructure characterization

Fig. 5.2 shows XRD patterns for Ti/Ni multilayers deposited at a wide temperature range from RT to 500 ℃. Overall, minor change is observed in low-ST cases compared to RT case, while significant change observed in high-ST cases. Specifically, in RT case, a strong peak at 44.3 ° is detected corresponding to (111) plane from FCC Ni, and a tiny peak at 76.2 ° for Ni (200). Two small peaks at 35.5 ° and 38.6 ° correspond to (100) and (002) planes from HCP Ti. In low-ST cases, an obvious difference is the disappearance of Ti (100) peak. Ti (002) peak becomes stronger in 100 ℃ case, while slightly weaker in 200 ℃ case. The Ni (200) peak becomes less intense

with the increase of substrate temperature. In high-ST cases, a totally different spectra is detected with only one new broad peak at 43.5 °, which is probably formed by a combination of Ti-Ni intermetallic phase and an amorphous broad peak. The intermetallic phase corresponds to either one of NiTi (002), Ni_3Ti (004) and Ni_4Ti_3 (122), or a mixture. In 300 ℃ case, only one broad peak was detected as well, locating between the Ni (111) peak in low-ST cases and the intermetallic peak in high-ST cases. This peak could correspond to a combination of Ni (111) phase, Ti-Ni intermetallic phases and amorphous structure.

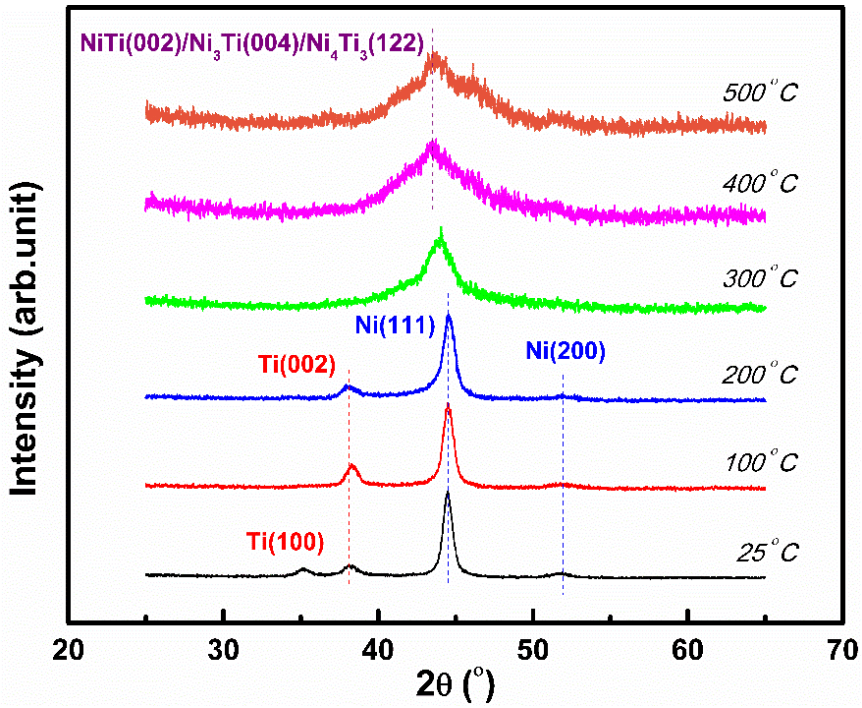

Figure 5.2: XRD patterns of Ti/Ni multilayers deposited at a wide range of substrate temperature from RT to 500 ℃. Similar spectra were achieved in low-ST cases, and a broad intermetallic peak was only detected in high-ST cases, corresponding to either one of NiTi (002), Ni_3Ti (004) and Ni_4Ti_3 (122), or a combination of them.

Based on the XRD results, the Ti/Ni multilayer crystallographic texture evolution with the substrate temperature can be summarized as following. At the initial stage of film growth, the nuclei have mixed orientations with (111) and (200) for FCC Ni, (100) and (002) for HCP Ti. After the impingement of crystal islands, Ni crystals with (111) orientation and Ti crystals with (002) orientation, which have lower surface energy, grow quicker during film growth and thus occupy more volume of the films. The corresponding growth rates of preferred orientations would be determined by adatom mobility and shadowing effect. Under RT, the adatom mobility is limited and shadowing effect is significant [106, 107], resulting in crystals with different orientations in the film. In 100 ℃ case, provided with more energy, the adatom mobility is enhanced and shadowing effect is limited, promoting the development of preferred crystallographic texture and resulting in the weakening of Ni (200) peak and disappearance of Ti (100) peak. In 200 ℃ case, the adatom mobility is even higher, leading to strong Ni (111) and Ti (002) peaks. On the other hand, higher substrate temperature also induces atomic diffusion along Ti/Ni interfaces, resulting in slightly weaker Ti (002) peak compared to 100 ℃ case. A slight peak shifting is observed for Ti (002) peak due to the compressive thermal stress in Ti layer in film growth direction. In addition, peak broadening can be also observed for both Ti (002) and Ni (111) peaks. In general, the peak broadening is generated from either smaller grain or larger strain. In 300 ℃ case, higher substrate temperature provides sufficient energy for massive diffusion during thin film deposition, leading to further intermetallic precipitates along interfaces. Eventually, a mixture of Ni (111) phase and intermetallic phase is formed. In high-ST cases, with high temperature and sufficient energy, the large adatom surface mobility is generally adequate to form the phases predicted by the phase diagram [107]. According to Ti-Ni phase diagram, Ti-Ni intermetallic phases can be detected with temperature higher than 400 ℃. A broad peak is observed in high-ST cases, probably due to small

intermetallic grains. Since Ni and Ti has an approximate ratio 1:1, assumed full intermixing of Ti and Ni layers, the intermetallic phase could come from a martensitic NiTi (B19'), which is probably formed after cooling from high temperature. In this case, NiTi (002) could be the detected intermetallic peak. Besides, (002) plane is also the preferred crystallographic texture in B19' structure since it is the closest packed plane. That could be the reason why only NiTi (002) peak detected in the XRD spectra. However, this peak might also correspond to Ni_3Ti (004) phase. Since Ni has higher mobility than Ti, it is possible to have more Ni atoms in some local areas, promoting the formation of Ni_3Ti phase. Ni_3Ti has a hexagonal structure, and (001) plane family is preferred due to the lowest surface energy. In addition, this peak might partially corresponds to a metastable structure Ni_4Ti_3, which was detected as precipitates in NiTi structure [108]. The XRD results here confirm that high-ST deposition of Ti/Ni multilayers could be an alternative fabrication process for TiNi SMA, and furthermore, the intermetallic is formed with preferred crystallography texture.

Next, the surface and cross-section morphological evolution in Ti/Ni multilayers with substrate temperature was shown by SEM images. Fig. 5.3 shows the surface SEM images samples deposited under various substrate temperature from RT to 500 ℃. In RT case, the plan-view shows a homogeneous Ni surface with uniform grain distribution as shown in Fig. 5.3(a). The Ni grain size is around 25 nm. In 100 ℃ case, homogeneous grain surface was observed while with much larger grain size around 70 nm. It is interesting to note that grain growth in this case does not soften the material. The grain growth is due to higher temperature activated grain boundary migration. The grain boundaries of initial crystals can extend outward during the film growth until impingement, and thus larger grains can be formed. In 200 ℃ case, similar surface morphology

was observed, although the grain boundary is not as sharp as that in 100 ℃ case. A similar film growth mode is expected as in 100 ℃ case, but there is more diffusion due to higher temperature, which is also confirmed by XRD spectra. Surface diffusion leads to indistinct grain boundaries on the surface as shown in Fig. 5.3(c). In 300 ℃ case, even less distinct grain boundaries were observed on the surface, and there are more voids between grains as shown in Fig. 5.3(d). In high-ST cases, totally different surface morphologies were shown. The dome shaped grains were observed closely packed on the surface in 400 ℃ case, and a recrystallized grain surface in 500 ℃ case. According to the XRD results, only Ti-Ni intermetallic phases were detected in high-ST cases. The domed grains and recrystallized grains are probably alloy grains. The domed alloy grains show an average grain size 50 nm. The recrystallized particles are composed of several small grains and well separated with each other, leaving voids on the surface. The morphologies in high-ST cases indicate large surface diffusion and bulk diffusion under such high deposition temperature.

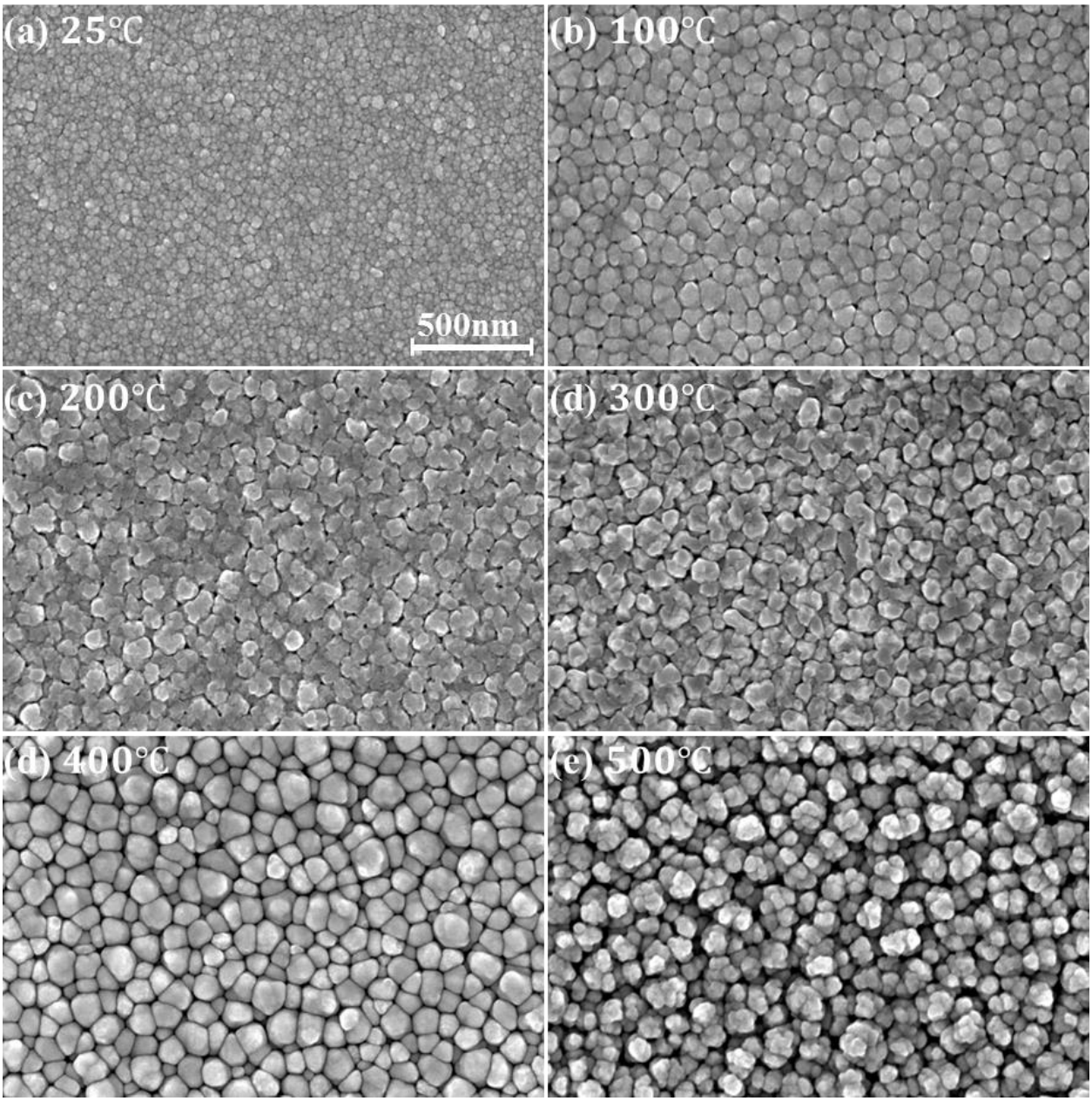

Figure 5.3: SEM images of surface morphology of Ti/Ni multilayer films deposited with various substrate temperatures from RT to 500 ℃. Homogeneous grains are shown in RT, grain growth in low-ST, domed alloy grains in 400 ℃, and recrystallization in 500 ℃.

The as-deposited film morphology with substrate temperature can be predicted by Thornton's Model. The zone I structure is defined as fibres of small diameter with $0 < T_s / T_m < 0.2$. The zone T structure is inhomogeneous, with fine crystalline at the substrate, composed of V-shaped grains in the next thickness range while columnar in the upper part with $02 < T_s / T_m < 0.4$. The zone II structure is characterized by columnar shaped grains from the bottom to the top with $0.4 < T_s / T_m$. The zone III structure is characterized by equi-axed three dimensional grains with larger T_s / T_m. Fig. 5.4 shows the cross-section morphology evolution of Ti/Ni multilayers with substrate temperature. In RT case, layered structure was clearly observed in the SEM image, with bright layer Ni and dark one Ti as shown in Fig. 5.4(a). According to Thornton's Model, RT deposited film generally follows Zone T structure. Grain growth could be expected during film growth. For multilayers in this work, however, grain growth can be disrupted by layered structure. Due to the low adatom mobility and shadow effect, nucleation occurs when each new layer starts to grow, leading to incoherent interface in RT-deposited Ti/Ni multilayers. In low-ST cases, textured films were observed with columnar structure extending through the layers. The columnar width is comparable with surface grain size around 75 nm. The cross-section morphology follows structure from Zone T to Zone 2, with columnar structure due to competitive growth mode and restructuration growth mode. The distinct layers were still observed within columns, indicating few nucleation at each layer, which is probably due to the enhanced adatom mobility at higher temperature. The interfaces in this case could be coherent or semi-coherent within columnar grains. The grain growth compared to RT case is due to grain boundary mobility at higher temperature. In 300 ℃ cases, more distinct columnar structure is observed from bottom to top, which follows the structure in Zone 2 as shown in Fig. 5.4(d). When the temperature is higher, such as 300 ℃ here, grain boundary migration is significant, leading to expansion of initial crystal islands during

film growth, and eventually a complete columnar structure can be formed following restructuration growth mode [107]. The coherent or semi-coherent interfaces within columnar grains can generate large strain due to lattice mismatch between Ti and Ni, which explains the broader Ti and Ni peaks detected at higher temperature in aforementioned XRD spectra.

In high-ST cases, the SEM images show a completely different cross-section morphology with columnar structures in the upper part of the film and layered structures near the substrate as shown in Fig. 5.4 (e) and (f). Almost no layered structure is observed within the column. According to the XRD results, the columns could be Ti-Ni alloys. The alloys are formed due to high temperature-induced intermixing and intermetallic formation, and the columns are formed according to restructuration growth mode in Zone 2 as discussed in 300 ℃ case. Thus, slightly increased column width was observed in high-ST cases. As to the layered structure near the substrate, there are two possible reasons. Since Ti-Ni intermetallic formation can be treated as a recrystallization process, there will be a time delay for its occurrence[31]. Thus, the initial film growth could be expected similar as in 300 ℃ case, that is, layered structure near the substrate. In addition, with high substrate temperature, the factor of crystal size during impingement could play a more important role than surface diffusion during film growth [96, 97]. Upon impingement, the crystal islands with other orientations have smaller size than those from preferential textures such as Ni (111) and Ti (002), and thus develop faster. As a result, the first layers display less distinct columnar structure and less ordered interfaces compared to 300 ℃ case. In 500 ℃ case, the alloying columns become slightly wider and fewer layers were observed near the substrate. In the upper part of the films, recrystallization was observed locally, which is consistent with surface

morphology result as shown in Fig. 5.3(e). This morphology indicates that 500 ℃ deposition can produce film structure as a transition from Zone 2 to Zone 3 in Thornton's Model.

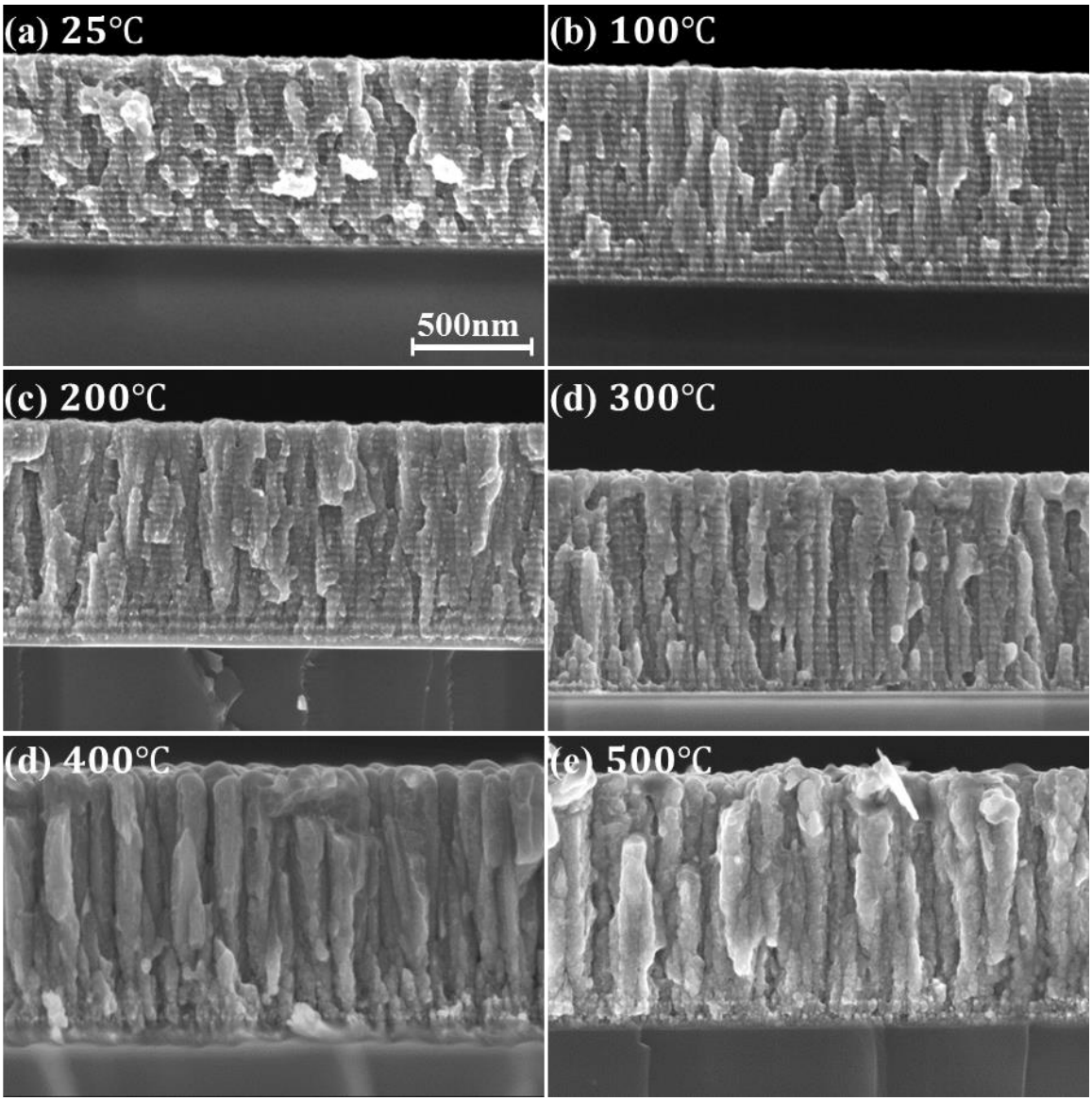

Figure 5.4: SEM images of surface morphology of Ti/Ni multilayer films deposited with various substrate temperatures from RT to 500 ℃. Layered structure with incoherent interface was observed in RT case, textured film in low-ST cases with columnar structure extending through layers, and columnar alloy grains in high-ST cases with disintegration of layered structures.

Fig. 5.5 shows the XPS depth profiles for samples deposited under various substrate temperature from RT to 500 ℃ with individual layer thickness 50 nm. The larger layer thickness 50 nm is used here in order to achieve high resolution depth profile. In RT case, clear periodic depth profiles are observed for both Ti and Ni, indicating layered structure in RT case. In low-ST cases (100 ℃ and 200 ℃), similar periodic profiles are shown compared to the RT case, while obvious intermixing could be indicated in 300 ℃ case, indicating obvious diffusion along Ti-Ni interfaces. In high-ST cases, almost no periodic profiles are observed for both Ti and Ni, indicating that fully intermixed and complete alloyed structure is probably formed.

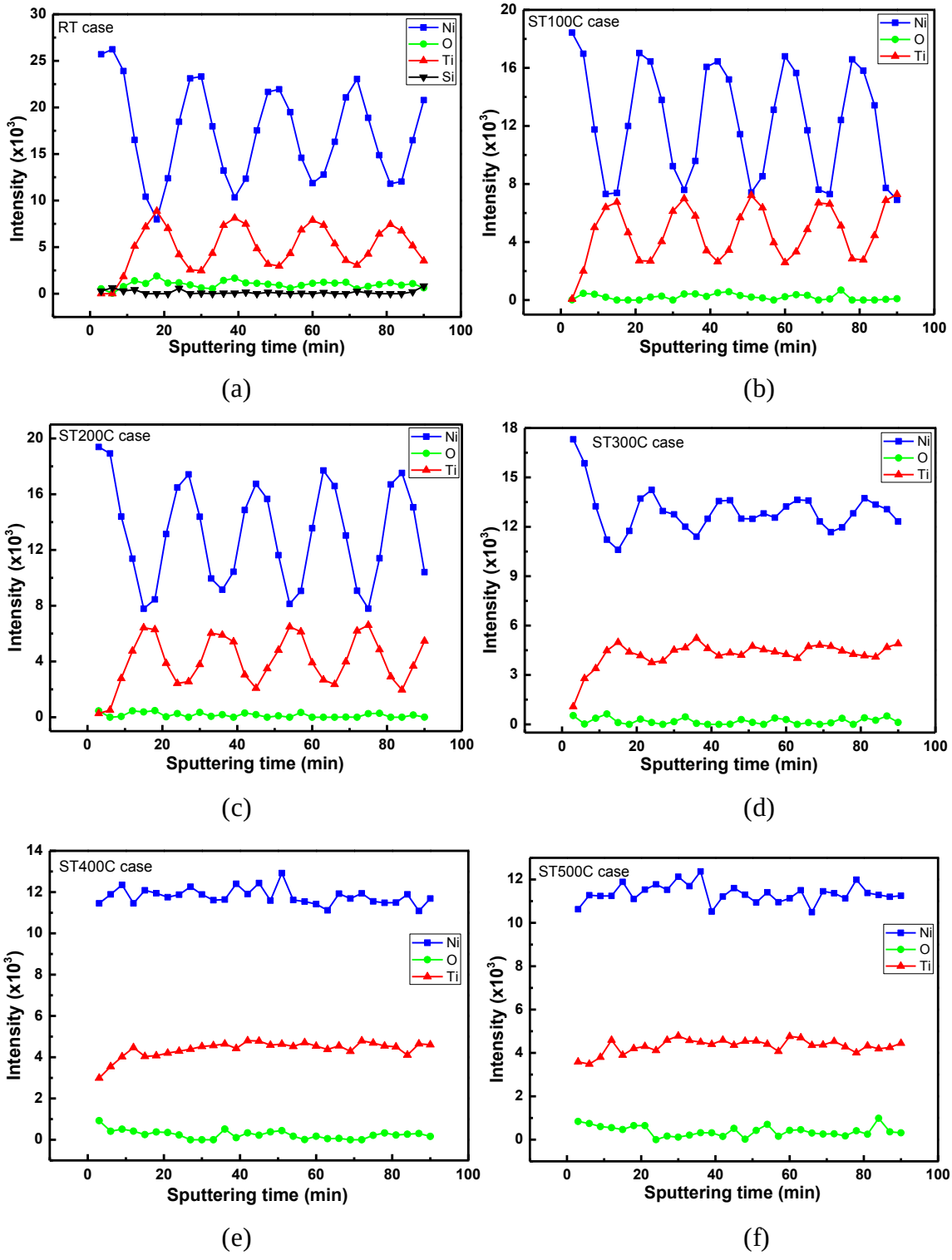

Figure 5.5: XPS depth profile for Ti/Ni multilayer thin film with different substrate temperature from RT to 500 ℃. No obvious change is observed in low-ST cases, and significant diffusion is indicated in 300 ℃ case, and fully intermix indicated in high-ST cases.

5.3.3 Discussion

From the aforementioned hardness behavior and microstructure characterization, the effect of substrate temperature on microstructural and mechanical properties is significant. Fig. 5.6 shows a schematic of strengthening mechanisms evolution for Ti/Ni multilayers with the increase of substrate temperature. In 100 ℃ case, larger grain size is observed than that in RT case as shown in Fig. 5.3(b) and it is well accepted that grain growth can cause softening. However, instead of softening, an obvious strengthening is achieved in 100 ℃ case. In this work, the layer thickness is about 20 nm, smaller than the average grain sizes (~25 nm in RT case and ~70 nm in 100 ℃ case), so the layer thickness contributes to the dominant feature size for dislocation associated deformation behaviors such as dislocation pile-up against the interfaces or single dislocation bowing within interfaces. Layer thickness rather than grain size would determine material strength in this case. The mechanical strengthening is partially due to texturing with preferential orientations, such as Ni (111) and Ti (002) as indicated by Fig. 5.2. In addition, columnar structures are observed extending through the layers, and the Ti-Ni interfaces are coherent or semi-coherent within the large columnar grains, providing stronger barrier for slip transmission than incoherent interfaces in RT case. Thus the strengthening from RT case to 100 ℃ case is due to preferred orientation and ordered Ti/Ni interfaces. In 200 ℃ case, the columnar structure is more distinct, providing more strengthening. Besides, obvious atomic diffusion is indicated from the XRD results and SEM images. The further strengthening can be from solid solute of diffused Ni and Ti atoms. It is interesting to note that the strengthening mechanisms of Ti/Ni multilayer thin films from low-ST deposition are totally different with those from low temperature annealing in our previous

work. There is no obvious microstructural modifications after low temperature annealing, and the strengthening mechanism is grain boundary relaxation.

In 300 ℃ case, the strengthening partially comes from even more distinct columnar cross-section structure. In previously reported works on Ti/Ni multilayer thin films[29], 300 ℃ annealing could generate amorphous structure due to extensive atomic diffusion and intermixing, however, no Ti-Ni intermetallic phase was detected. In this work, Ti-Ni intermetallic precipitates could be formed along Ti/Ni interfaces according to above microstructure analysis. Further strengthening is due to solid solutes of diffused Ti and Ni atoms as well as Ti-Ni intermetallic precipitates.

In high-ST cases, the high hardness corresponds to Ti-Ni alloys. Further strengthening comes from preferred crystallography texture of Ti-Ni intermetallic. Note that 400 ℃ annealing induces complete Ti-Ni alloy, while with mixed intermetallic phases[29]. Thus depositing at a low temperature and annealing at a high temperature does not produce the same microstructure, and generally not the same phases as depositing at the same high temperature. In 500 ℃ case, recrystallization is observed with smaller grain size on the surface, which results in further strengthening.

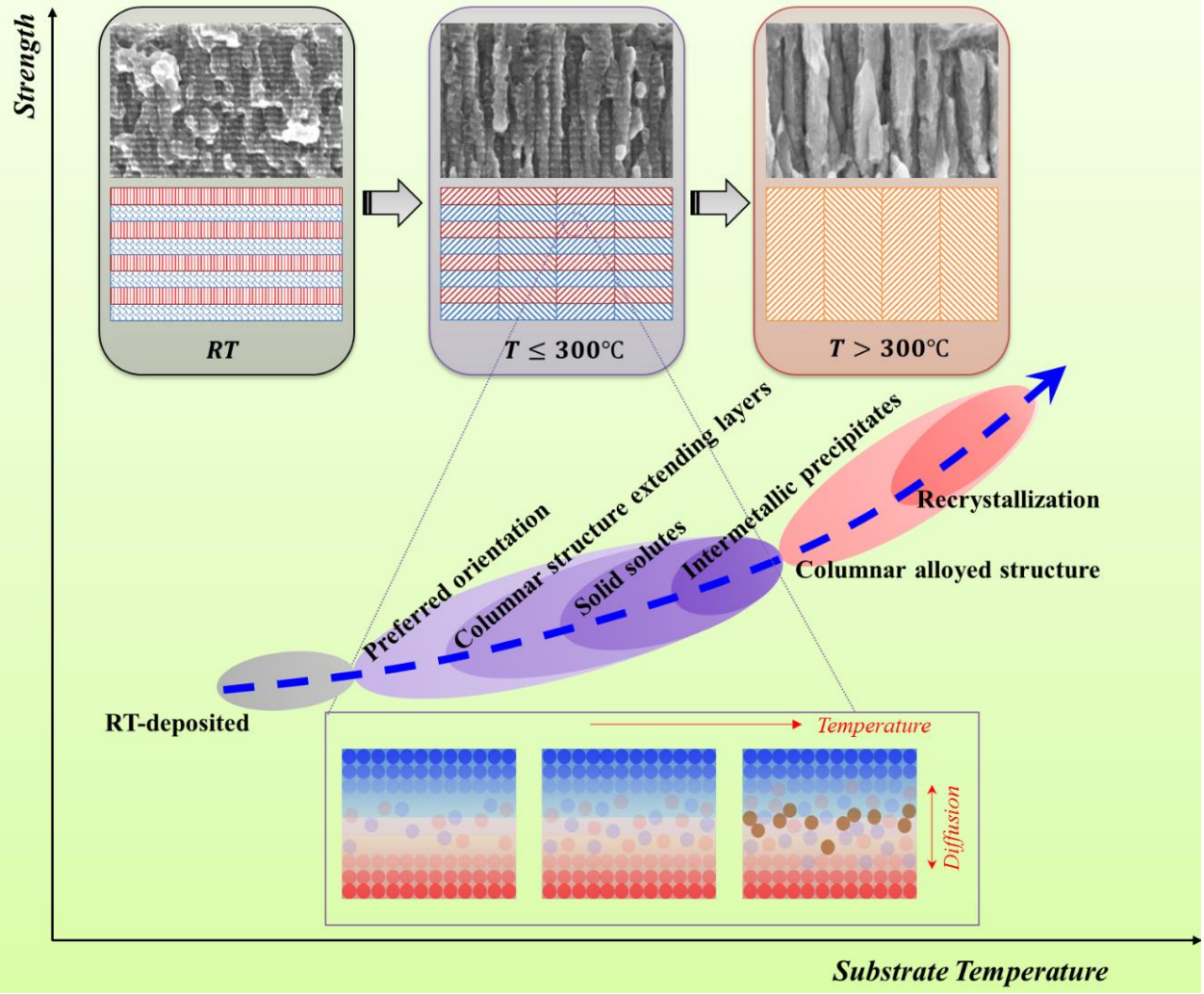

Figure 5.6: A schematic of strengthening mechanism of Ti/Ni multilayers deposited with different substrate temperature. With the increase of substrate temperature, the strengthening could be due to preferred orientations, ordered interfaces within columnar structures, solid solution, intermetallic precipitation, columnar alloys and alloying recrystallization.

5.4 LAYER THICKNESS EFFECT ON TEXTURE AND STRENGTHENING OF TI/NI MULTILAYER THIN FILMS

5.4.1 Hardness

Fig. 5.7 shows the hardness results for Ti/Ni multilayer thin films with a wide layer thickness range from 250 nm to 10 nm deposited with substrate temperature (ST) 100 ℃ and 200 ℃ as well as those deposited under room temperature (RT). A strong layer thickness dependent hardness behavior is observed in all cases. For RT case, increased hardness is observed with decreasing layer thickness. This trend has been obtained in various metallic multilayer thin films in previously reported works. For ST case, an overall strengthening is observed. For example, Ti/Ni multilayer films with layer thickness 125 nm, shows about 5% increase in hardness after deposition at 100 ℃ and about 30% increase at 200 ℃. This hardness achieved after deposition at 200 ℃ is even higher than the maximum hardness value from multilayers in RT case. The strengthening trend as the substrate temperature increases is consist with previously reported works. Furthermore, this work shows the layer thickness dependent strengthening behavior with different substrate temperature as shown in the insert figure in Fig. 5.7. For multilayer films deposited at 100 ℃, more strengthening is achieved as the layer thickness decreases with layer thickness below 100 nm (thin layer), however, more strengthening is observed as the layer thickness increases with layer thickness above 100 nm (thick layer). For multilayer films deposited at 200 ℃, more strengthening in samples with thin layer than those with thick layer.

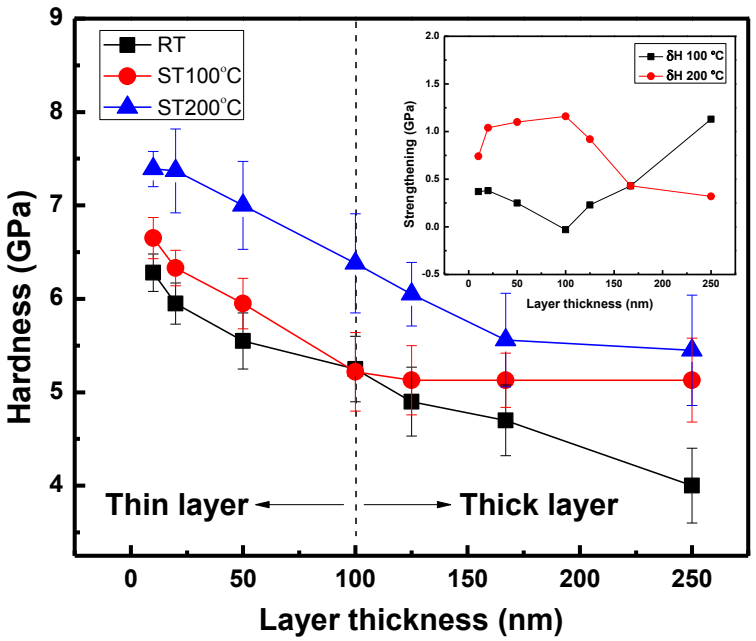

Figure 5.7: Hardness result for Ti/Ni multilayer thin films deposited under RT and with substrate temperature 100 ℃ and 200 ℃. An overall strengthening is observed in films deposited with ST. Insert figure shows the strengthening in multilayers deposited at 100 ℃ and 200 ℃. The strengthening behavior with various ST is different between multilayers with thin layer and multilayers with thick layer.

5.4.2 Microstructure

Microstructure modifications are expected to play an important role in strengthening behavior in multilayers with thin and thick layer. Fig. 5.8 shows XRD patterns for RT, 100 ℃ and 200 ℃ deposited Ti/Ni multilayer thin films with layer thickness 50 nm (Fig. 5.8(a)) and 250 nm (Fig. 5.8(b)). For multilayers deposited under RT, a strong peak at 44.3 ° corresponds to Ni (111), the peak at 76.2 ° for Ni (200), and the peak at 38.6 ° for Ti (002). In thin layer case, an obvious peak is detected at 35.5 °, corresponding to Ti (100), while limited Ti (100) peak intensity is shown in

thick layer case, indicating that layer thickness has a significant effect on crystallographic texture formation. At the initial stage of film growth, nuclei are formed with mixed orientations, and there is no grain boundary immigration under RT deposition. Crystals with mixed orientation can be formed. For thin layer case, the layer covers crystals with mixture orientation, and thus the film shows all phases in XRD result. For thick layer case, the film follows a competitive growth mode. Preferred crystallographic texture Ni (111) and Ti (002), which have lower surface energy, grow quicker and occupy more volume of the film. For multilayers deposited at 100 ℃, significant phase change was observed in thin layer case. Ti (100) peak disappears and Ti (002) peak becomes stronger. The same phenomenon was observed in Ti/Ni multilayers with layer thickness 20 nm after 100 ℃ deposition. Compared to RT, 100 ℃ deposition provides more energy to enhance the adatom mobility and overcome shadowing effect, so that the preferred crystallographic texture can develop quickly, leading to strengthening of Ti (002) phase and disappearance of Ti (100) phase. However, it is interesting to note that Ti (002) peak becomes weaker in thick layer case, which is probably due to atomic diffusion along the Ti/Ni interfaces. For the multilayers deposited at 200 ℃, both thin layer case and thick layer case display the same phase modification. For Ti, the only peak Ti (002) becomes weaker, and for Ni, Ni (200) peak becomes stronger, indicating the ratio of Ni (111) phase in Ni layer decreases. There could be several reasons for the intensity weakening of preferred phases Ti (002) and Ni (111). At higher deposition temperature, the atomic diffusion becomes more significant, and there is possibility of recrystallization. Both can strongly affect the volume ratio of dominant phases. On the other hand, the initial crystal size could play a more important role than surface diffusion during film growth. The islands with preferred orientation generally have larger size, and thus develop slower in this case. In addition, compared to the results in 100 ℃, an obvious left shifting of Ti (002) peak is observed in both thin layer case and thick

layer case, which is probably due to the compressive thermal stress in Ti layer in film growth direction. Slightly peak broadening can be also observed, indicating the possibility of large strain within the multilayers after 200 ℃ deposition.

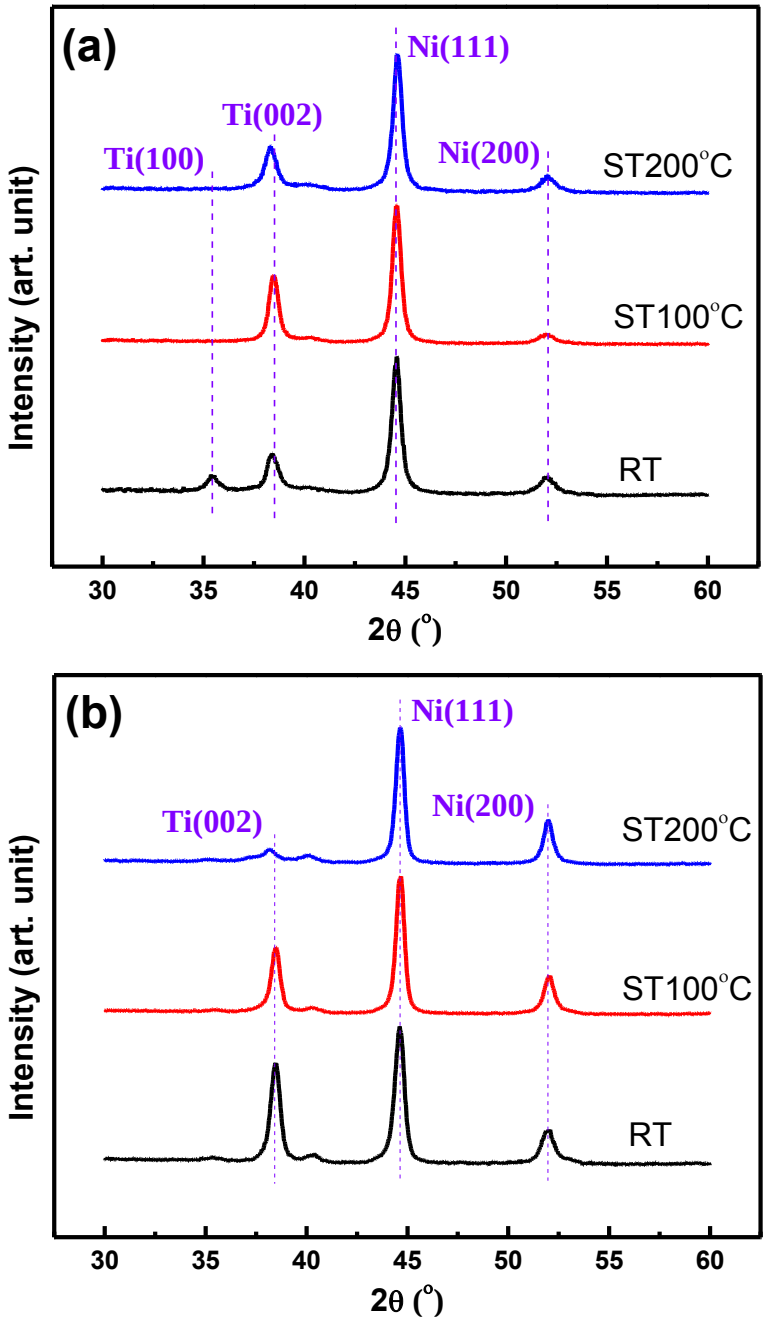

Figure 5.8: XRD results for Ti/Ni multilayers deposited under RT, 100 ℃ and 200 ℃ with different layer thicknesses (a) 50 nm and (b) 250 nm. The crystallographic texture modifications are different in multilayers with thin layer and thick layer.

Fig.5.9 shows the surface morphology of RT, 100 ℃ and 200 ℃ deposited Ti/Ni multilayer films with a wide range of layer thickness from 20 nm to 250 nm. Overall, the plan views indicate that all the multilayer films have homogeneous Ni surfaces with uniform grain distribution. However, with different layer thickness, different surface grain size is observed in RT deposited multilayer films, while similar surface grain size is maintained in 100 ℃ and 200 ℃ deposited multilayer films. Fig.5.10 shows the relationship between surface grain size and layer thickness for all the multilayer films based on measurements from the above SEM images (solid symbol). For the multilayers deposited at RT, the average surface grain size increases from 28 nm to 72 nm with the individual layer thickness changes from 20 nm to 250 nm. In addition, for multilayers with thick layer, much larger particles are observed to compose of a few grains, which was observed in our previous work. According to Thornton's model, film growth under RT generally follows Zone T structure. Grain growth could be expected during film growth, and thus larger grain size is observed in multilayers with thick layer. Shadowing effect is significant, and thus large particle is formed by several grains. For the multilayers deposited at 100 ℃, Fig. 5.10 shows the average surface grain size 70 nm regardless of the layer thickness. The layer thickness independent grain size is probably due to grain boundary immigration during film growth, and the critical crystal size is about 70 nm during impingement. For the multilayers with thick layer, the surface is well packed and no large particle is observed as in RT deposited multilayers, indicating the shadowing effect is limited during 100 ℃ deposition. For the multilayers deposited at 200 ℃, similar surface grain size is maintained as those at 100 ℃ as shown in Fig. 5.4, while the grain boundary is not as sharp as those at 100 ℃ as shown in Fig. 5.3, indicating similar growth mode during low temperature deposition (T<300 ℃), while more atomic diffusion under higher deposition temperature. This is

also confirmed by the aforementioned XRD results for multilayers with both thin and thick layer as shown in Fig. 5.8.

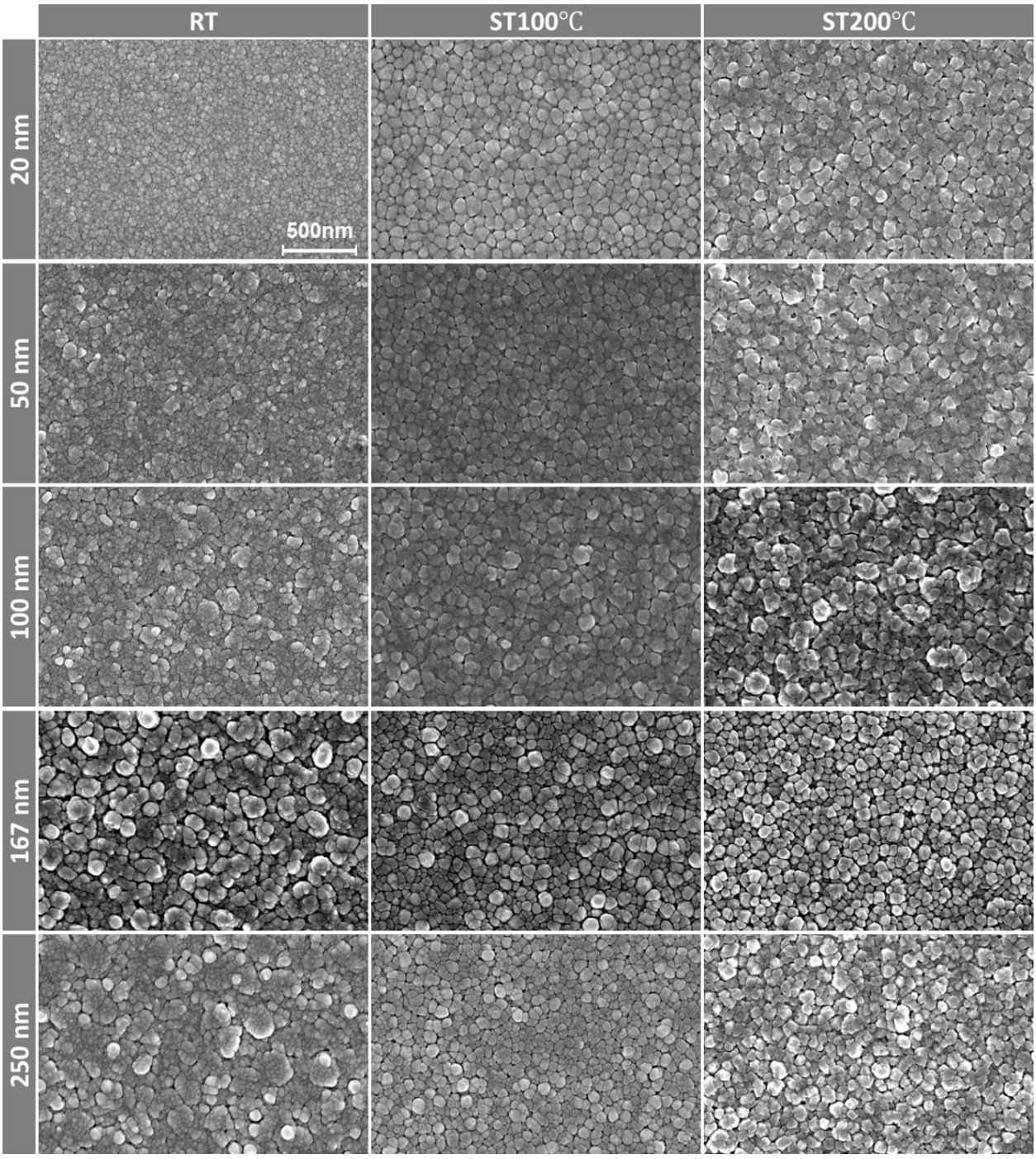

Figure 5.9: SEM images of surface morphology of Ti/Ni multilayer films deposited at RT, 100 ℃ and 200 ℃ with a wide range of layer thickness from 20 nm to 250 nm. In RT case, different grain size is shown in multilayers with different layer thickness, while similar grain size is observed in multilayers in 100 ℃ and 200 ℃ cases.

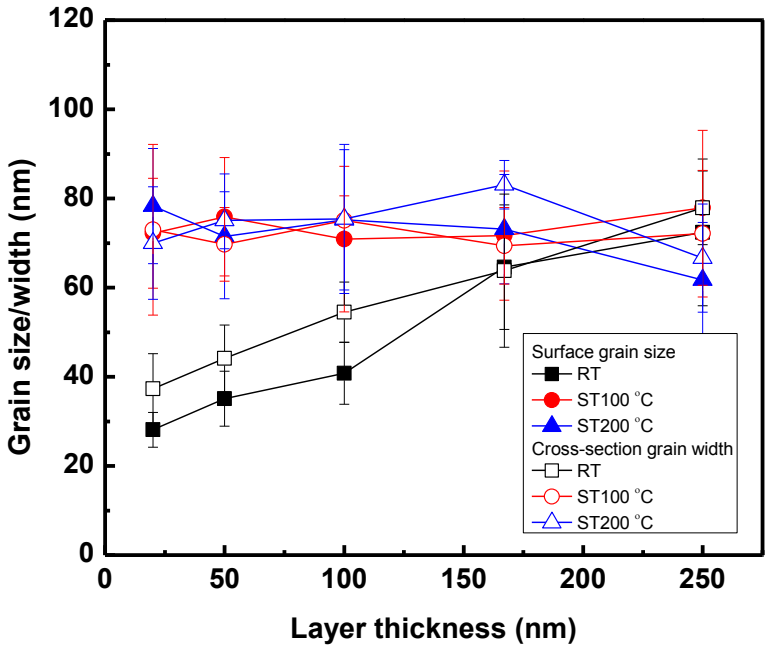

Figure 5.10: Surface grain size and cross-section columnar grain width in RT, 100 ℃ and 200 ℃ deposited Ti/Ni multilayers with layer thickness from 20 nm to 250 nm. Surface grain size was measured based on surface SEM images in Fig. 5.3 and cross-section columnar grain width was measured based on cross-section SEM images in Fig. 5.4.

Fig. 5.11 shows the cross-section morphology of RT, 100 ℃ and 200 ℃ deposited Ti/Ni multilayer films with a wide range of layer thickness from 20 nm to 250 nm. A strong layer thickness dependent cross-sectional morphology modification has been observed in both RT and ST deposited multilayers. For the multilayers deposited at RT, columnar grains are clearly observed in Ni layer and equi-axed grains in Ti layer. Incoherent interface is generated between Ti and Ni layers, indicating nucleation might occur upon each layer growth. The film structure follows Zone T in Thornton's model, and Ni layer grows according to competitive growth mode. Thus the columnar grain width increases with the increasing of layer thickness as shown in Fig.

5.4. It is interesting to note that Ti film also shows columnar grain structure in previously reported works. For multilayers deposited at 100 ℃, textured films are observed with columnar structure extending through the layers in 20 nm case, although the columns are not highly distinct. Within the columns, the interface is expected to be coherent or semi-coherent. Coherent interface was detected in previous works when the layer thickness is ultra-thin for RT deposited metallic multilayer films. Columnar Ti grains are clearly observed in 50 nm and 100 nm cases. For multilayers with thick layer (167 nm and 250 nm), the film exhibits different structure in the upper part and bottom part, indicating the Si substrate and layers themselves can affect the next layer growth. In the upper part of the film, columnar grains are observed in both Ti layer and Ni layer, and large columns are also observed to extend through layers. Although the cross-section morphologies are not exact the same in multilayers with different layer thickness, the columnar grain width is about the same, 70 nm, which is comparable with the surface grain size as shown in Fig. 5.10. The layer thickness independent columnar grain width indicates that the critical crystal size could be around 70 nm during impingement for all the cases, and the grain boundary immigration plays an important role in determine the critical size upon impingement. For the multilayers deposited at 200 ℃, the columnar structure is more distinct in 20 nm case with similar column width. More distinct columnar grain structure is observed in Ti layer in other cases, however, equi-axed grains are observed in Ni layer. Thus no large columns are observed to extend through layers in multilayers with thick layer. In addition, obvious atomic diffusion is observed at 200 ℃, especially for Ni layer. This also confirms the modifications of crystallinity and surface morphology from the aforementioned XRD results and SEM images.

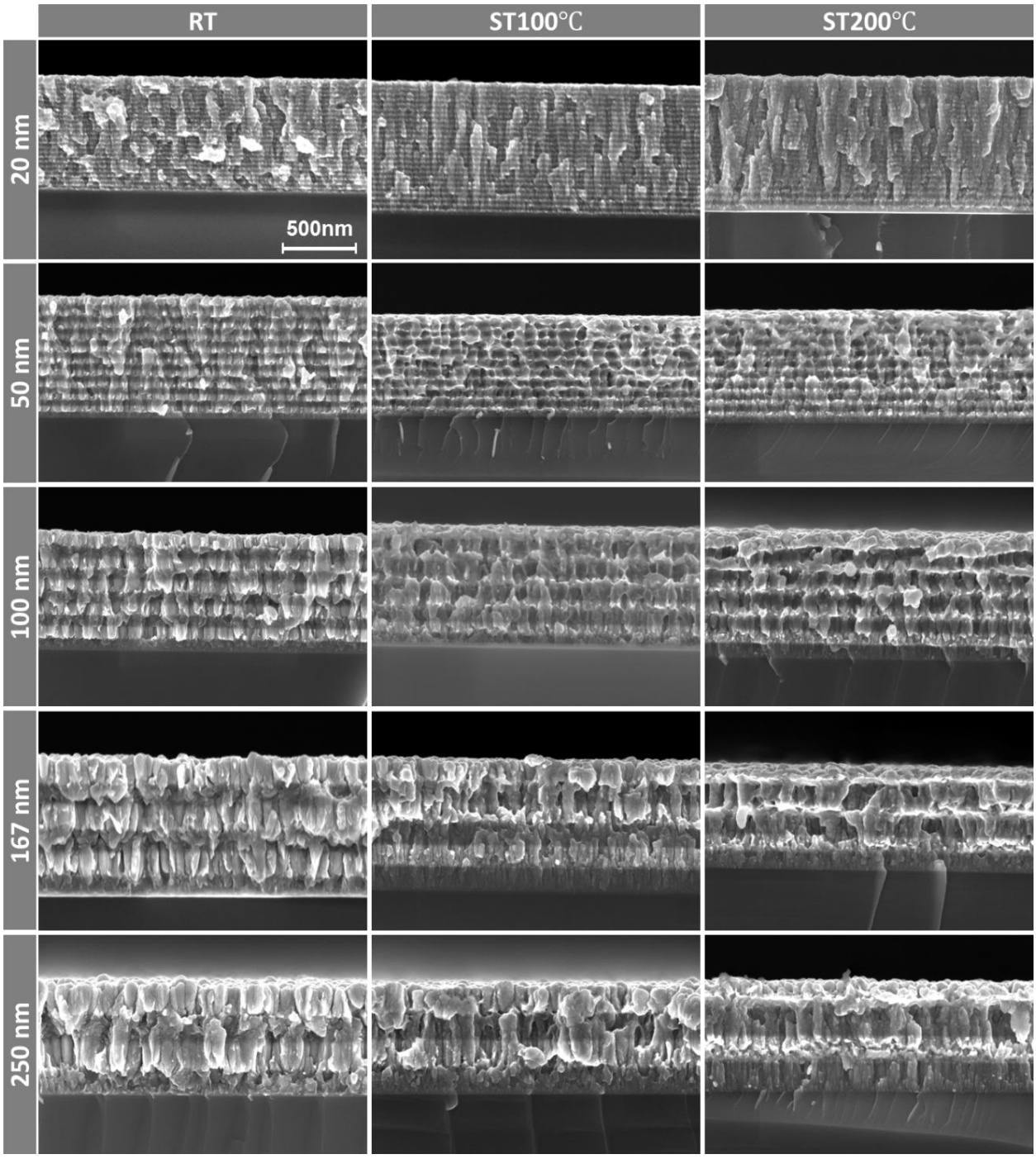

Figure 5.11: SEM images of cross-section morphology of Ti/Ni multilayer films deposited at RT, 100 ℃ and 200 ℃ with a wide range of layer thickness from 250 nm to 25 nm.

5.4.3 Discussion

With the understanding of microstructure modification for Ti/Ni multilayers under different deposition temperature, the hardness behavior and strengthening mechanisms are discussed as following. For RT deposited multilayers, when the layer thickness is above 50 nm, the hardness can be fitted by the Hall-Petch model:

$$H = H_0 + kh^{-0.5} \tag{5.1}$$

where H is the hardness, H_0 is a constant, caused by lattice friction, k is the Hall-Petch slop, and h is the individual layer thickness. By fitting with experimental data, we obtained $H_0 = 3.0$ GPa, and $k = 22.06\ GPa\sqrt{nm}$. Note that the hardness in 250 nm case was not selected for fitting because the indentation depth is less than 200 nm, the hardness result can be mainly affected by the top Ni layer. The Hall-Petch slope can be used to estimate the peak strength for multilayers via:

$$k_\tau = \sqrt{\frac{\tau^* \mu b}{\pi(1-\nu)}} \tag{5.2}$$

where $k_\tau = k/(2.7 \times 3.1)$, τ^* is the interface barrier strength for slip transmission, μ is the shear modulus, b is the Burgers vector, and ν is the Poisson ratio. Substituting $\mu = 76$ GPa, $b = 0.25$ nm, and $\nu = 0.31$ for Ni material, we obtained $\tau^* = 0.79$ GPa, yielding a peak strength for RT deposited Ti/Ni multilayers 6.6 GPa, which is close to the maximum hardness 6.3 GPa achieved in experiments. The good fitting of the Hall-Petch model and precise estimate of peak strength indicate that dislocation pile-up against interface is the dominated strengthening mechanism for multilayers with thick layer.

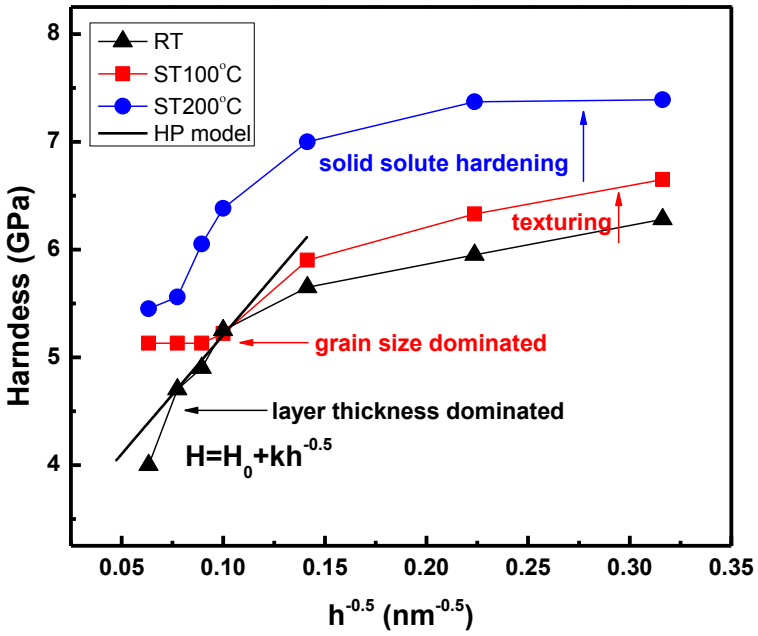

Figure 5.12: Hardness of RT, 100 ℃ and 200 ℃ deposited Ti/Ni multilayers with layer thickness from 10 nm to 250 nm. The hardness of RT deposited multilayers is fitted by using Hall-Petch model.

However, for 100 ℃ deposited multilayers with thick layer, similar hardness value is maintained when the layer thickness is above 50 nm, indicating the broken down of layer thickness mediated Hall-Petch relationship. In this case, the surface grain size and columnar grain width is about 70 nm, much less than layer thickness, so the grain size, rather than layer thickness is the dominate feature size for dislocation pile-up against boundaries. Thus a similar hardness level is achieved for the multilayers with thick layer since these samples have similar surface grain size. For multilayers with thin layer, preferred crystallographic texture is formed and thus texturing is the dominated strengthening mechanism. With thinner layer, preferred crystallographic texture

occupies more volume, and thus more strengthening is achieved. In addition, columnar structure can be easier to form for multilayers with thinner layer, in which coherent or semi-coherent interfaces are probably formed, providing more barrier to dislocation transferring. For the multilayers deposited at 200 ℃, obvious atomic diffusion is observed from XRD and SEM results, and as a result, solid solution strengthening from diffused Ti and Ni atoms is the dominated mechanism. For multilayers with thin layer, columnar structure becomes more distinct, providing further strengthening. For multilayers with thick layer, recrystallization is observed in Ni layer, which might slightly soften the material. Thus, less strengthening is achieved in multilayers with thick layer and more strengthening in multilayers with thin layer.

5.5 CONCLUSION

Significant texture strengthening is observed in Ti/Ni multilayer films deposited with various substrate temperature. Under low substrate temperature deposition, columnar structure is observed extending through Ti/Ni layers, and texture strengthening comes from preferred crystallography orientations and ordered Ti/Ni interfaces. With the increase of substrate temperature, the columnar structure becomes more distinct, providing more strengthening. Meanwhile, there is more atomic diffusion and intermixing along the interfaces, promoting the formation of Ti-Ni intermetallic precipitates. Eventually, solid solution strengthening of diffused atoms and precipitation strengthening of Ti-Ni intermetallic becomes the dominated strengthening mechanisms. Under high substrate temperature, a columnar Ti-Ni alloying film is observed with disintegration of Ti/Ni layered structure. High hardness corresponds to Ti-Ni alloys and recrystallization with even higher temperature.

In addition, significant size effect in texturing is observed in Ti/Ni multilayer thin films deposited with substrate temperature. Overall strengthening is achieved in samples deposited at 100 ℃ and 200 ℃, while the strengthening behavior depends on layer thickness. At 100C, preferred orientation and ordered interface is the dominated strengthening mechanism in thin layer case, and with the thinner layer, the more strengthening. Smaller grain size is the dominated strengthening mechanism in thick layer case, and with the thicker layer, the more strengthening. At 200 ℃, solid

solute hardening is the dominated strengthening mechanism. For thin layer case, texturing provide more strengthening, and a result, more strengthening in this case.

Chapter 6. LASER-INDUCED MICROSTRUCTURAL EVOLUTION AND SURFACE STRENGTHENING OF TI/NI MULTILAYER THIN FILMS

6.1 INTRODUCTION

Laser treatment has attracted more attention recently on micro and nano-scale materials in many ways [109]: fabrication of stable nanoparticles [110, 111] and nanocomposite thin films [112] by laser ablation; laser crystallization, laser doping and laser cleaning in semiconductor industry; and laser processing for micro and nanostructured solids, such as laser-induced forward transfer (LIFT) [113] and laser-induced periodic surface structures (LIPSS) [114-117]. LIPSS have been extensively reported and found large potential in micromachining for microelectronics and micro-electro mechanical systems (MEMS) [118, 119]. The formation of LIPSS is attributed to interference between the incident beam and scattered beam parallel to the substrate, and the corresponding period and orientation of ripples can be determined by laser beam wavelength and polarization as described by classic theories [120-123]. In addition, laser treatment can modify the phase composition and chemical state of the irradiated surface [124-126], via surface oxidation and intermetallic formation, accompanying the modification of surface properties. The surface treatments have been carried out previously on bulk metallic materials to achieve better mechanical properties such as hardness [127], fatigue [128], wear [129], and corrosion resistance. The mechanical property enhancement is attributed to solid solutions and alloy precipitates induced by laser treatment. The advantage of this technique is the ability to improve surface mechanical

properties while confining the modification of both microstructure and chemical composition to a very shallow depth from the surface within a very short interaction time.

For metallic multilayer thin films, few studies have been done on laser treatment. However, laser-treated multilayer films could have broad potential applications. First, laser treatment on multilayer thin films can be a convenient and quick approach to form alloy compared to thermal annealing. Second, laser-induced surface strengthening, protective coating, and texturing could be achieved with suitable material selection and precise laser controlling, increasing the corresponding potential applications of multilayer thin films in aerospace/armor systems, biomedical devices, and photovoltaic/ semiconductor industry.

In this work, Ti/Ni multilayer thin films were selected as a model system to perform laser treatment due to their advanced functional properties (e.g. optical and magnetic) as well as mechanical properties. Laser treatment can potentially improve the wear and corrosion resistance and biocompatibility of Ti/Ni multilayer films by forming a Ti-Ni alloy coating on the surface, increasing the probability of applying the Ti/Ni multilayer system for medical applications.

6.2 EXPERIMENTAL DETAILS

In this study, the Ti/Ni multilayer thin films were prepared using the same procedure as introduce in Chapter 3. In this work, films with two different individual layer thicknesses, - 20 nm and 50 nm, and two different total film thicknesses, - 1 μm and 500 nm, were deposited. Thus a total of 4 layer thickness/film thickness combinations were studied: 20 nm/500 nm, 20 nm/1 μm, 50 nm/500 nm, and 50 nm/1 μm.

The aforedeposited Ti/Ni multilayer thin films were subsequently treated by a Nd:YAG pulse laser (Leopard SS, Continuum, Santa Clara CA) with pulse duration of 120 picosecond (ps) and wavelength of 1064 nm. Fig. 6.1 shows the schematic of the experimental setup for the laser treatment. The Nd:YAG laser has a fixed pulse energy of 260 mJ. The combination of a half-wave plate and a polarizer was used as an optical attenuator to adjust the pulse-energy according to the following relationship:

$$\begin{cases} E_1 = E_0 \\ \gamma = \beta \end{cases} \tag{6.1}$$

$$E_2 = E_1 \cos(\beta + \gamma + \alpha) = E_0 \cos(2\beta + \alpha) \tag{6.2}$$

where E_0, E_1, E_2 are the light vector magnitudes from the laser, and after passing through the half-wave plate and polarizer, respectively, α is the angle between the polarization direction of the laser beam and the polarizer (which is assumed to be vertical), β and γ are the entering and exiting angles of the laser beam relative to the fast axis of the half-wave plate. During experiment, β was adjusted by rotating the half-wave plate to vary the deposited pulse energy which was measured by a power-meter (Ophir, 10A-V2, MA) placed just before the sample surface. In this

work, pulse-energy dependency was studied with a wide energy range from 25 mJ to 150 mJ. A plano-convex lens was used to focus the original laser beam of 10 mm diameter down to a spot with 3 mm diameter. The incident laser beam was directed on the Ti/Ni multilayer surface at an incident angle of 67.5 ° due to the high reflectivity of sample surface. Each treatment consists of 50 successive pulses with a typical pulse repetition rate of 5 Hz. A three-axis translational stage was used to precisely position the laser spot at a desired location on the sample.

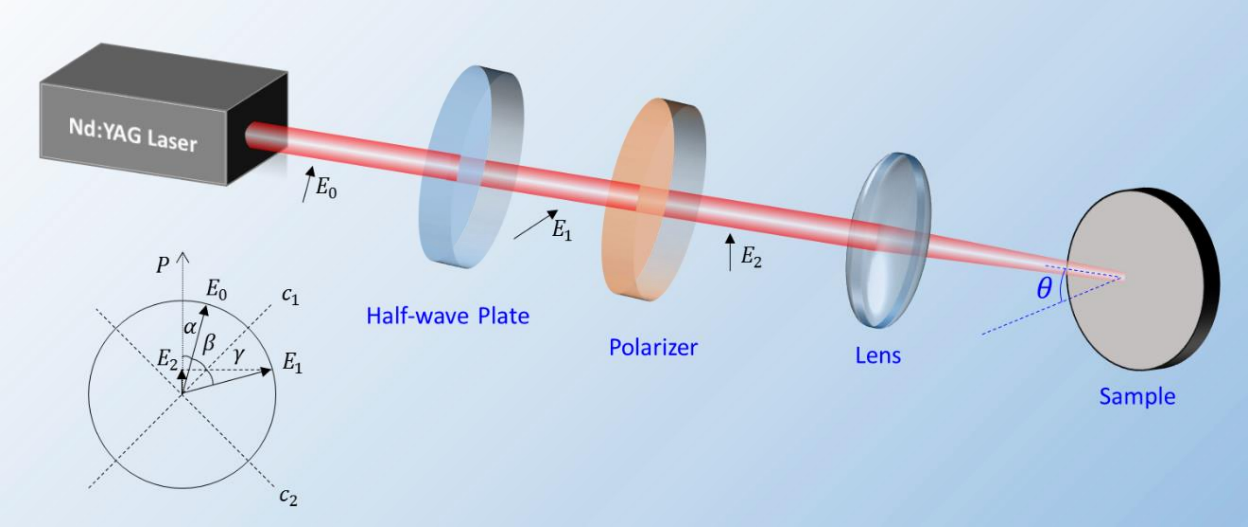

Figure 6.1: Schematic of experimental setup for laser treatment on Ti/Ni multilayer thin films. A Nd: YAG laser is used to generate laser beam. Half-wave plate and polarizer are used to adjust the laser energy. The relation of pulse energies after each optics is shown in the left bottom corner.

For microstructure characterization, SEM was used to examine the evolution of both cross-section and surface morphologies, and XRD with Cu K α radiation source was used to study the crystallinity of the non-treated and laser-treated films. Fine scanning was performed with a step of

0.06 %s in order to capture detailed modifications of phase composition and chemical state after irradiation. AFM was used to further examine the surface features for laser-treated samples. For mechanical testing, nanoindentation was carried out with a Berkovich indenter tip for both non-treated and laser-treated Ti/Ni multilayer films. Before and after indentation, an in-situ SPM imaging option was used to scan the surface and ascertain the indent quality. For rough surfaces observed after high pulse-energy treatment, manual polishing was carried out before nanoindentation by using 0.3 μm alumina slurry for about 30 seconds to remove a few nanometers of the surface roughness.

6.3 LASER ENERGY EFFECT ON MICROSTRUCTURAL EVOLUTION AND SURFACE STRENGTHENING

In this part, Ti/Ni multilayer 20 nm/500 nm is used to study the microstructural evolution and surface mechanical properties modification with respect to the laser pulse energy.

6.3.1 Microstructure Characterization

Cross-section morphology can provide direct evidence of microstructure evolution after laser treatment. Fig. 6.2 shows the cross-section SEM images for both non-treated and laser-treated Ti/Ni multilayer films by a wide range of pulse-energy from 25 mJ to 125 mJ. For non-treated sample as shown in Fig. 6.2(a), well-defined Ti and Ni layers are clearly displayed with dark layer being Ti and bright layer being Ni. In samples treated with pulse-energy of 50 mJ in Fig. 6.2(b), a thin intermixed layer is formed on the surface with thickness around 50 nm and the remaining thickness maintains the alternating Ti/Ni multilayered structure down to the Si substrate. The same intermixed layer is also observed in the 75 mJ case, but with thicker intermixed layer around 100 nm as shown in Fig. 6.2(c). This partially intermixed structure appears uniform in the whole treated area. A totally different phenomenon is shown in the 100 mJ case, with a fully intermixed structure in the center area of the irradiated spot as in Fig. 6.2(e) while a partially intermixed structure is observed in the peripheral area as shown in Fig. 6.2(f). This non-uniform cross-sectional morphology can also be detected in samples treated with 125 mJ, as shown in Fig. 6.2(g-i), corresponding to the cross-section morphologies in the treated center, and 0.5 mm and 1 mm on the side. The spatial dependence after high pulse-energy treatment is attributed to the Gaussian distribution of the laser beam profile. The formation of the intermixed layer is due to thermal

diffusion during treatment. Laser-illumination induced ultra-high temperature on the surface and the majority of the thermal energy is confined within a shallow depth from the surface (or heat affected zone) to form an intermixed region. After the high pulse-energy treatment, the intermixed layer can expand, producing bubbles and voids. For the remaining thickness of the Ti/Ni multilayer, the microstructure appears similar to that in the non-treated sample, indicating no obvious diffusion along Ti/Ni interfaces, although the heat diffuses through the whole film. Note that the total film thickness is less than 500 nm after high pulse-energy treatment, as the film is partially ablated with successive pulses.

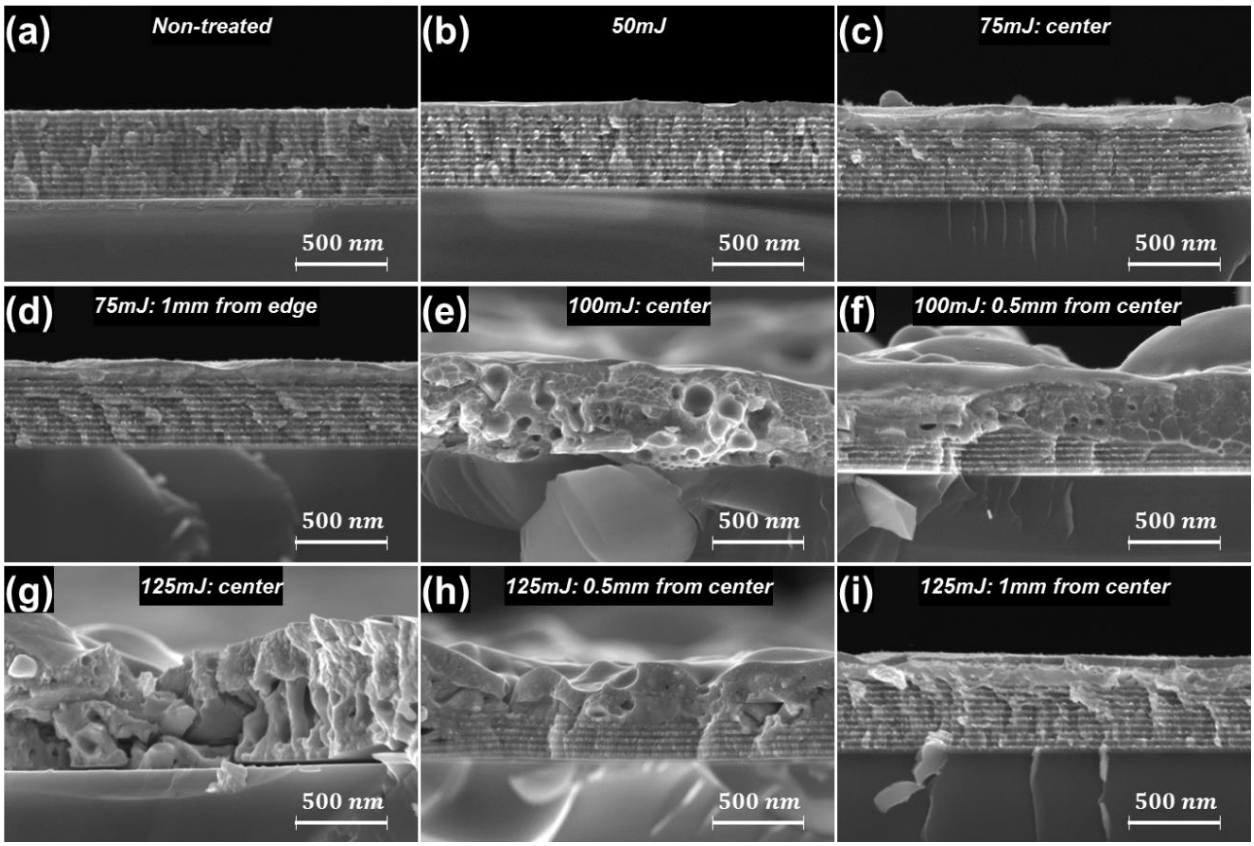

Figure 6.2: SEM images of cross-section morphologies for (a) non-treated and laser-treated Ti/Ni multilayer thin films (20 nm/500 nm case) by different pulse-energies (b) 50 mJ, (c ~ d) 75 mJ, (e ~ f) 100 mJ and (g ~ i) 125 mJ.

Fig. 6.3 shows the XRD spectra for both non-treated and laser-treated samples with pulse-energy from 50 to 150 mJ. In the non-treated case, two well-defined peaks at 35.7 °and 44.3 °are detected, corresponding to a HCP structure for Ti (100) and a FCC structure for Ni (111) respectively. The large intensity difference between the Ni (111) and Ti (100) peaks indicates that the Ni layer is more crystalline and textured than the Ti layer. In the 50 mJ case, there is no obvious difference from the non-treated one, showing neither peak weakness nor new peak formation, indicating no Ti-Ni intermetallic formation in the thin intermixed layer formed in this sample. In the 75 mJ case,

Ti-Ni intermetallic peaks start to appear, such as TiNi (011) and NiTi(002)/Ni_3Ti(004), indicating that higher pulse-energy promotes the formation of Ti-Ni intermetallic. These Ti-Ni intermetallic peaks become more intense in samples after higher pulse-energy treatment, and meanwhile more Ti-Ni intermetallic phases can be detected such as the Ni_4Ti_3 as shown in the 100 and 125 mJ cases. An extreme situation is observed in the 150 mJ case, with only NiTi peaks detected. These XRD results show that different types of intermetallic phases can be detected after laser treatment, such as NiTi, Ni_4Ti_3 and Ni_2Ti. In addition to the sufficient pulse-energy, the amount of diffused element plays an important role as well. Ni material has higher mobility than Ti, leading to higher fraction of Ni atoms in the locally intermixed area, where Ni_4Ti_3 and Ni_2Ti might be preferred. A fully Ti-Ni intermixed region might promote NiTi formation. In a previous reported work, only NiTi intermetallic is detected in laser-treated Ti/Ni multilayer samples with layer thickness of 16 nm.

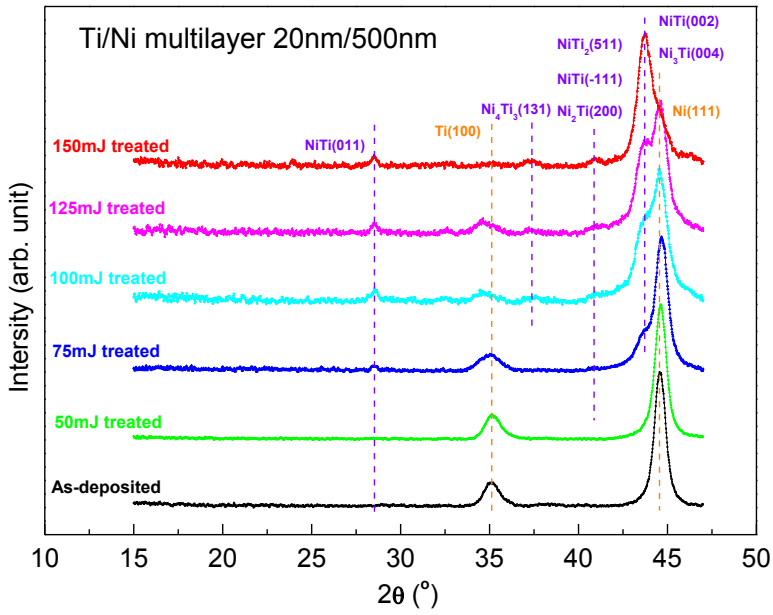

Figure 6.3: XRD patterns for non-treated and laser-treated Ti/Ni multilayer thin films by different pulse-energies from 25 ~ 125 mJ. Ti-Ni intermetallic phases could be first detected with pulse energy 75 mJ.

Surface morphology can provide complementary information about pulse-energy dependent microstructure evolution. Fig. 6.4 shows the surface SEM images for non-treated and laser-treated Ti/Ni multilayer films with different pulse energies. The non-treated sample displays a smooth surface, covered by uniform grains with average size around 25 nm as shown in Fig. 6.4(a). In the 50 mJ case as shown in Fig. 6.4(b), some area displays vertical ripples structure while a relatively smooth surface still maintained. In the 75 mJ case as shown in Fig. 6.4(c), a cross-hatched pattern is observed in some local area. The detailed ripple topographies for Fig. 6.4(b) and (c) are examined by using AFM as shown in Fig. 6.5(a) and (b), and the corresponding depth profiles along the lines in AFM images are shown in Fig. 6.5(c) and (d). In 50 mJ case, the vertical ripple structure has a period on the order of 250 nm and a height on the order of a few tens of nm. In 75

mJ case, the cross-hatched pattern has a period on the order of 700 nm and a height on the order of 100 nm. The formation of these periodic structures may be attributed to interference between the incident beam and scattered beam parallel to the substrate as previously reported [120-123]. After treatment with high pulse-energy, a melted surface with high roughness can be observed together with bubbles, voids and cracks as shown in the 100 mJ case in Fig. 6.4(d).

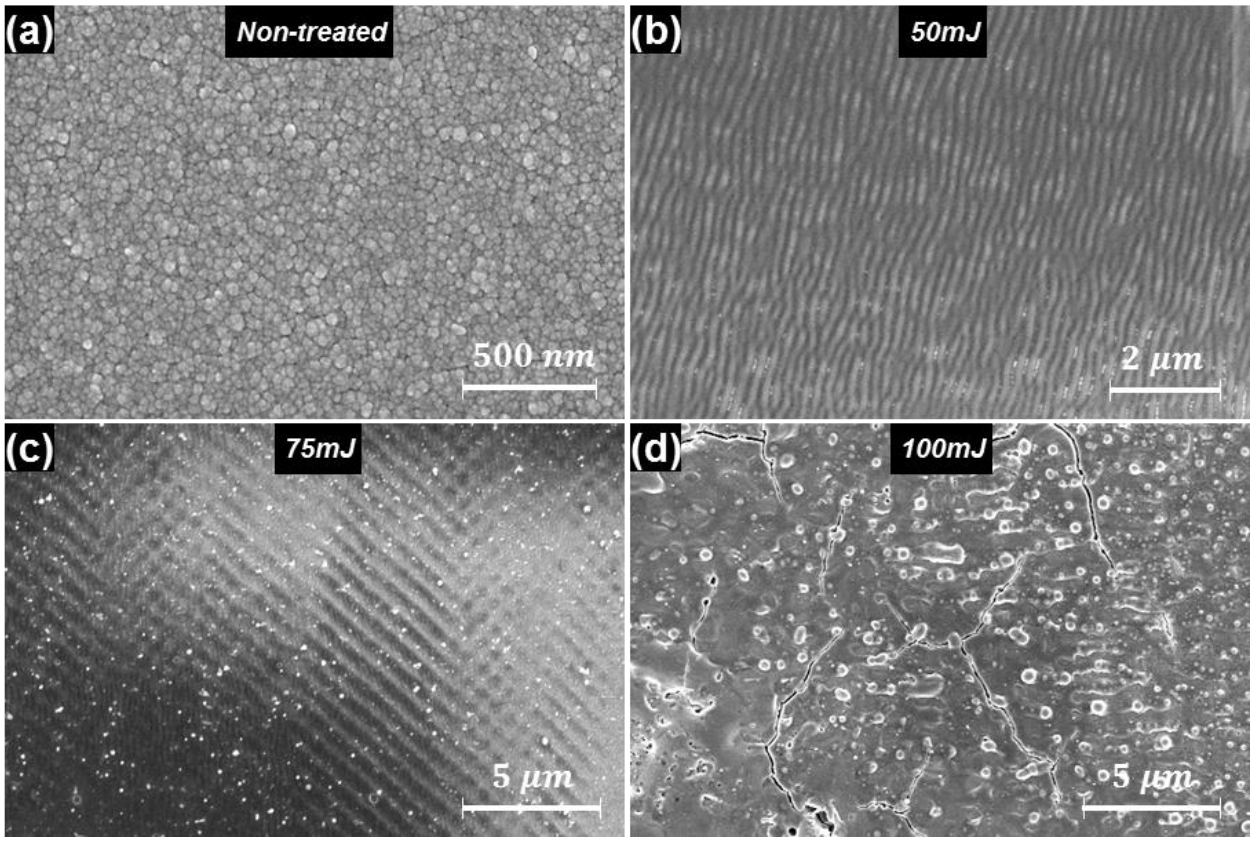

Figure 6.4: SEM images of surface morphologies for (a) non-treated and laser-treated Ti/Ni multilayer thin films by different pulse-energies: (b) 50 mJ, (c) 75 mJ, and (d) 100 mJ.

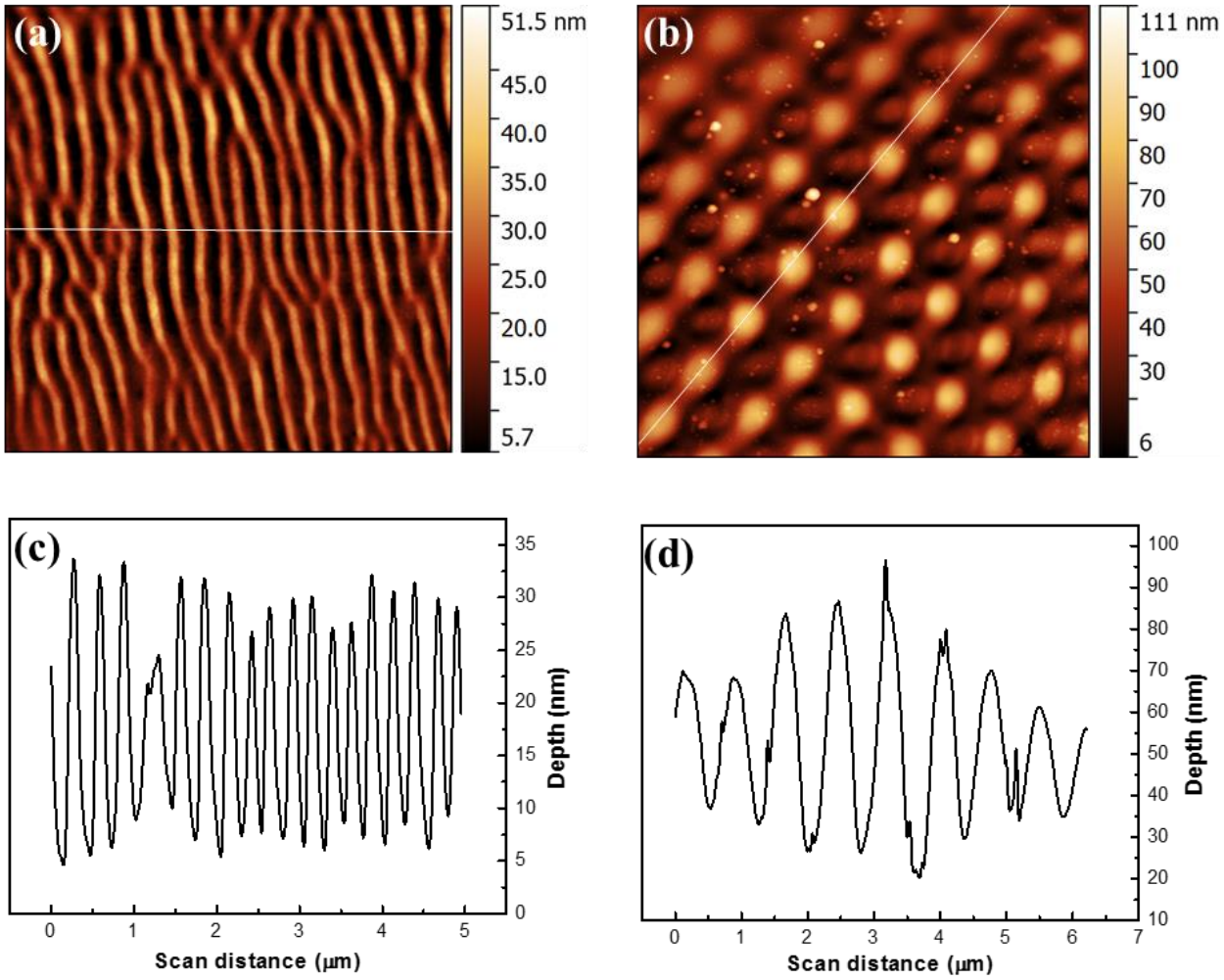

Figure 6.5: AFM images of surface morphologies ($5\ \mu m \times 5\ \mu m$) for laser-treated Ti/Ni multilayer thin films by (a) 50 mJ and (b) 75 mJ as well as the corresponding depth profiles (c) and (d) along the lines in AFM images.

Combining the SEM images and XRD spectra of both non-treated and laser-treated Ti/Ni multilayer films, the microstructure evolution can be schematically described by Fig. 6.6. During laser treatment, ultrahigh temperature is generated on the irradiated surface and the resulting thermal energy diffuses through the film. With successive pulses, more and more energy is built

up within the heat affected zone near surface area, promoting complex thermal activities and chemical reactions, such as interdiffusion, intermixing, oxidation, alloy solidification, and melting. Instead of the multilayered structure in the non-treated sample, an intermixed layer is formed to overlay the Ti/Ni multilayer film. With the increase of pulse-energy, the intermixed layer becomes thicker, and eventually a fully intermixed structure is formed. Meanwhile, the surface morphology changes from a smooth grain surface to a periodic surface, and then to a rough melted surface. High pulse-energy can lead to thermal expansion, producing a large number of voids and bubbles on the surface. Additionally, high thermal stress is generated at Ti-Ni interfaces due to the different coefficients of thermal expansion for Ti and Ni, resulting in micro-cracks in the film.

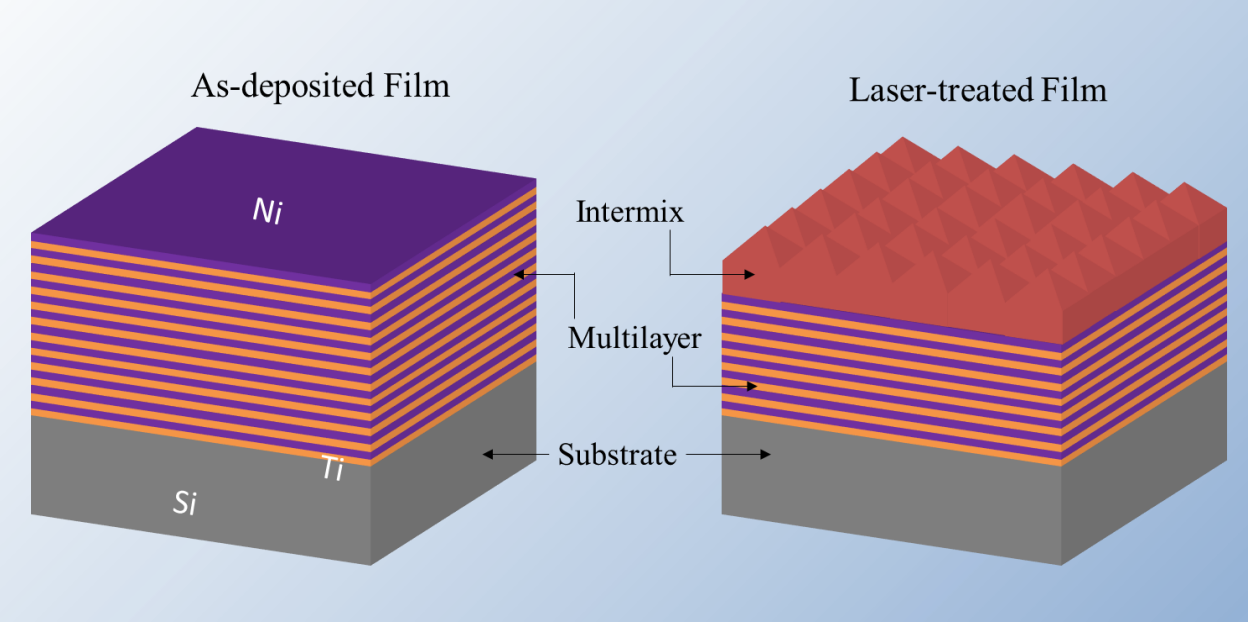

Figure 6.6: Schematic of microstructural evolution after laser treatment on as-deposited Ti/Ni thin multilayer. Intermixed layer is formed on the top of multilayered structure, and periodic surface structure is observed.

6.3.2 Hardness Characterization

Nanoindentation was applied to obtain the hardness for Ti/Ni multilayer films. Fig. 6.7 shows the hardness as a function of contact depth for both non-treated and laser-treated samples with pulse-energy from 25 to 100 mJ, as well as the polished samples after high pulse-energy treatment. The total film thickness is around 500 nm, and the maximum contact depth is controlled around 30% of the film thickness, ~150 nm, in order to minimize the substrate effect. In the non-treated case as in Fig. 6.7(a), a uniform hardness distribution is observed with contact depth from 70 to 140 nm. The hardness distribution can be significantly susceptible to surface quality, and the consistency shown in this case is due to the homogeneous and smooth surface of the as-deposited film. Similar hardness distribution is observed in the 25 mJ case as shown in Fig. 6.7(b) and the 50 mJ case shown in Fig. 6.7(c), since the relatively smooth surface can be maintained after low pulse-energy treatment. In the 75 mJ case shown in Fig. 6.7(d), the hardness data points are scattered within the contact depth range from 80 nm to 160 nm, due to the cross-hatched pattern induced slightly rougher surface. In higher pulse-energy case, such as the 100 mJ in Fig. 6.7(e), the rough melted surface, covered with voids, bubbles and cracks, leads to even more scattered data. In order to reduce the surface roughness effect, mechanical polishing was carried out on samples treated after high pulse-energies such as 75 mJ and 100 mJ. Manual polishing was carefully performed by using 0.3 μm alumina for about 30 seconds to remove a few nanometers on the surface. Fig. 6.7(f) shows the hardness distribution for the polished samples with contact depth from 80 nm to 160 nm. By comparison, more uniform hardness distribution can be observed after polishing.

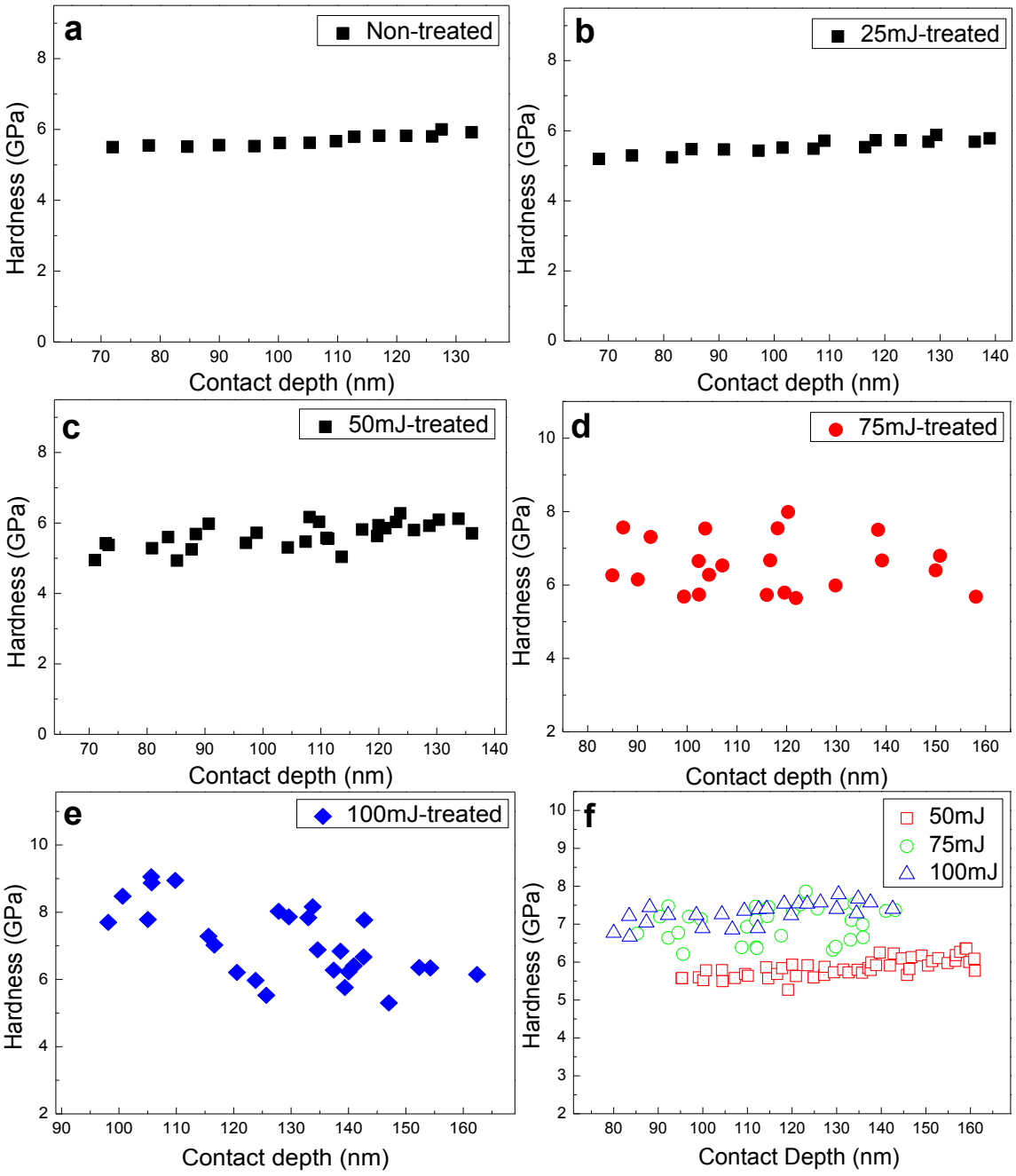

Figure 6.7: Hardness distribution with contact depth for both (a) non-treated and laser-treated Ti/Ni multilayer thin films by different pulse-energies from (b ~ e) 25 ~ 100 mJ, as well as for (f) polished samples treated by higher pulse-energies from 50 ~ 100 mJ.

Fig. 6.8 shows the average hardness as a function of pulse-energy for both unpolished and polished samples. For unpolished samples, almost no hardness change is observed after low pulse-energy treatment, such as 25 mJ and 50 mJ. Note that a 50 nm intermixed layer is formed in the 50 mJ case, indicating either the intermixed layer has the similar hardness as the multilayer film, or the intermixed layer is too thin to contribute in the overall hardness. With high pulse-energy treatment, an obvious surface strengthening is achieved, and the strengthening is attributed to precipitation of the intermetallics. Note that a 100 nm intermixed layer is formed in the 75 mJ case, and high hardness maintains with indentation depth as large as 160 nm, indicating the multilayers next to the top intermixed layer could be probably strengthened as well after high pulse-energy treatment. With even higher pulse-energy, more intermetallic is formed and as a result more strengthening is achieved. For polished samples, the similar strengthening trend is observed with increasing pulse-energy. Compared to unpolished samples, the polished samples have higher hardness in general, possibly due to come contribution of polishing induced high initial dislocation density after cold working.

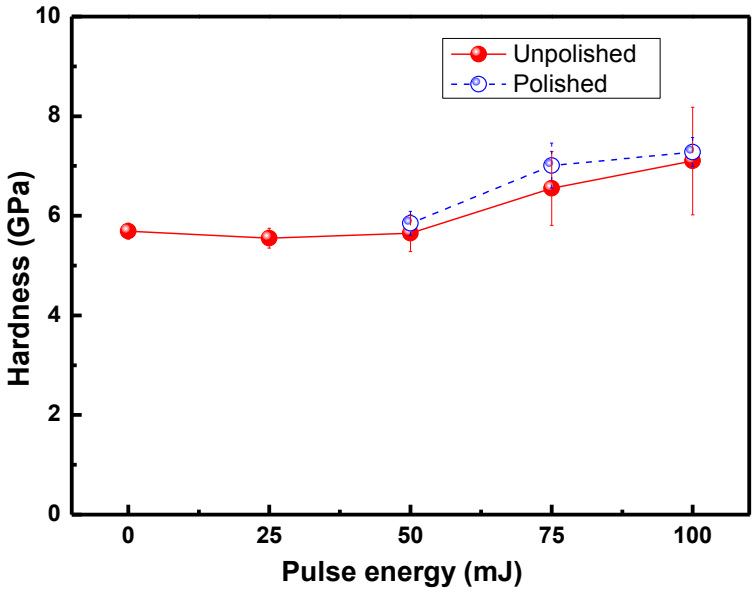

Figure 6.8: Average hardness as a function of laser pulse energy for both unpolished and polished Ti/Ni multilayer thin films. Obvious strengthening could be first achieved after treatment with pulse energy 75 mJ.

6.4 THICKNESS EFFECT ON MICROSTRUCTURAL EVOLUTION AND SURFACE STRENGTHENING: LAYER THICKNESS AND FILM THICKNESS

6.4.1 Microstructure Characterization

6.4.1.1 Layer Thickness Effect

Previous study on the 20 nm (layer thickness)/500 nm (film thickness) Ti/Ni multilayer thin films showed that pulse-energy can have significant effect on the morphological evolution of laser treated multilayers [130]. With the increase of pulse-energy, the cross-section morphology changes from a multilayered structure to a partially intermixed structure, then to a fully intermixed structure, and the surface morphology changes from a homogeneous grain structure to non-uniform mixed surface structure with grains, ripples and lightly melted surface, then to a rough melted surface covered with voids, bubbles and cracks. In current work, the microstructural evolution on 50 nm/500 nm multilayers was further studied to investigate the layer thickness effect.

Fig. 6.9 shows the cross-section morphology evolution of laser-treated 500 nm thick films with $\lambda = 20$ nm and $\lambda = 50$ nm, respectively. After treatment with 50 mJ, a thin (~50 nm) and smooth intermixed layer was formed on the top of multilayered film in the 20 nm case, while a thick (~100 nm) and rough intermixed layer was observed in the 50 nm case. After treatment with 75 mJ, in the 20 nm case, the intermixed layer becomes thicker (~100 nm) and still uniformly overlays the multilayers while in the 50 nm case, non-uniform distribution was observed with fully intermixed structure in the center area and partially intermixed structure near the edge. The non-uniform

distribution could be observed in the 20 nm case as well, if the pulse-energy is increased to a higher level, e.g. 100 mJ and 125 mJ [130].

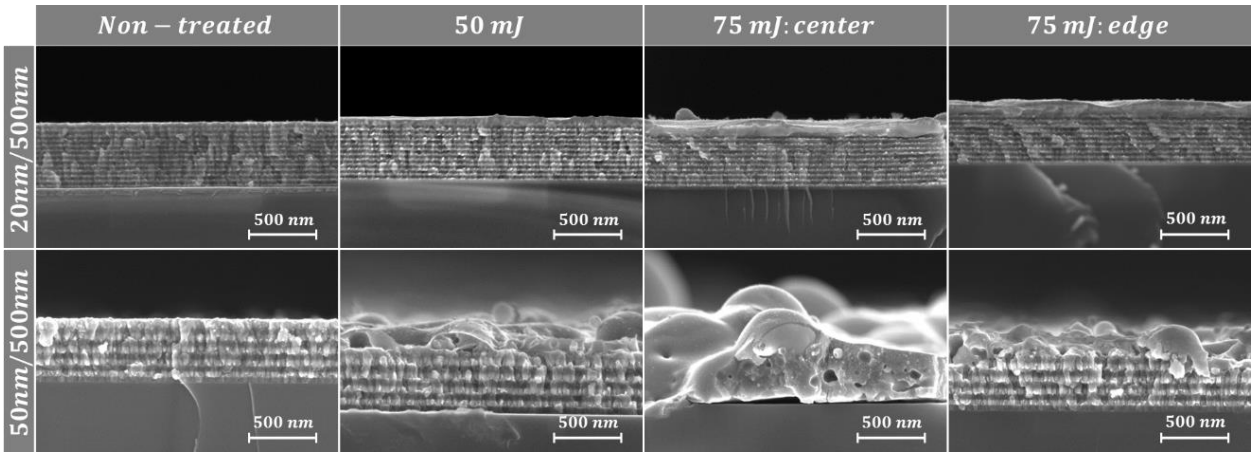

Figure 6.9: Cross-sectional SEM images of non-treated and laser-treated 500 nm thick Ti/Ni multilayer films with layer thickness of 20 nm and 50 nm, respectively. Uniform cross-section structure is observed in 20 nm case.

Fig. 6.10 shows the corresponding surface morphology evolution of the laser-treated 500 nm thick films with $\lambda = 20$ nm and $\lambda = 50$ nm. The as-deposited samples both show a smooth surface with homogeneous grain distribution and grain size around 25 nm. In the 20 nm case, vertical ripples were observed on top of the grain surface with a period on the order of 250 nm after treatment with 50 mJ, and 45 ° ripples with a period on the order of 700 nm were observed after treatment with 75 mJ. These LIPSS are indistinct and locally distributed on the surfaces, which remain smooth or relatively smooth after laser treatment. A rough melted surface structure was observed after treatment with 100 mJ pulse-energy. In the 50 nm case, neither vertical ripples nor 45 ° ripples

were observed after treatments with 50 mJ and 75 mJ. Instead, rough melted surfaces were formed. However, another type of vertical ripple structure with ripple width on the order of 100 nm was observed uniformly after treatment with 25 mJ. This new feature is likely a superposition between a LIPSS from the optical interference and a lightly melted surface. It is interesting to note that three different types of ripples were observed in the current work with the same laser beam parameters.

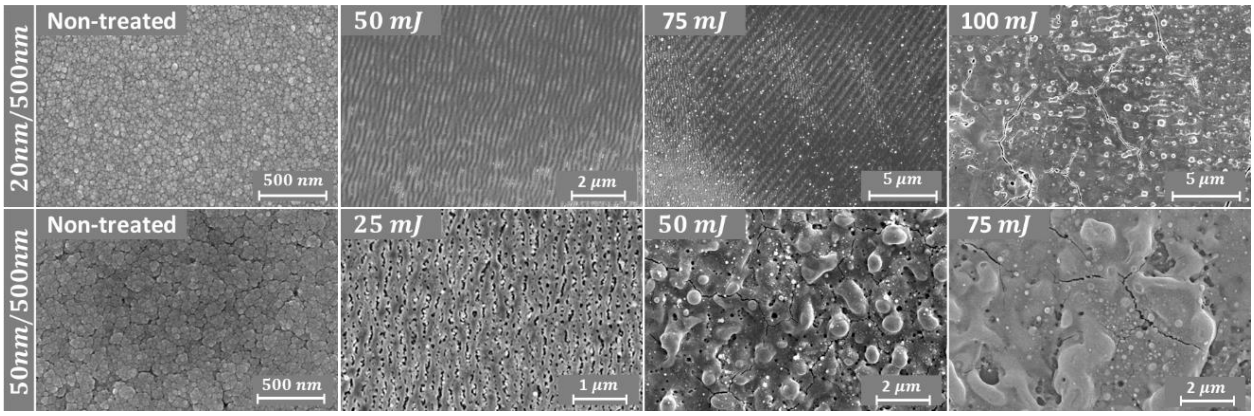

Figure 6.10: Surface SEM images of non-treated and laser-treated 500 nm thick Ti/Ni multilayer films with layer thickness of 20 nm and 50 nm, respectively. Smoother surface is generally observed in sample with thinner layer, that is, 20 nm case.

Both cross-section and surface SEM morphologies have demonstrated significant layer thickness effect on morphological evolution. Further investigation of layer thickness dependent phase composition and chemical state after laser treatment was carried out using XRD. Fig. 6.11 shows XRD patterns before and after laser treatment for the 500 nm thick films with $\lambda = 20$ nm and

$\lambda = 50$ nm, respectively. Both as-deposited films show similar crystallinity: HCP Ti (100) structure and FCC Ni (111) structure. After treatment with 50 mJ, a similar XRD pattern is displayed in the 20 nm case, indicating no obvious phase modification after laser treatment, while in the 50 nm case the Ti peak almost disappeared and a tiny Ti-Ni intermetallic peak $NiTi_2$ (400) is detected. The intermetallic peak becomes increasingly more intense after treatment with higher pulse-energies, and meanwhile more Ti-Ni intermetallic phases are detected. For the 20 nm case, the intermetallic peak was first detected after treatment with 75 mJ, which is higher than that in the 50 nm case. The intermetallic peaks also become more intense after treatment with higher pulse-energy. For both the 20 nm and 50 nm cases, the Ti-Ni intermetallic evolution behavior is similar: intermetallic phase initially precipitates with a certain pulse-energy, more precipitation with higher pulse-energy, and then more intermetallic phases were formed. However, for the two different λ, the Ti-Ni intermetallic phases formed are different, indicating the individual layer thickness plays an important role in the intermetallic formation. When the individual layer is thick, diffused Ni atoms could be surrounded by more Ti atoms, leading to the formation of intermetallic with higher Ti fraction, such as $NiTi_2$ in 50 nm case. When the individual layer is thin, full intermixing could occur, promoting the formation of NiTi and Ni_4Ti_3, as in the 20 nm case. Only a tiny NiTi intermetallic peak was detected in a previously reported work with individual layer thickness of 16 nm [126]. In addition, a TiO_2 phase can be detected only in the 50 nm case. This oxide peak appears after treatment with 75 mJ and becomes more intense after treatment with higher pulse energy.

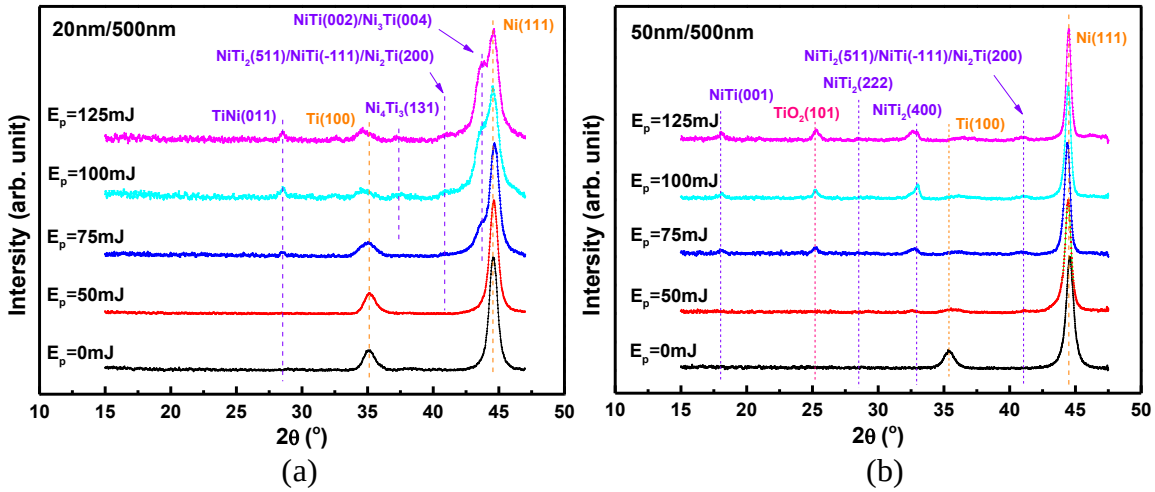

Figure 6.11: XRD patterns for non-treated and laser-treated 500 nm thick Ti/Ni multilayer films with layer thickness of 20 nm and 50 nm, respectively. In both figures, the symbol E_p refers to pulse-energy. Note the pulse energies required to achieve intermetallic phase are different in two cases.

6.4.1.2 Film Thickness Effect

In addition to individual layer thickness, total film thickness (h) can also play an important role in microstructure modification after laser treatment. In previous work, for example, laser-induced periodic surface structures were observed to have different periods on irradiated surfaces for samples with various total film thickness [130]. In this work, varying cross-section and surface morphologies have been observed in samples with different h. Fig. 6.12 shows the SEM images of morphologies after laser treatment with 50 mJ and 75 mJ on both 500 nm and 1 μm thick films with $\lambda = 20$ nm and $\lambda = 50$ nm. From examination of the cross-section morphology, the 1 μm film forms a thin and smooth intermixed structure from the top layers of the multilayer system, which is distributed uniformly across the irradiated surface. In comparison, the 500 nm film

develops a thick and rough intermixed layer. Furthermore, even thicker intermixing can be observed in samples with $\lambda = 50$ nm. The comparison of cross-sectional morphologies from all four cases indicates that more energy can be accumulated near surface with a larger λ / h ratio, which is also confirmed by the corresponding surface morphologies. With laser treatment after 75 mJ, for example, the 50 nm/500 nm films show a massive melted surface covered by bubbles, voids and cracks, the 20 nm/500 nm films display a mixture surface morphology with indistinct 45 ripples and local melting surface, while both 1 μm films exhibit a uniformly distributed cross-hatched pattern structure. In the current study, the cross-hatched periodic surface structure can be observed in the 1 μm films even after treatment with pulse-energy as high as 125 mJ, indicating a wide range pulse-energies could be adopted to achieve the periodic structure for thick films. In addition, in the 1 μm thick films, the individual layer thickness effect on the cross-section and surface morphologies is not as significant as in the 500 nm thick films. That is, for the 1 μm films, the uniformly distributed intermixed layer and distinct cross-hatched surface pattern can be observed in both 20 nm and 50 nm cases. Although not included here, the laser-treated 1 μm thick Ti/Ni multilayers showed very similar XRD spectra to non-treated samples, indicating the accumulated energy in the intermixed layer is probably not sufficient to introduce any crystallinity or chemical state modification regardless of pulse-energy and layer thickness studied here.

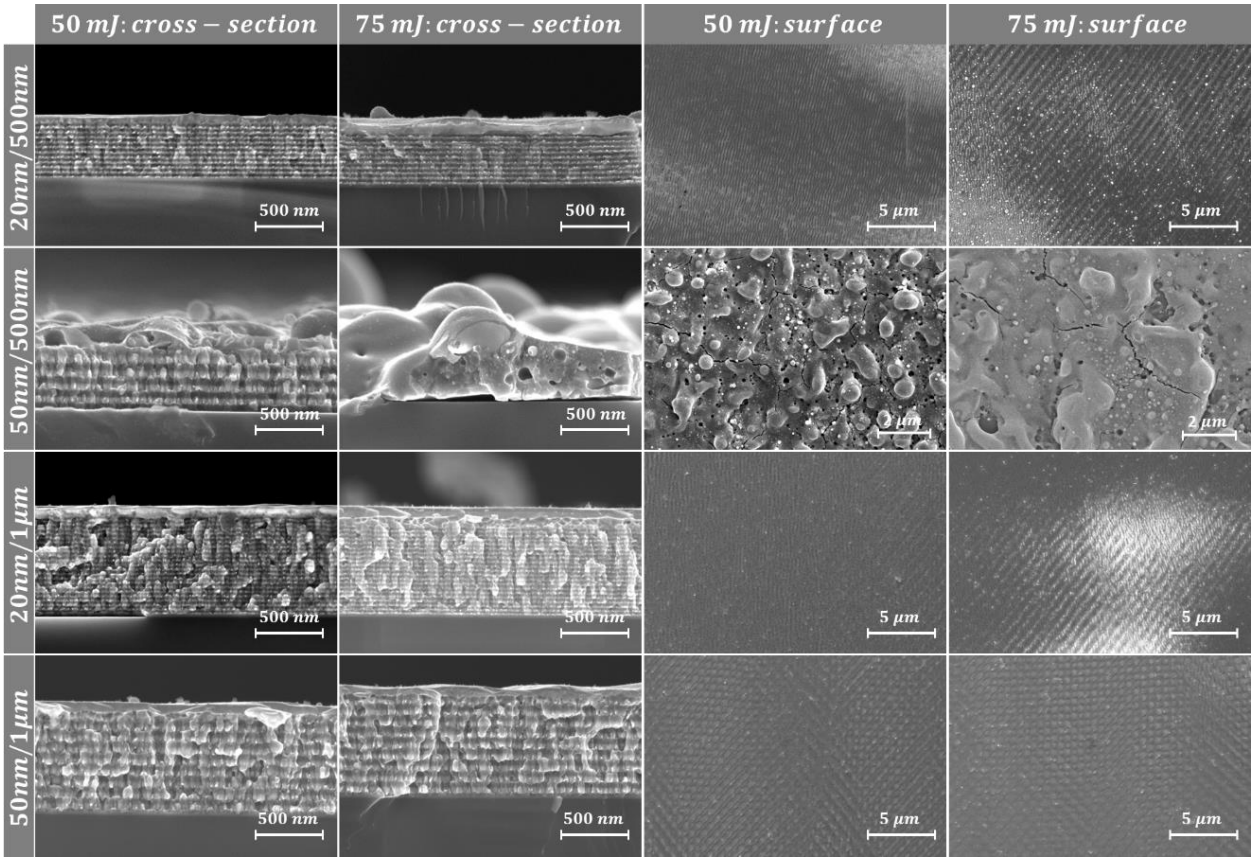

Figure 6.12: Cross-section and surface SEM morphologies for 50 mJ and 75 mJ treated 500 nm and 1 μm thick Ti/Ni multilayer films with layer thicknesses of 20 nm and 50 nm. Smooth surface and uniform layered cross-section can be observed in 1 μm film. In 500 nm film, rough surface and intermixed cross-section could be observed with thick layer, 50 nm here.

6.4.2 Hardness Characterization

Fig. 6.13 shows the hardness as a function of pulse-energy for all four sets of Ti/Ni multilayer thin films. The as-deposited Ti/Ni multilayers have hardness values around 5.8 GPa with $\lambda = 20$ nm and 5.4 GPa with $\lambda = 50$ nm. In the 20 nm/500 nm case, no obvious hardness change is observed

after laser treatment with 50 mJ, while significant hardening was achieved after higher pulse-energy treatment in both unpolished and polished samples as shown in Fig. 6.13(a). For example, an estimated 25% hardness increase is achieved after laser treatment with 100 mJ. In the 50 nm/500 nm case, the surface is too rough to apply indentation after treatment with high pulse-energy, so no unpolished hardness results were obtained for those samples. Careful manual polishing had to be carried out to achieve locally smooth locations for indentation. As shown in Fig. 6.13(b), polished samples display hardening after treatment with pulse-energy higher than 25 mJ, although the increase is a less significant (around 5% after 50 mJ treatment) than that in the 20 nm/500 nm case. For the 1 μm thick films, since a relatively smooth surface maintained after treatment, polishing is not necessary. A different hardness behavior is exhibited here, with almost no hardness change after laser treatment, regardless of pulse-energy (25 mJ ~ 100 mJ) and layer thickness (20 nm or 50 nm).

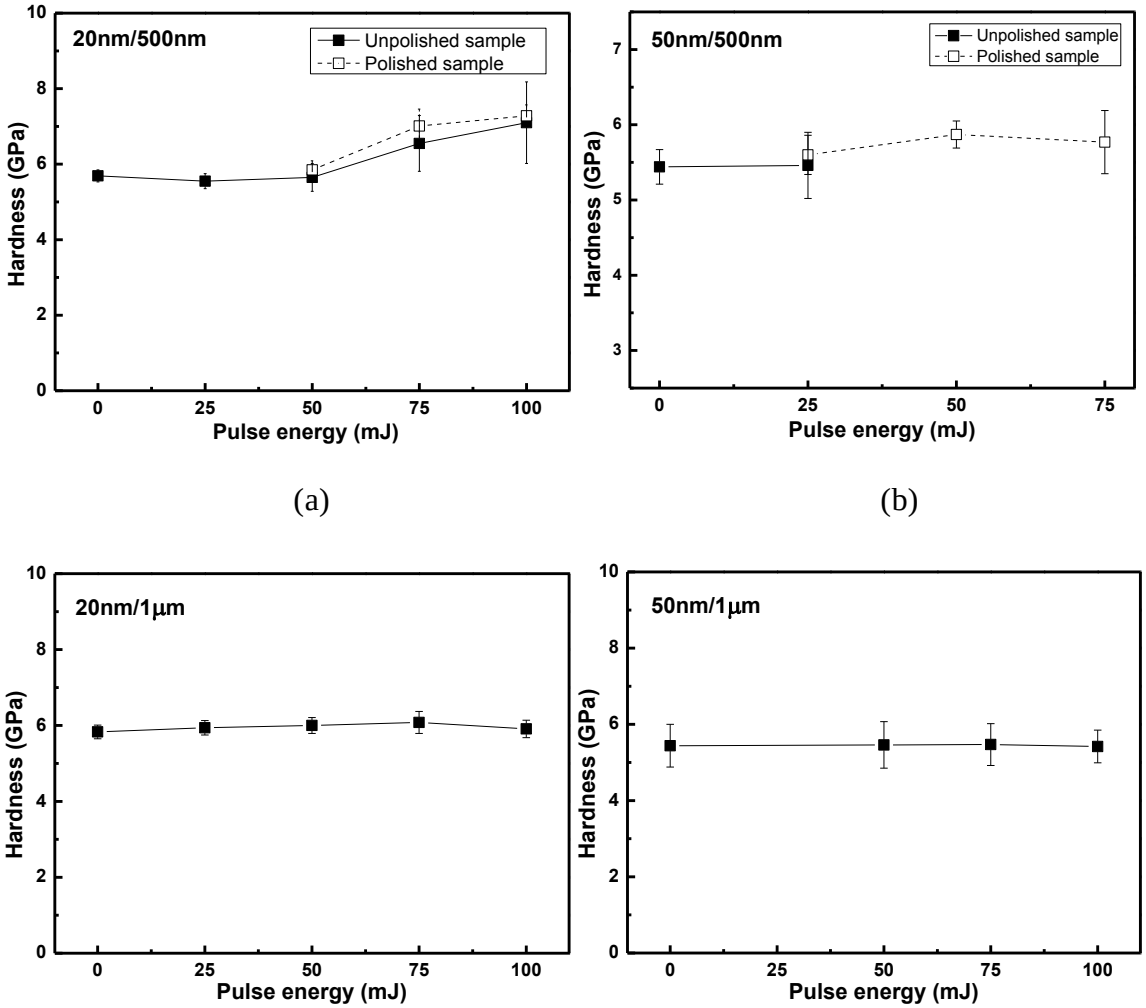

Figure 6.13: Hardness as a function of pulse energy for both non-treated and laser-treated Ti/Ni multilayer thin films in four different layer thickness/total film thickness combinations: (a) 20 nm/500 nm; (b) 50 nm/500 nm; (c) 20 nm/1 μm; and (d) 20 nm/1 μm. Laser treatment-induced surface strengthening can be only achieved in 500 nm total film thickness film.

6.4.3 Discussions

Significant thickness effects were observed on microstructural and mechanical properties for laser-treated Ti/Ni multilayer thin films. For example, surface strengthening is achieved in films with $h = 500$ nm, and more significant improvement occurred when further combined with $\lambda = 20$ nm. Uniform periodic surface structures are observed in films with $h = 1$ μm under a wide range of applied energy for both $\lambda = 20$ nm and $\lambda = 50$ nm. Oxidation is detected in 50 nm/500 nm. All these features - surface strengthening, LIPSS, and oxide layer formation - have large potential applications in various fields, and our current study here has demonstrated that each individual surface phenomena can be uniquely achieved through precise control of the laser treatment parameters and design of the material system.

The observed layer thickness and film thickness effects on microstructure and hardness likely result from their effects on thermal energy distribution in the multilayers. After a single pulse, ultrahigh temperature is generated on the irradiated surface, and the resulting thermal wave propagates toward the substrate, while the majority of the thermal energy is still confined near the surface region. With successive pulses, energy continues to accumulate in this area, promoting the formation of an intermixed layer. Meanwhile, for multilayers, interface reactions play an important role in thermal energy dissipation via interdiffusion, intermixing and intermetallic formation[124, 131]. Films with thin layers and a larger number of interfaces dissipate more energy, resulting in less energy accumulated in the intermixed region. For thick films, the longer heat conduction distance and increased number of interfaces lead to even less energy near the surface. Consequently, tailoring the thickness of metallic multilayer thin films can be a powerful means in the functionalization of laser-treated material systems in desired applications.

Applying these energy distribution assumptions, we first discuss the intermixed layer formation and the surface strengthening of laser-treated multilayers. For the 1 μm thick films, less energy is accumulated near the surface, resulting in the formation of a smooth, thin intermixed layer. For the 500 nm thick films, the intermixed layer is thicker due to more energy near the surface, which also promotes the formation of intermetallics. The precipitation of intermetallics is the main factor for improving surface strength, but also requires critical energy to initiate. There are more interfaces in films with $\lambda = 20$ nm, and more energy is absorbed along the interfaces, leading to less accumulated energy. As a result, higher pulse-energy is required to initiate the intermetallic formation, when compared to the 50 nm case. That is why the intermetallic appears after laser treatment with 75 mJ in the 20 nm/500 nm multilayers, while 50 mJ is required in the 50 nm/500 nm multilayers. More strengthening is observed in the 20 nm case, due to more energy absorption promoting intermetallic formation.

Next, we discuss the surface morphology in laser-treated multilayers. Available literature attributed the periodic surface structure to the interference between the incident beam and the scattered beam on the sample surface [122]. The competition between this optical interference and the net thermal energy seems to dominate the formation of the LIPSS or the melted surface. For 1 μm films, less energy remains on the surface, promoting LIPSS formation for a wide range of pulse-energies. In contrast, for 500 nm films, there is more energy and higher temperature on the surface, so a rough melted morphology is more likely. Low thermal energy on the surface could be the key to form LIPSS, and it is well accepted that the period Δ and orientation of the ripples depend on the wavelength Λ, the incident angle θ and the polarization of laser beam[114]. For

example, after p-polarized laser beam treatment, ripple structure with orientation parallel to polarization (vertical in current case) can be observed with a period calculated by $\Delta = \frac{\Lambda}{\cos\theta}$. However, none of the ripples found in this work agree with the prediction from the classic theory, indicating the properties of the multilayer films play a role in the LIPSS formation in addition to the properties of the incident laser beam. A similar phenomenon was also observed in other works related to laser-treated multilayer films [126], and further research into LIPSS on multilayers is required.

The surface oxidation observed in the 50nm/500nm films is likely from (1) surface segregation of Ti and formation of TiO2 due to its affinity to oxygen, and (2) laser-induced ablation of the Ni layer and thermal driven Ni atomic diffusions. The TiO2 phase was detected only in the 50 nm/500 nm case after treatment with 75 mJ. In the 20 nm/500 nm case, most of the Ti material likely reacts with Ni to form the Ti-Ni alloy before exposure on the surface. In the 1 μm films, the accumulated thermal energy on the surface of film is too low and as a result, less Ni material is ablated and diffused, resulting in less Ti exposure.

6.5 CONCLUSION

In this study, a ps pulse laser was utilized to treat Ti/Ni multilayer films. Detailed microstructural evolution and surface strengthening was investigated under a wide range of pulse-energy treatment from 25 to 150 mJ. With increasing pulse-energy, the surface morphology was observed to change from homogeneous grain structure to periodic surface structure, then to a rough melted surface covered with voids, bubbles and cracks. The corresponding cross-sectional morphology evolves from a layered structure to a partially intermixed structure, then to a fully intermixed structure. With sufficient pulse-energy, intermetallic phases were observed to form and the precipitation of the intermetallics can lead to surface strengthening.

Four layer thickness/film thickness combinations were studied, and it turns out that both film thickness and layer thickness play an important role in microstructural and mechanical properties of laser-treated Ti/Ni multilayer thin films. For films with smaller layer thickness, the increased number of interfaces can dissipate more thermal energy, resulting in less energy confined in the intermixed layer. As total film thickness increases, the thermal wave needs to propagate a longer distance and travel through more interfaces, resulting in even less thermal energy confined in the intermixed layer. The main findings can be summarized as follows:

(1) For thick films, distinct cross-hatched patterns were observed on the surface and a thin, smooth intermixed layer uniformly overlaid the multilayers under a wide range of pulse-energy treatments.

(2) For thin films, an indistinct ripple structure on the surface and uniform intermixing on the

cross-section were observed after low pulse-energy treatment, while a massive melting surface and rough, non-uniform intermixing cross-section were observed after high pulse-energy treatment.

(3) Surface morphology results from the competition between optical interference and thermal energy. Periodic surface structures can be observed in thick films due to less energy accumulated on the surface, as well as in thin films with low pulse-energy, while melted surfaces were observed on the surface in thin films with high pulse-energy, especially for films with thick layers.

(4) Surface strengthening occurs due to the precipitation of Ti-Ni intermetallics. Without intermetallic formation in thick films, no obvious hardness change is achieved even with the intermixed layer. An obvious strengthening is achieved in thin films, and a more significant strengthening is observed in films with thin layers due to more intermetallic precipitates.

(5) Formation of the intermetallic requires a critical energy. In thick films, long heat conduction distance and a large number of interfaces lead to insufficient energy near the surface to initiate intermetallic formation. In thin films, for a given layer thickness, a critical pulse-energy is required to introduce the intermetallic phase and subsequent strengthening.

Chapter 7. FINAL REMARKS AND FUTURE PERSPECTIVES

7.1 FINAL REMARKS

In the last two decades, more and more nanostructured materials have been reported to exhibit ultra-strength, such as nanocrystalline materials, nanopillars, nanowires, nanoparticles, multilayer and nanotwinned material. Although most of nanostructured materials can be routinely synthesized nowadays, there are still some challenges for ultra-strength materials. One of the most important challenges is how to fully understand the mechanisms of deformation behavior and material strength. In this work, systematical studies on Ti/Ni multilayer thin films have been carried out to understand the coupled size effect and thermal effect on strengthening mechanism for metallic multilayered thin film material. Specifically, in this dissertation, the size effect comes from the individual layer thickness and total film thickness, and the thermal effect from post deposition annealing, in-situ high temperature deposition, and localized surface annealing by laser irradiation.

In as-deposited multilayer thin films, strong size effect and orientation effect are observed on the deformation behavior and strengthening mechanisms. An obvious strengthening is obtained with the decrease of layer thickness due to the dislocation mediated deformation behavior, such as dislocation pile up along the interfaces and single dislocation bowing within interfaces. A softening is followed with further reduced layer thickness due to the grain boundary mediated motions. Both surface indentation and cross-section indentation were applied to study the loading orientation effect on the size strengthening behavior. The size strengthening in surface indentation

is due to dislocation pile up along interfaces while that in cross-section indentation is due to single dislocation bowing between interfaces.

In annealed multilayer thin films, integrated effects of annealing temperature, layer thickness and loading orientation were observed on the mechanical strength and thermal stability. Obvious strengthening is observed for multilayer with thin layer after low-T annealing due to grain boundary relaxation strengthening mechanism, while higher temperature is required to activate this strengthening mechanism for multilayer with thick layer. Under the similar temperature level, further strengthening is observed for multilayer with thin layer due to a combined strengthening mechanism from solid solution strengthening from diffused atoms and precipitation strengthening from intermetallic. After high-T annealing, fully intermixed and completely alloyed structure is formed in multilayer with thin layer, and high hardness is obtained due to alloy formation, while dramatic softening is observed in multilayer with thick layer due to recrystallization and grain growth.

For substrate temperature study, significant texture strengthening is observed with the increase of substrate temperature. Preferred crystallography orientations and large columnar structure extending through layers contribute to the initial strengthening due to low substrate temperature deposition, and further strengthening is from solid solution strengthening and precipitation strengthening. After high substrate temperature, a columnar Ti-Ni alloying film is observed with disintegration of layered structure.

In laser treated multilayer thin films, laser energy was observed to play an important role in microstructural and mechanical properties modification, with the surface morphology changing from homogeneous grain structure to periodic surface structure, then to a rough melted surface covered with voids, bubbles and cracks, and the corresponding cross-sectional morphology from a layered structure to a partially intermixed structure, then to a fully intermixed structure. In addition, strong effect from both film thickness and layer thickness were observed. In the films with smaller layer thickness, the increased number of interfaces can dissipate more thermal energy, resulting in less energy confined in the intermixed layer. As total film thickness increases, the thermal wave needs to propagate a longer distance and travel through more interfaces, resulting in even less thermal energy confined in the intermixed layer.

7.2 FUTURE PERSPECTIVES

In as-deposited multilayer thin films, the softening with decreased layer thickness when the layer thickness is on the order of a few nanometers is still not fully understood. Two possible mechanisms were proposed in literature: one is dislocation crossing mechanism, and another one relates with grain boundary mediated motions. Both computational work and experimental work can help to understand this fundamental problem better. Molecular dynamics simulation could provide direct evidence of deformation behavior, however, the difficulty is to set up a polycrystalline multilayer thin film model with comparable size. High resolution TEM could be performed to capture detailed deformation before and after loading. In addition, nanoindentation

could be applied with different constant strain rate in order to obtain the activation volume, and thus to distinguish the dislocation and grain boundary mediated motions.

In annealed multilayer thin films, detailed study with grain boundary relaxation strengthening mechanism is still limited. The aforementioned MD simulation, TEM and nanoindentation testing could be applied to understand this relaxation process. For example, if the dominating deformation mechanism is grain boundary associated motion in as-deposited sample, after annealing, the dominating deformation mechanism switches to dislocation mediated motion due to grain boundary relaxation. Then, from nanoindentation results, the activation volume would display a significant change. From our work, grain boundary plays a very important role in the deformation behavior and strengthening mechanism in annealed multilayer thin films, however, very few studies have been done to study the detailed interface role during annealing.

In laser treated multilayer thin films, laser energy, film thickness and layer thickness have a significant effect on the microstructure evolution and surface strengthening, due to the thermal energy distribution in the film. Simulation work could provide detailed analysis of heat transfer and help understand these effects better. In addition, laser treated multilayer films could improve the surface mechanical properties, such as wear resistance, and as a result could have large potential application in micro scaled device to improve the life time. Nanoscratch testing could be applied to study the wear properties of this laser treated multilayer films.

In addition, other factors not considered here may be important in metallic multilayer systems, such as the residual stress in the layers. It is well known that residual stress plays an important role

in mechanical properties of a thin film such as film cracking due to tensile residual stress or film delamination due to compressive residual stress. The residual stress has a strong dependency on deposition method and deposition conditions. For example, Satomi et al. found that the stress in thin film varies from compressive to tensile, depending on the deposition rate and substrate temperature [132]. Chang et al. reported that the residual stress in sputtered Ti films decreases as the substrate temperature increases, in which the stress changes from tensile to compressive when the substrate temperature increases from 25 to 150 ℃ [133]. Furthermore, an obviously linear correlation was observed for both the elastic modulus and the hardness with respect to residual stress. It shows that the elastic modulus decreases 3.33% and the hardness decreases 4.15% as the residual stress increases 0.1 GPa [133]. Another method to reduce the residual stress in sputtered thin film is by stacking low and high material density layers of the same material [134]. In general, low density thin films deposited at high Ar pressure and low temperature have almost zero residual stress, but with poor electrical properties. Low Ar pressure results in compressive residual stress finally forming a dense tin film. The compressive stress build-up in a film can be reduced by modulating between compliant layer and dense layer. The residual stress was also studied in nanoscale twinned thin films. Zhang et al. found that the residual stress varies from tensile to compressive by changing the deposition conditions, while there is no obvious change in microstructure, including the average columnar grain size and the texture of the film. However, the hardness of the film changes with the residual stress, from 5.5 GPa of films with residual tension to 7 GPa of film with compressive residual stress [135]. Misra et al. studied the residual stress in polycrystalline Cu/Cr multilayer thin films [136], and they found that the growth stress in the Cr layers is the primary source of residual stress in Cu/Cr multilayers. With the small layer thickness, the stress in Cr film follows the stress generation model, such as the crystalline

coalescence mechanism, and with the large layer thickness, the residual stress is limited by the yield strength of the film, followed by Orowan model. Zhang and Misra studied the residual stress in copper/330 stainless steel multilayer thin films and found that both single layer and multilayer films exhibit high tensile residual stresses that increase with decreasing layer thickness, but are found to be lower than the yield strengths [137]. The difference is attributed to interface stress. Although there are some observations for multilayer system, systematic studies of residual stress effect are still limited, especially for coupled size and thermal effect. The residual stress of multilayer thin films can be investigated in the future from the potential perspective of coupled size and temperature effect.

APPENDIX. ELASTIC MODULUS OF TI/NI MULTILAYERS

A.1 NANOINDENTATION PROCEDURE

Nanoindentation testing has been applied in current work to obtain the mechanical properties of Ti/Ni multilayer thin films. In the aforementioned sections, the hardness data were analyzed to understand the deformation behaviors and strengthening mechanisms. In current section, the detailed nanoindentation procedure is first introduced, and then representative results are shown by using as-deposited Ti/Ni multilayer thin film with layer thickness 25 nm (25 nm case for short).

A typical force displacement curve is shown in Fig. A.1 after indentation with maximum force 6000 μN for 25 nm case. As mentioned previously, a trapezoidal loading is applied with a 10 s loading, 5 s hold at maximum load, and 10 s unloading. A continuous loading curve was observed for this layered structure without obvious pop-up. This could be probably due to similar mechanical properties of Ti and Ni layers. Using the standard Oliver and Pharr method, the hardness and reduced modulus were obtained: 5.93 GPa and 139.49 GPa respectively. The contact depth is 166 nm, indicating more than six layers were involved in this single indentation. More layers covered, more accurate. Fig. A.2 shows the multiple force displacement curves under the same maximum force 6000 μN for as-deposited Ti/Ni multilayers with various layer thickness: 10 nm, 25 nm, 100 nm, and 167 nm. The similar continuous loading parts were observed in all four curves. For 167 nm case, only two layers were involved by this indentation, with one complete Ni layer and one partial Ti layer. However, from the loading curve, there is still no obvious layered structure-induced loading discontinuity with displacement around 167 nm.

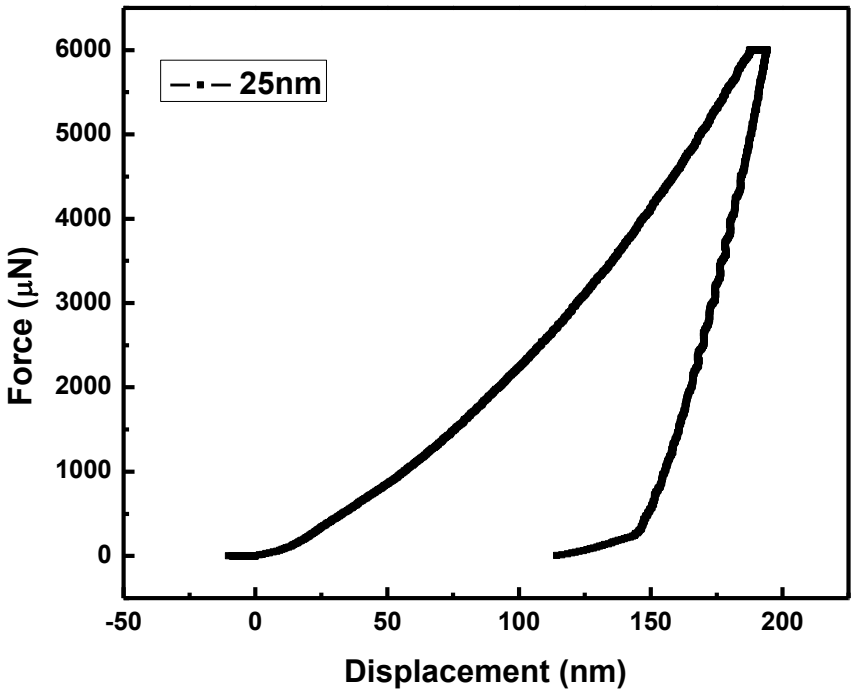

Figure A.1: Typical force displacement curve after single nanoindentation testing for as-deposited Ti/Ni multilayer thin film with layer thickness 25 nm under the maximum applied force 6000 μN. The hardness and reduced modulus are 5.93 GPa and 139.49 GPa respectively.

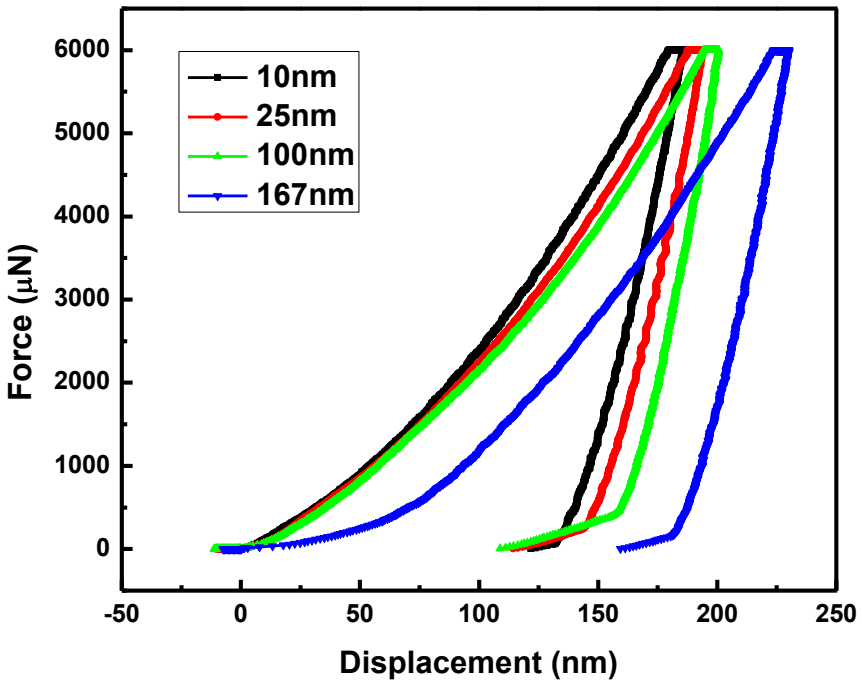

Figure A.2: Force displacement curves from nanoindentation for as-deposited Ti/Ni multilayer thin films with different layer thickness: 10 nm, 25 nm, 100 nm and 167nm. The maximum force is the same 6000 μN for all four cases.

Fig. A.3 shows the load displacement curves with different maximum loadings for 25 nm case. The load displacement curves could be used to distinguish the bad indents. In general, automation method is applied to carry out multiple indents with different maximum loadings. Bad indents might result from rough surface, debris or particle on indent position, or tip slipping during indentation. Fig. A.4 and Fig. A.5 show the 2D and 3D topographies from SPM after this automation indentation. These SPM images can be also used to distinguish the bad indents. From the SPM images, the spacing between indents is large enough to avoid the overlap of indentation-induced plastic zone.

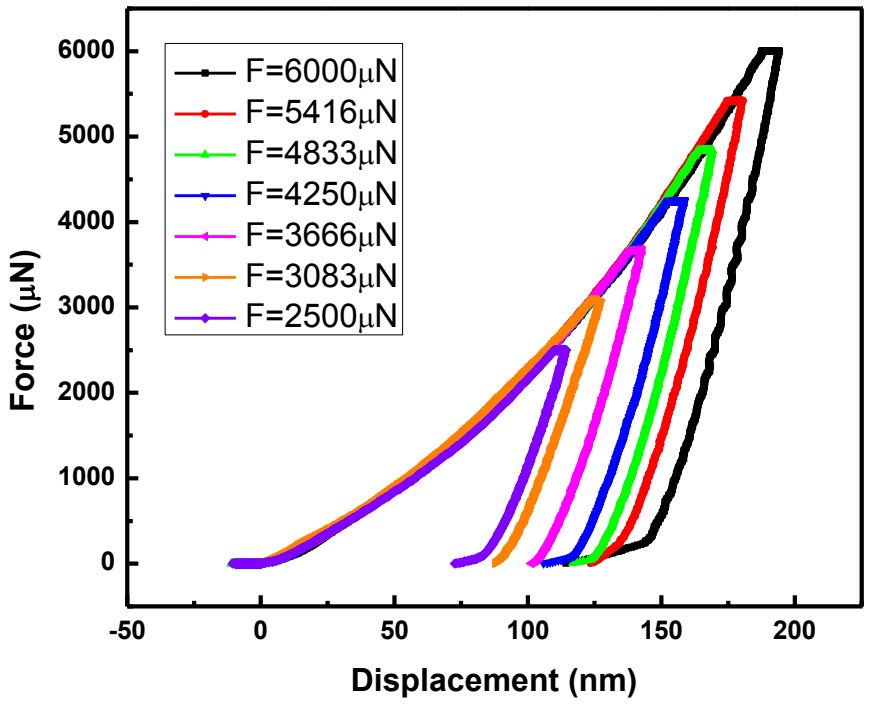

Figure A.3: Force displacement curves from automation nanoindentation with maximum force changing from 6000 μN to 2500 μN for as-deposited Ti/Ni multilayer thin films with layer thickness 25 nm. The loading paths are consistent in all cases.

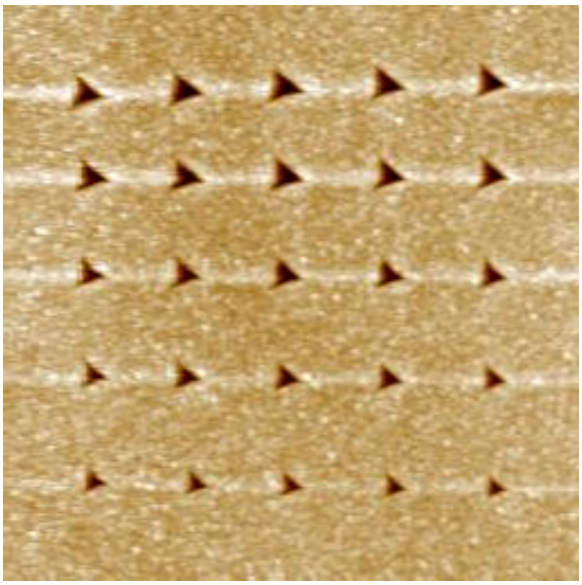

Figure A.4: 2D SPM image after one set of automation nanoindentation (5×5) for as-deposited Ti/Ni multilayer with layer thickness 25 nm. The scan size is $20\ \mu m \times 20\ \mu m$ in this case, and the spacing between indents is large enough to avoid overlapping.

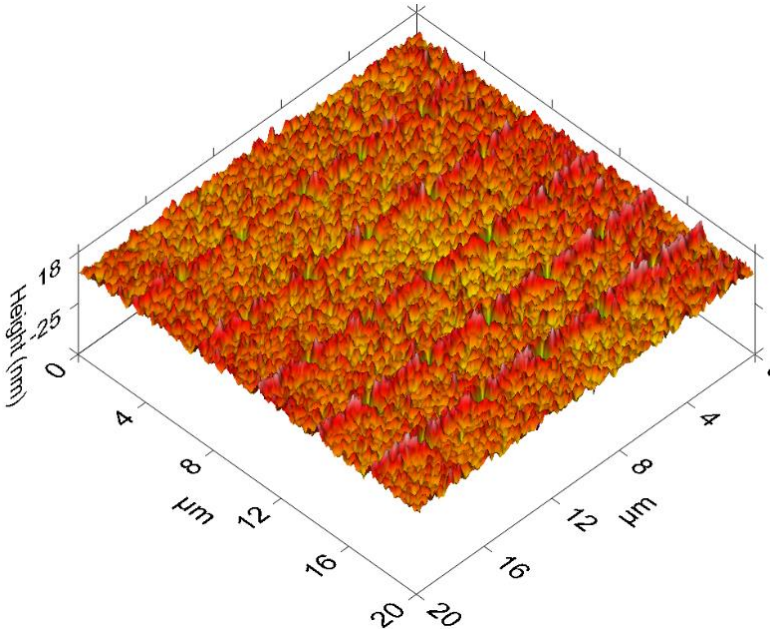

Figure A.5: 3D SPM image after one set of automation nanoindentation (5×5) for as-deposited Ti/Ni multilayer with layer thickness 25 nm.

By analyzing all accurate indent curves, the corresponding hardness and reduced modulus results could be obtained with respect to contact depth, as shown in Fig. A.6 and Fig. A.7. Then the average hardness/reduced modulus and standard derivation could be obtained as well. In addition, the substrate effect on the hardness and modulus can be obviously observed by using this procedure. In this case, shown in Fig. A.6 and Fig. A.7, no obvious substrate effect was observed here, probably because the contact depth is controlled within 20% of the total film thickness.

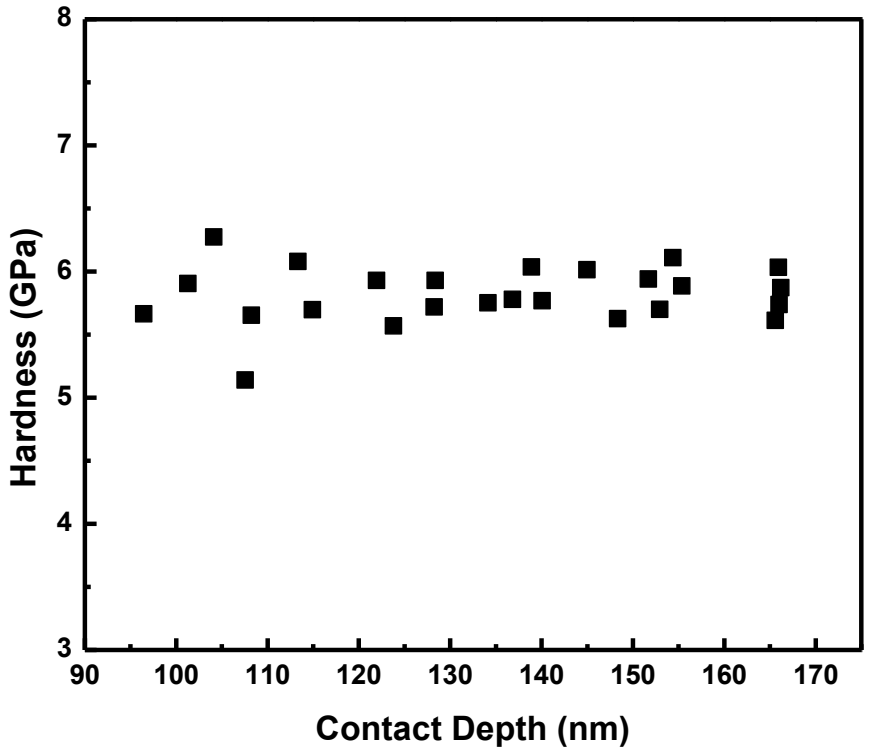

Figure A.6: Hardness results as a function of contact depth after automation nanoindentation for as-deposited Ti/Ni multilayer with layer thickness 25 nm. No obvious substrate effect on modulus is shown here.

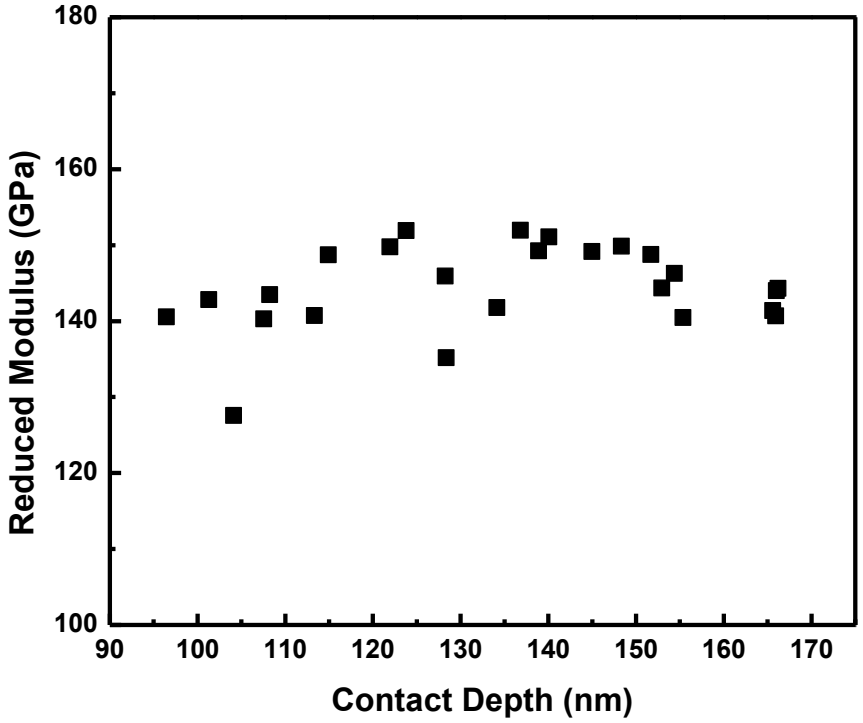

Figure A.7: Reduced modulus results as a function of contact depth after automation nanoindentation for as-deposited Ti/Ni multilayer with layer thickness 25 nm. No obvious substrate effect on modulus is shown here.

A.2 MODULUS RESULTS

In addition to hardness, modulus is another important mechanical property. The modulus information could be also obtained from nanoindentation testing as introduced in above section. For metallic multilayer thin film systems, the modulus is not as sensitive as hardness with respect to layer thickness or temperature. In current section, the modulus results are shown in different cases related with thermal and size effect for Ti/Ni multilayer thin films.

A.2.1 Substrate Temperature Effect

Fig. A.8 shows the reduced modulus as a function of substrate temperature for Ti/Ni multilayer thin films with layer thickness 20 nm. From the previous work discussed in Chapter 5, textured films were formed after deposition with low substrate temperature (up to 300 ℃), including preferred crystallographic texture (XRD spectra) and distinct columnar structure extending through layers (Cross-section SEM images). With high substrate temperature, columnar Ti-Ni alloyed structures were formed and Ti-Ni intermetallic phases were detected. Obvious microstructural evolution was observed with increasing substrate temperature, and a continuously increased hardness was obtained, however, no significant change in reduced modulus was shown as in Fig. A.8. Future work is necessary to understand this fundamental mechanism here.

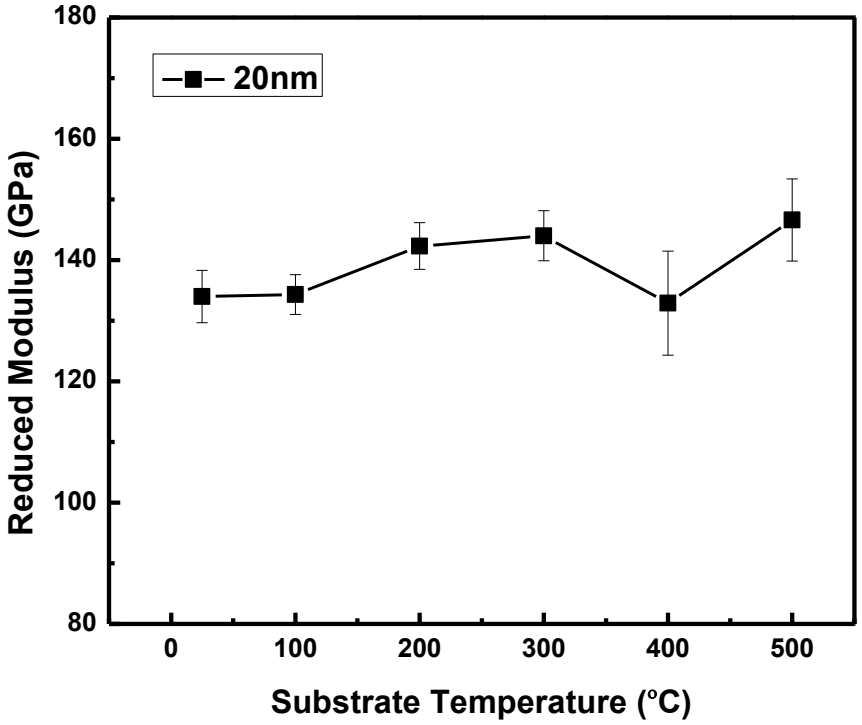

Figure A.8: Reduced modulus results as a function of substrate temperature for Ti/Ni multilayer thin films with layer thickness 20 nm, deposited with different substrate temperature from room temperature to 500 ℃.

In addition, a coupled substrate temperature-layer thickness effect on reduced modulus was shown in Fig. A.9 for Ti/Ni multilayer thin films with layer thickness ranged from 10 nm to 250 nm, deposited under room temperature and with substrate temperature 100 ℃ and 200 ℃. Layered structure is maintained after deposition with low substrate temperature. In this case, although obvious microstructure modification and different hardness behavior were observed, no significant change in reduced modulus was shown with different layer thickness and substrate temperature for multilayer thin films.

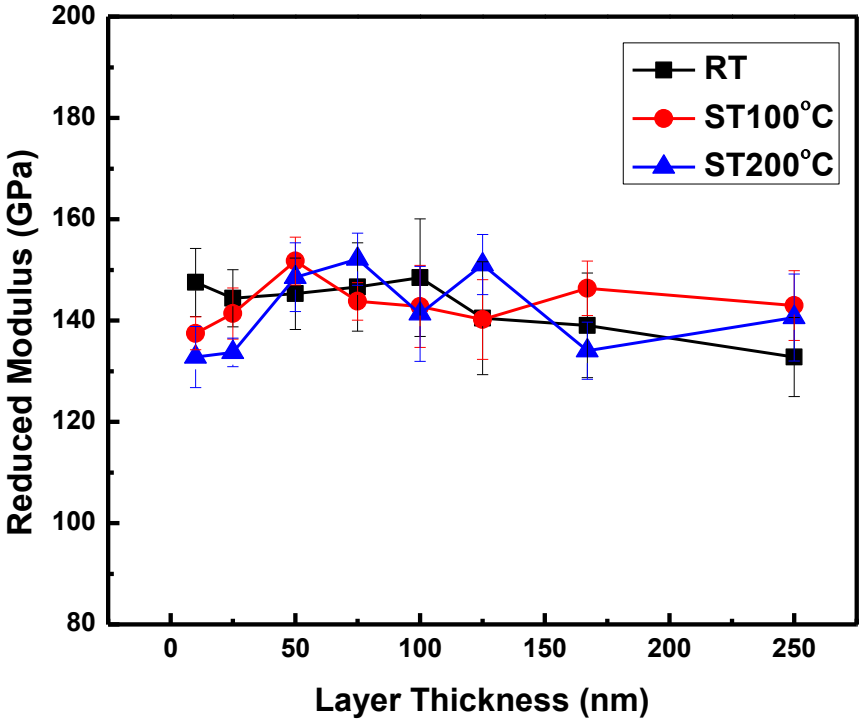

Figure A.9: Reduced modulus results as a function of layer thickness for Ti/Ni multilayer thin films with a wide range of layer thickness from 250 nm to 10 nm, and deposited under room temperature and with different substrate temperature 100 ℃ and 200 ℃.

A.2.2 Annealing Temperature Effect

Fig. A.10 and Fig. A.11 show the reduced modulus data for Ti/Ni multilayer thin films with layer thickness ranged from 200 nm to 6 nm, annealed at temperature up to 500 ℃. Obvious coupled layer thickness-annealing temperature effect on both microstructure and material hardness was discussed previously in Chapter 4. However, only minor change in reduced modulus was observed

here, without any general behavior trend. Note that the reduced modulus results of multilayers in RT case shown in Fig. A.10 are different from those shown in Fig. A.9. Berkovich indenter tip was used in annealing temperature project, while cube corner indenter tip in substrate temperature project. The indenter tip might result in some difference in the modulus. After annealing, a general increased modulus was observed in Fig. A.11, although slightly. In Fig. A.10, for samples with thin layer (16 nm ~ 6 nm) annealed at high temperature (500 ℃), much higher reduced modulus around 170 GPa was obtained, probably due to completely Ti-Ni alloyed structure.

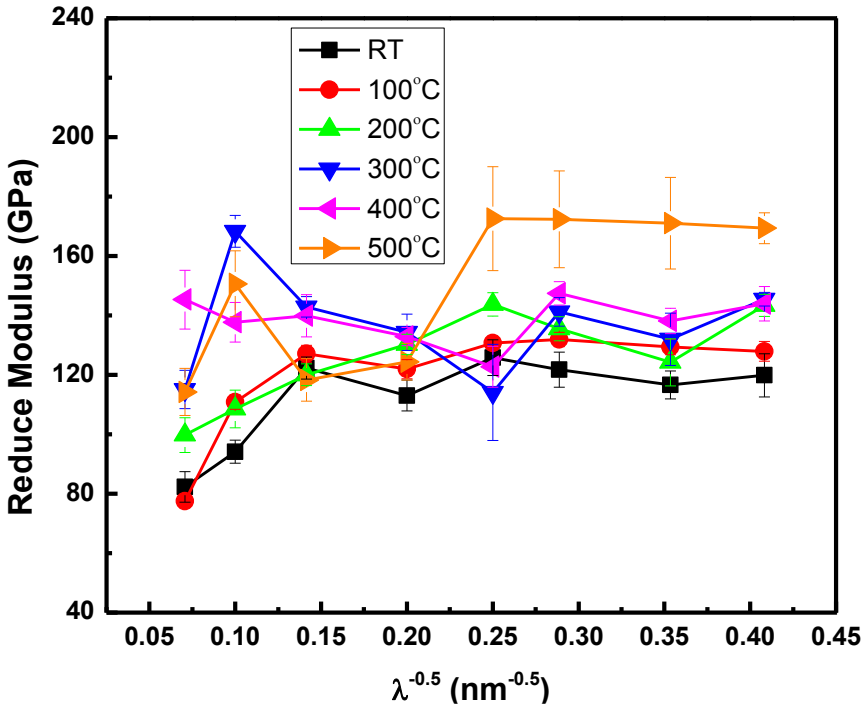

Figure A.10: Reduced modulus results as a function of layer thickness (inverse of root square of layer thickness) for Ti/Ni multilayer thin films with a wide range of layer thickness from 200 nm to 6 nm before and after annealing, with annealing temperature up to 500 ℃.

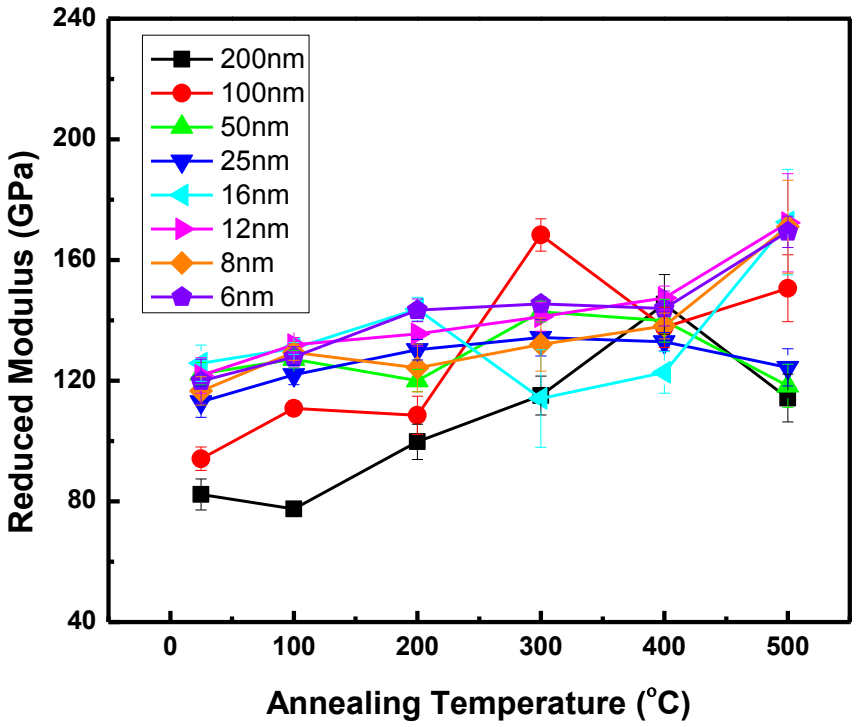

Figure A.11: Reduced Modulus results as a function of annealing temperature for Ti/Ni multilayer thin films with a wide range of layer thickness from 200 nm to 6 nm before and after annealing, with annealing temperature up to 500 ℃.

BIBLIOGRAPHY

1. Zhu, T. and J. Li, *Ultra-strength materials.* Progress in Materials Science, 2010. **55**(7): p. 710-757.
2. Zhu, T., et al., *Mechanics of ultra-strength materials.* MRS Bulletin, 2009. **34**(3): p. 167-172.
3. Brenner, S.S., *Growth and properties of "whiskers".* Science, 1958. **128**(3324): p. 569-575.
4. Brenner, S.S., *Tensile strength of whiskers.* Journal of Applied Physics, 1956. **27**(12): p. 1484-1491.
5. Ma, E., et al., *Strain hardening and large tensile elongation in ultrahigh-strength nano-twinned copper.* Applied Physics Letters, 2004. **85**(21): p. 4932-4934.
6. Lu, L., et al., *Ultrahigh Strength and High Electrical Conductivity in Copper.* Science, 2004. **304**(5669): p. 422-426.
7. Jiao, D., et al., *Intrinsic hierarchical structural imperfections in a natural ceramic of bivalve shell with distinctly graded properties.* Scientific Reports, 2015. **5**: p. 12418.
8. Liu, Y., et al., *Mechanical properties of highly textured Cu/Ni multilayers.* Acta Materialia, 2011. **59**(5): p. 1924-1933.
9. Misra, A. and H. Kung, *Deformation behavior of nanostructured metallic multilayers.* Advanced Engineering Materials, 2001. **3**(4): p. 217-222.
10. Wang, J. and A. Misra, *An overview of interface-dominated deformation mechanisms in metallic multilayers.* Current Opinion in Solid State and Materials Science, 2011. **15**(1): p. 20-28.

11. Uchic, M.D., et al., *Sample dimensions influence strength and crystal plasticity*. Science, 2004. **305**(5686): p. 986-989.

12. Rinaldi, A., et al., *Sample-size effects in the yield behavior of nanocrystalline nickel*. Acta Materialia, 2008. **56**(3): p. 511-517.

13. Greer, J.R. and W.D. Nix, *Nanoscale gold pillars strengthened through dislocation starvation*. Physical Review B, 2006. **73**(24): p. 245410.

14. Wu, B., A. Heidelberg, and J.J. Boland, *Mechanical properties of ultrahigh-strength gold nanowires*. Nature Materials, 2005. **4**(7): p. 525-529.

15. Murphy, K.F., et al., *Strain- and Defect-Mediated Thermal Conductivity in Silicon Nanowires*. Nano Letters, 2014. **14**(7): p. 3785-3792.

16. Márquez-Lucero, A., et al., *A method to evaluate the tensile strength and stress-strain relationship of carbon nanofibers, carbon nanotubes, and C-chains*. Small, 2005. **1**(6): p. 640-644.

17. Demczyk, B.G., et al., *Direct mechanical measurement of the tensile strength and elastic modulus of multiwalled carbon nanotubes*. Materials Science and Engineering: A, 2002. **334**(1–2): p. 173-178.

18. Deneen, J., et al., *In situ deformation of silicon nanospheres*. Journal of Materials Science, 2006. **41**(14): p. 4477-4483.

19. Lee, C., et al., *Measurement of the elastic properties and intrinsic strength of monolayer graphene*. Science, 2008. **321**(5887): p. 385-388.

20. Ohring, M., *Materials Science of Thin Films*. 2001: Academic Press.

21. Suresh, L.B.F.a.S., *Thin Film Materials: Stress, Defect Formation and Surface Evolution*. 2004: Cambridge University Press.

22. Seshan, K., *Handbook of thin film deposition*. 2012: William Andrew.

23. Auciello, O. and J. Engemann, *Multicomponent and Multilayered Thin Films for Advanced Microtechnologies: Techniques, Fundamentals and Devices: Techniques, Fundamentals, and Devices*. Vol. 234. 1993: Springer Science & Business Media.

24. Liu, Z., et al., *Thickness dependent magnetization dynamics of perpendicular anisotropy Co/Pd multilayer films*. Journal of Magnetism and Magnetic Materials, 2011. **323**(12): p. 1623-1626.

25. Lee, J.-C., et al., *Comparison of anistropic interface magnetoresistance in Co/Pt and Co/Pd multilayers*. Journal of Applied Physics, 2013. **113**(17): p. -.

26. Speetzen, N., et al., *Co/Pd multilayers for perpendicular magnetic recording media.* Journal of Magnetism and Magnetic Materials, 2005. **287**(0): p. 181-187.

27. Troussel, P., et al., *Multilayer optics for monochromatic high-resolution X-ray imaging diagnostic in a broad photon energy range from 2 keV to 22 keV*. Nuclear Instruments and Methods in Physics Research Section A: Accelerators, Spectrometers, Detectors and Associated Equipment, 2014. **767**(0): p. 1-4.

28. Artyukov, I.A., et al., *Soft X-ray imaging of thick carbon-based materials using the normal incidence multilayer optics*. Micron, 2010. **41**(7): p. 722-728.

29. Al-Marzoug, S.M. and R.J.W. Hodgson, *Optimization of platinum–carbon multilayer mirrors for hard X-ray optics*. Optics Communications, 2006. **268**(1): p. 84-89.

30. PalDey, S. and S.C. Deevi, *Single layer and multilayer wear resistant coatings of (Ti,Al)N: a review*. Materials Science and Engineering: A, 2003. **342**(1–2): p. 58-79.

31. Yang, Z. and J. Wang, *Orientation-Dependent Hardness in As-Deposited and Low-Temperature Annealed Ti/Ni Multilayer Thin Films.* Journal of Applied Mechanics, 2015. **82**(1): p. 011008-011008.

32. Yuan, F. and X. Wu, *Layer thickness dependent tensile deformation mechanisms in sub-10 nm multilayer nanowires.* Journal of Applied Physics, 2012. **111**(12): p. -.

33. Misra, A., J.P. Hirth, and R.G. Hoagland, *Length-scale-dependent deformation mechanisms in incoherent metallic multilayered composites.* Acta Materialia, 2005. **53**(18): p. 4817-4824.

34. Yang, Z. and J. Wang, *Coupled annealing temperature and layer thickness effect on strengthening mechanisms of Ti/Ni multilayer thin films.* Journal of the Mechanics and Physics of Solids, 2016. **88**: p. 72-82.

35. Yang, Z., M. Stossel, and J. Wang, *Microstructural evolution and surface strengthening of pulse-laser treated Ti/Ni multilayer thin films.* Extreme Mechanics Letters, 2015. **4**: p. 45-51.

36. Gupta, R., et al., *Thermal stability of nanometer range Ti/Ni multilayers.* Thin Solid Films, 2006. **515**(4): p. 2213-2219.

37. Bobeth, M., et al., *Thermal stability of nanoscale Co/Cu multilayers.* Zeitschrift fuer Metallkunde/Materials Research and Advanced Techniques, 2001. **92**(7): p. 810-819.

38. Bhatt, P., et al., *High temperature annealing effect on structural and magnetic properties of Ti/Ni multilayers.* Applied Surface Science, 2006. **253**(5): p. 2572-2580.

39. Clemens, B.M., W.L. Johnson, and R.B. Schwarz, *Amorphous zirconium-nickel films formed by solid state reactions.* Journal of Non-Crystalline Solids, 1984. **61–62, Part 2**(0): p. 817-822.

40. Clemens, B.M., *Effect of sputtering pressure on the structure and solid‐state reaction of titanium‐nickel compositionally modulated film.* Journal of Applied Physics, 1987. **61**(9): p. 4525-4529.

41. Clemens, B.M., *Solid-state reaction and structure in compositionally modulated zirconium-nickel and titanium-nickel films.* Physical Review B, 1986. **33**(11): p. 7615-7624.

42. Soyama, K., et al., *Developments of a small d-spacing multilayer neutron mirror and the supermirror neutron guide tube at the JRR-3M in JAERI.* Physica B: Condensed Matter, 2002. **311**(1–2): p. 130-137.

43. Grimmer, H., et al., *Polarizing mirrors for soft X-ray radiation.* Nuclear Instruments and Methods in Physics Research Section A: Accelerators, Spectrometers, Detectors and Associated Equipment, 2001. **467–468, Part 1**(0): p. 354-357.

44. Grimmer, H., et al., *X-ray reflectivity of multilayer mirrors for the water window.* Thin Solid Films, 1998. **319**(1–2): p. 73-77.

45. Hiroshi, N., *Nickel/Vanadium and Nickel/Titanium Multilayers for X-Ray Optics.* Japanese Journal of Applied Physics, 1990. **29**(6R): p. 1215.

46. Cho, H., H.Y. Kim, and S. Miyazaki, *Fabrication and characterization of Ti–Ni shape memory thin film using Ti/Ni multilayer technique.* Science and Technology of Advanced Materials, 2005. **6**(6): p. 678.

47. Lehnert, T., et al., *A new fabrication process for Ni–Ti shape memory thin films.* Materials Science and Engineering: A, 1999. **273–275**(0): p. 713-716.

48. Lehnert, T., et al., *Characterization of shape-memory alloy thin films made up from sputter-deposited Ni/Ti multilayers.* Acta Materialia, 2000. **48**(16): p. 4065-4071.

49. Cho, H., H.Y. Kim, and S. Miyazaki, *Alloying process of sputter-deposited Ti/Ni multilayer thin films*. Materials Science and Engineering: A, 2006. **438–440**(0): p. 699-702.

50. Petrović, S., et al., *Formation of intermetallic phase in Ni/Ti multilayer structure by ion implantation and thermal annealing*. Intermetallics, 2012. **25**(0): p. 27-33.

51. Fu, Y., et al., *TiNi-based thin films in MEMS applications: a review*. Sensors and Actuators A: Physical, 2004. **112**(2–3): p. 395-408.

52. Shabalovskaya, S.A. and J.W. Anderegg, *Surface spectroscopic characterization of TiNi nearly equiatomic shape memory alloys for implants*. Journal of Vacuum Science & Technology A: Vacuum, Surfaces, and Films, 1995. **13**(5): p. 2624-2632.

53. Duerig, T., A. Pelton, and D. Stöckel, *An overview of nitinol medical applications*. Materials Science and Engineering: A, 1999. **273–275**(0): p. 149-160.

54. Bouhki, M., A. Bruson, and P. Guilmin, *X-ray diffraction study of amorphization along interfaces in polycrystalline Ni/Ti multilayers*. Solid State Communications, 1992. **83**(1): p. 5-9.

55. Bhatt, P., A. Sharma, and S.M. Chaudhari, *Correlation of structural, chemical, and magnetic properties in annealed Ti ⁄ Ni multilayers*. Journal of Applied Physics, 2005. **97**(4): p. 043509.

56. Koehler, J.S., *Attempt to Design a Strong Solid*. Physical Review B, 1970. **2**(2): p. 547-551.

57. Chawla, M.A.M.K.K., *Mechanical Metallurgy: Principles and Applications*. 1984: Englewood Cliffs, N.J.: Prentice-Hall.

58. Oliver, W.C. and G.M. Pharr, *Measurement of hardness and elastic modulus by instrumented indentation: Advances in understanding and refinements to methodology*. Journal of Materials Research, 2004. **19**(01): p. 3-20.

59. Oliver, W.C. and G.M. Pharr, *An improved technique for determining hardness and elastic modulus using load and displacement sensing indentation experiments*. Journal of Materials Research, 1992. **7**(06): p. 1564-1583.

60. Huang, H. and F. Spaepen, *Tensile testing of free-standing Cu, Ag and Al thin films and Ag/Cu multilayers*. Acta Materialia, 2000. **48**(12): p. 3261-3269.

61. Friedman, L.H. and D.C. Chrzan, *Scaling theory of the Hall-Petch relation for multilayers*. Physical Review Letters, 1998. **81**(13): p. 2715-2718.

62. Anderson, P.M. and C. Li, *Hall-Petch relations for multilayered materials*. Nanostructured Materials, 1995. **5**(3): p. 349-362.

63. Anderson, P.M., T. Foecke, and P.M. Hazzledine, *Dislocation-based deformation mechanisms in metallic nanolaminates*. MRS Bulletin, 1999. **24**(2): p. 27-33.

64. Embury, J.D. and J.P. Hirth, *On dislocation storage and the mechanical response of fine scale microstructures*. Acta Metallurgica et Materialia, 1994. **42**(6): p. 2051-2056.

65. Phillips, M.A., B.M. Clemens, and W.D. Nix, *A model for dislocation behavior during deformation of Al/Al3Sc (fcc/L12) metallic multilayers*. Acta Materialia, 2003. **51**(11): p. 3157-3170.

66. Henager Jr, C.H., R.J. Kurtz, and R.G. Hoagland, *Interactions of dislocations with disconnections in fee metallic nanolayered materials*. Philosophical Magazine, 2004. **84**(22): p. 2277-2303.

67. Rao, S.I. and P.M. Hazzledine, *Atomistic simulations of dislocation-interface interactions in the Cu-Ni multilayer system*. Philosophical Magazine A: Physics of Condensed Matter, Structure, Defects and Mechanical Properties, 2000. **80**(9): p. 2011-2040.

68. Hoagland, R.G., et al., *On the strengthening effects of interfaces in multilayer fcc metallic composites*. Philosophical Magazine A: Physics of Condensed Matter, Structure, Defects and Mechanical Properties, 2002. **82**(4): p. 643-664.

69. Shoykhet, B., M.A. Grinfeld, and P.M. Hazzledine, *Internal stresses and strains in coherent multilayers*. Acta Materialia, 1998. **46**(11): p. 3761-3766.

70. Hull, R. and J.C. Bean, *Misfit dislocations in lattice-mismatched epitaxial films*. Critical Reviews in Solid State and Materials Sciences, 1992. **17**(6): p. 507-546.

71. Chu, X. and S.A. Barnett, *Model of superlattice yield stress and hardness enhancements*. Journal of Applied Physics, 1995. **77**(9): p. 4403-4411.

72. Misra, A., J.P. Hirth, and H. Kung, *Single-dislocation-based strengthening mechanisms in nanoscale metallic multilayers*. Philosophical Magazine A: Physics of Condensed Matter, Structure, Defects and Mechanical Properties, 2002. **82**(16): p. 2935-2951.

73. Masumura, R.A., P.M. Hazzledine, and C.S. Pande, *Yield stress of fine grained materials*. Acta Materialia, 1998. **46**(13): p. 4527-4534.

74. Kang, B.C., et al., *Bilayer thickness effects on nanoindentation behavior of Ag/Ni multilayers*. Scripta Materialia, 2007. **57**(8): p. 703-706.

75. Mara, N.A., et al., *Mechanism for shear banding in nanolayered composites*. Applied Physics Letters, 2010. **97**(2): p. -.

76. Bunge, H.-J. and W.T. Roberts, *Orientation distribution, elastic and plastic anisotropy in stabilized steel sheet*. Journal of Applied Crystallography, 1969. **2**(3): p. 116-128.

77. Bate, P., W.T. Roberts, and D.V. Wilson, *The plastic anisotropy of two-phase aluminium alloys—I. Anisotropy in unidirectional deformation.* Acta Metallurgica, 1981. **29**(11): p. 1797-1814.

78. Hazzledine, P.M. and B.K. Kad, *Yield and fracture of lamellar γα2 TiAl alloys.* Materials Science and Engineering: A, 1995. **192–193, Part 1**(0): p. 340-346.

79. Lu, L., et al., *Revealing the maximum strength in nanotwinned copper*. Science, 2009. **323**(5914): p. 607-610.

80. Li, X., et al., *Dislocation nucleation governed softening and maximum strength in nano-twinned metals*. Nature, 2010. **464**(7290): p. 877-880.

81. Shen, Y.F., et al., *Tensile properties of copper with nano-scale twins*. Scripta Materialia, 2005. **52**(10): p. 989-994.

82. You, Z.S., L. Lu, and K. Lu, *Tensile behavior of columnar grained Cu with preferentially oriented nanoscale twins.* Acta Materialia, 2011. **59**(18): p. 6927-6937.

83. You, Z., et al., *Plastic anisotropy and associated deformation mechanisms in nanotwinned metals.* Acta Materialia, 2013. **61**(1): p. 217-227.

84. Williamson, G.K. and W.H. Hall, *X-ray line broadening from filed aluminium and wolfram.* Acta Metallurgica, 1953. **1**(1): p. 22-31.

85. Zhai, Q., et al. *Characterization of high strength Cu/Ag multilayered composites*. in *Materials Research Society Symposium - Proceedings*. 1997.

86. Misra, A. and R.G. Hoagland, *Effects of elevated temperature annealing on the structure and hardness of copper/niobium nanolayered films.* Journal of Materials Research, 2005. **20**(8): p. 2046-2054.

87. Wen, S.P., et al., *Thermal stability of microstructure and mechanical properties of Ni/Ru multilayers*. Surface and Coatings Technology, 2008. **202**(10): p. 2040-2046.

88. Lee, H.-J., et al., *Thermal stability of a Cu/Ta multilayer: an intriguing interfacial reaction*. Acta Materialia, 1999. **47**(15–16): p. 3965-3975.

89. Troche, P., et al., *Thermally driven shape instabilities of Nb/Cu multilayer structures: instability of Nb/Cu multilayers*. Thin Solid Films, 1999. **353**(1): p. 33-39.

90. Edgar Alfonso, J.O.a.G.C., *Thin Film Growth Through Sputtering Technique and Its Applications*, in *Crystallization - Science and Technology*, D.M. Andreeta, Editor. 2012, InTech.

91. Zubeck, R.B., et al., *Growth morphologies of thick films of Nb3Sn formed by electron beam evaporation*. Thin Solid Films, 1977. **40**(0): p. 249-261.

92. Hong, R.J., et al., *Texture analysis of Al-doped ZnO thin films prepared by in-line reactive MF magnetron sputtering*. Applied Surface Science, 2004. **226**(4): p. 378-386.

93. Dong, L. and D.J. Srolovitz, *Texture development mechanisms in ion beam assisted deposition*. Journal of Applied Physics, 1998. **84**(9): p. 5261-5269.

94. Knuyt, G., et al., *A quantitative model for the evolution from random orientation to a unique texture in PVD thin film growth*. Thin Solid Films, 1995. **258**(1-2): p. 159-169.

95. Frey, H.K., Hamid, *Handbook of Thin-Film Technology*. 2015, Berlin, Heidelberg: Springer Berlin Heidelberg.

96. Feng, Y.C., D.E. Laughlin, and D.N. Lambeth, *Formation of crystallographic texture in rf sputter‐deposited Cr thin films*. Journal of Applied Physics, 1994. **76**(11): p. 7311-7316.

97. Cheng, F., C. Jiang, and J. Wu, *Effect of substrate temperatures on texture in thin films by magnetron sputtering.* Materials Letters, 2005. **59**(12): p. 1530-1532.

98. Gudmundsson, B., B.E. Jacobson, and H. Gruner, *The influence of substrate temperature on the microstructure and hardness of vacuum-plasma-sprayed Co Ni Cr Al Si Zr Y and Co Ni Cr Al Y alloys.* Materials Science and Engineering: A, 1989. **108**(0): p. 105-115.

99. Liu, Z.L. and L. Xiang, *Effects of working pressure and substrate temperature on the structure and mechanical properties of nanocrystalline SiC thin films deposited by bias-enhanced hot filament chemical vapor deposition.* Thin Solid Films, 2014. **562**(0): p. 24-31.

100. Li, Q., et al., *Low-temperature magnetron sputter-deposition, hardness, and electrical resistivity of amorphous and crystalline alumina thin films.* Journal of Vacuum Science & Technology A, 2000. **18**(5): p. 2333-2338.

101. Zhang, X., et al., *Low-temperature crystallization and hardness enhancement of alumina films using the resputtering technique.* Journal of Non-Crystalline Solids, 2013. **362**(0): p. 34-39.

102. Wu, Q., et al., *Characteristics of microstructure and mechanical properties of Sc films as a function of substrate temperature.* Applied Surface Science, 2012. **258**(19): p. 7421-7424.

103. Yang, Z., J. Lian, and J. Wang, *Molecular dynamics simulation of thin film interfacial strength dependency on lattice mismatch.* Thin Solid Films, 2013. **537**: p. 190-197.

104. Xiong, S., et al., *A two-stage heating scheme for heat assisted magnetic recording.* Journal of Applied Physics, 2014. **115**(17): p. 17B702.

105. Jergel, M., Anopchenko, A., Majková, E., Spasova, M., Luby, S., Holý, V., Brunel , M., Luches , A., Martino , M, *Excimer laser treated Ag/Co multilayers exhibiting giant magnetoresistance effect*. Superficies y vacío, 1999. **9**: p. 193-198.

106. Barna, P.B. and M. Adamik, *Fundamental structure forming phenomena of polycrystalline films and the structure zone models.* Thin Solid Films, 1998. **317**(1–2): p. 27-33.

107. Thornton, J.A., *HIGH RATE THICK FILM GROWTH.* Annual Review of Materials Science, 1977. **7**: p. 239-260.

108. Prokofiev, E.A., et al., *Suppression of Ni4Ti3 precipitation by grain size refinement in Ni-Rich NiTi shape memory alloys*. Advanced engineering materials, 2010. **12**(8).

109. Perriere, J., Millon, E., and Fogarassy, E., *Recent advances in laser processing of materials*. 2006, Amsterdam: Elsevier.

110. Ogawa, K., et al., *Elastic properties of nanoparticle chain aggregates of TiO2, Al2O3, and Fe2O3 generated by laser ablation.* Journal of Applied Physics, 2000. **87**(1): p. 63-73.

111. Ullmann, M., S.K. Friedlander, and A. Schmidt-Ott, *Nanoparticle formation by laser ablation.* Journal of Nanoparticle Research, 2002. **4**(6): p. 499-509.

112. Ohtsuka, S., et al., *Nonlinear optical property of CdTe microcrystallites doped glasses fabricated by laser evaporation method.* Applied Physics Letters, 1992. **61**(25): p. 2953-2954.

113. Sones, C.L., et al., *Laser-induced-forward-transfer: a rapid prototyping tool for fabrication of photonic devices.* Applied Physics A, 2010. **101**(2): p. 333-338.

114. Skolski, J.Z.P., et al., *Laser-induced periodic surface structures: Fingerprints of light localization.* Physical Review B, 2012. **85**(7): p. 075320.

115. Tsibidis, G.D., et al., *Dynamics of ripple formation on silicon surfaces by ultrashort laser pulses in subablation conditions.* Physical Review B, 2012. **86**(11): p. 115316.

116. Zhang, W., G. Cheng, and Q. Feng, *Unclassical ripple patterns in single-crystal silicon produced by femtosecond laser irradiation.* Applied Surface Science, 2012. **263**(0): p. 436-439.

117. Tan, B. and K. Venkatakrishnan, *A femtosecond laser-induced periodical surface structure on crystalline silicon.* Journal of Micromechanics and Microengineering, 2006. **16**(5): p. 1080.

118. Chen, X.Y., et al., *Pattern-induced ripple structures at silicon-oxide/silicon interface by excimer laser irradiation.* Applied Physics Letters, 2002. **81**(7): p. 1344-1346.

119. Brugger, J., et al., *Resistless patterning of sub-micron structures by evaporation through nanostencils.* Microelectronic Engineering, 2000. **53**(1–4): p. 403-405.

120. Young, J.F., J.E. Sipe, and H.M. Van Driel, *Laser-induced periodic surface structure. III. Fluence regimes, the role of feedback, and details of the induced topography in germanium.* Physical Review B, 1984. **30**(4): p. 2001-2015.

121. Young, J.F., et al., *Laser-induced periodic surface structure. II. Experiments on Ge, Si, Al, and brass.* Physical Review B, 1983. **27**(2): p. 1155-1172.

122. Sipe, J.E., et al., *Laser-induced periodic surface structure. I. Theory.* Physical Review B, 1983. **27**(2): p. 1141-1154.

123. van Driel, H.M., J.E. Sipe, and J.F. Young, *Laser-Induced Periodic Surface Structure on Solids: A Universal Phenomenon.* Physical Review Letters, 1982. **49**(26): p. 1955-1958.

124. Afonso, C.N., et al., *Laser induced interface reactions in Sb/Ge multilayer thin films: a study by RBS and CS-TEM*. 1992.

125. izmovi, M., et al., *Intermixing in Al/Ti multilayer structures induced by nanosecond laser pulses*. Physica Scripta, 2013. **2013**(T157): p. 014008.

126. Petrović, S., et al., *Laser-induced surface alloying in nanosized Ni/Ti multilayer structures*. Applied Surface Science, 2013. **264**: p. 273-279.

127. Dutta Majumdar, J. and I. Manna, *Laser surface alloying of copper with chromium II. Improvement in mechanical properties*. Materials Science and Engineering: A, 1999. **268**(1–2): p. 227-235.

128. Tong, X., M.-j. Dai, and Z.-h. Zhang, *Thermal fatigue resistance of H13 steel treated by selective laser surface melting and CrNi alloying*. Applied Surface Science, 2013. **271**(0): p. 373-380.

129. Fu, Y. and A.W. Batchelor, *Laser alloying of aluminum alloy AA 6061 with Ni and Cr. Part II. The effect of laser alloying on the fretting wear resistance*. Surface and Coatings Technology, 1998. **102**(1–2): p. 119-126.

130. Yang, Z., M. Stossel, and J. Wang, *Microstructural evolution and surface strengthening of pulse-laser treated Ti/Ni multilayer thin films*. Extreme Mechanics Letters.

131. Catalina, F., et al., *Kinetics of laser induced interface reactions in Sb/Ge thin multilayer films*. Surface Science, 1991. **251–252**(0): p. 1006-1011.

132. Satomi, N., et al., *Internal stress control of boron thin film*. Fusion Engineering and Design, 1998. **39–40**: p. 493-497.

133. Chang, R.C., et al., *Residual stresses of sputtering titanium thin films at various substrate temperatures*. J Nanosci Nanotechnol, 2010. **10**(7): p. 4562-7.

134. Alagoz, A.S., et al., *Residual Stress Reduction in Sputter Deposited Thin Films by Density Modulation*. MRS Online Proceedings Library Archive, 2009. **1224**: p. null-null.

135. Zhang, X., et al., *Effects of deposition parameters on residual stresses, hardness and electrical resistivity of nanoscale twinned 330 stainless steel thin films*. Journal of Applied Physics, 2005. **97**(9): p. 094302.

136. Misra, A., et al., *Residual stresses in polycrystalline Cu/Cr multilayered thin films*. Journal of Materials Research, 2000. **15**(03): p. 756-763.

137. Zhang, X. and A. Misra, *Residual stresses in sputter-deposited copper/330 stainless steel multilayers*. Journal of Applied Physics, 2004. **96**(12): p. 7173-7178.

VITA

Zhou Yang was born in Nanchang, Jiangxi province, P.R. China on September 15, 1988. In 2005, he began his undergraduate study in Theoretical and Applied Mechanics Department at the University of Science and Technology of China (USTC). During his junior year, he joined the Material Design and Behavior Lab and worked on mechanical analysis of single walled carbon nanotubes under supervision of Prof. Haibo Chen. He received his Bachelor of Science degree in Theoretical and Applied Mechanics in 2009. In the fall of 2009, Zhou entered the Master of Science program in the Department of Mechanical Engineering at the University of Washington. He joined the Laboratory for Nanomechanics and Complex Material Systems and began his research on molecular dynamics simulation of acoustic wave motion in thin solid films under the advisement of Professor Junlan Wang. In the fall of 2011, Zhou graduated with a Master of Science degree in Mechanical Engineering and then continued his research with Professor Wang at the University of Washington for his PhD studies. His PhD research was focused on the thermo-mechanical stability and strengthening mechanisms of Ti/Ni multilayer thin films. Zhou's work with Professor Wang has led to seven first-author articles that have been either published or submitted to top mechanics and materials journals. After receiving his PhD in Mechanical Engineering in the spring of 2016, he will be joining the Applied Materials, Inc. in Santa Clara, CA as a Process Engineer.